理學博士 學位論文

Plasmonic-enhanced Dye-Sensitized Solar Cells with Ag and Au Nanoparticles

은, 금 나노입자의 플라즈모닉 효과를 이용한 염료감응형 태양전지 효율 향상

2017 年 8 月

서울大學校 大學院
化學部
宋 多 賢

Abstract

Dye-sensitized solar cell (DSSC) is one of the efficient devices for generating electrons from solar light energy. Their advantages are low-cost processing, and various colors and transparent design for building integrated photovoltaics (BIPVs). Although DSSCs have numerous advantages, their power conversion efficiency (PCE) is lower than that of other solar cells. There are several ways to develop highly efficient DSSCs, such as improving light harvesting and electron transport.

Applying plasmonic metal nanoparticles (NPs), exhibiting localized surface plasmon resonances (LSPRs), to the DSSCs seems to be very effective for highly efficient DSSCs. Because their strong plasmonic near-fields increase the photon scattering cross-section enormously, thereby increasing the overall dye absorption and efficiency improvement by many different route such as light trapping. Therefore, when plasmonic metal NPs are applied to the DSSCs, light harvesting or carrier collection can be improved. Many attempts have been made to apply plasmonic metal NPs to increase the efficiency in DSSCs. Among the various plasmonic metal NPs, Ag and Au NPs are the most widely used metallic materials for triggering plasmonic enhancement in solar cells, because of their remarkable optical properties. The maximum absorption wavelengths of spherical Ag and Au NPs are approximately 400 nm and 530 nm, respectively. The absorption bands of these NPs are well matched to those of N719 dye which is the most commonly

used Ru-based dye molecules for DSSCs.

Therefore, in this thesis, Ag and Au NPs were incorporated together in DSSCs to enhancing two absorption bands of N719 dye at the same time for highly efficient DSSCs.

First, we fabricated Ag and Au NPs and used them to fabricate plasmonic DSSCs based on double-layered composite films. Compared to DSSCs without metal NPs, the PCE of the double-layered plasmonic DSSC enhanced from 8.42% to 10.03%, corresponding to 19% enhancement due to LSPR effect of Ag and Au NPs. The high efficiency of double-layered plasmonic DSSC might be due to a well optical spectra matching between the LSPRs of Ag and Au NPs and two strong absorption bands of N719 dye. For double-layered plasmonic DSSCs, the plasmonic metal NPs were dispersed into the TiO_2 photoactive layer and play a role as light harvesting and charge separation sites. By LSPR effect of Ag and Au NPs, the electric field around the metal NPs enhances and the light absorption cross section of the dye and the number of generated photoelectrons increase which in turn increases the efficiency of DSSCs.

Next, to fabricate highly efficient DSSCs, it is required to prevent the aggregation of metal NPs in the fabrication process of the composite film with TiO_2 and metal NPs. Therefore, we fabricated plasmonic layer consisting of Ag and Au NPs and incorporated on the TiO_2 photoactive layer of DSSCs. In this experiment, the plasmonic layer was fabricated by immobilizing plasmonic metal NPs on the surface of the TiO_2 film coated with

poly(4-vinylpyridine) (P4VP) to prevent the aggregation of metal NPs. The optimal conditions for metal NPs, such as immobilizing time and order, were examined. When both Au and Ag NPs were employed together at optimum conditions as the plasmonic layer, the PCE further improved from 8.39% to 10.17%, corresponding to 21.16% enhancement compared to DSSCs without metal NPs. The significant improvement of the PCE could be attributed to the LSPRs of plasmonic layer consisting of Au and Ag NPs. The plasmonic layer, which is located between the photoactive and scattering layers, functions as light scattering site and results in increase optical path length of the incident light, the light absorption and the electron transfer yields.

Lastly, multi-shaped Ag NPs were prepared and applied to DSSCs to enhance their PCE by broad absorption in visible region. Prepared multi-shaped Ag NPs were composed of various shapes such as spherical, rod, and triangle structures, which exhibited broader absorption than that of the spherical Ag NPs. The absorption of the plasmonic layer based on multi-shaped Ag and Au NPs could cover the absorption range of N719 dye. To study the plasmonic effect of the multi-shaped Ag NPs, we have compared the effect of spherical Ag NPs and multi-shaped Ag NPs on the photovoltaic properties of DSSCs based on a layer-by-layer structure and a composite film structure with Ag and Au NPs. The maximum absorption wavelength (λ_{max}) of the multi-shaped Ag NPs is 420 nm, including the shoulder with a full width at half maximum (FWHM) of 121 nm. This is a broad absorbance

wavelength compared to spherical Ag NPs, whose λ_{max} is 400 nm, without the shoulder of 61 nm FWHM. For DSSCs based on layer-by-layer structure with multi-shaped Ag and Au NPs, the PCE increased from 9.90% to 10.22%, a 3.2% enhancement, compared to DSSCs with spherical Ag and Au NPs. The PCE of the DSSCs based on layer-by-layer structure with multi-shaped Ag and Au NPs enhanced by 21.09%, compared to DSSCs without metal NPs. Similar to the layer-by-layer structure, the PCE of DSSCs based on the composite film structure with multi-shaped Ag and Au NPs increased from 9.99% to 10.34%, a 3.5% enhancement, compared to DSSCs with spherical Ag and Au NPs. The PCE of the DSSCs based on composite film structure with multi-shaped Ag and Au NPs enhanced by 20.51%, compared to DSSCs without metal NPs. It is concluded that the DSSCs with spherical Ag or multi-shaped Ag NPs was improved by the plasmonic effect, and the DSSCs with multi-shaped Ag NPs, which have broader absorption wavelengths range in the absorption of N719 dye at 393nm, exhibited better PCE than the DSSCs with spherical Ag NPs.

Key words: Dye-sensitized solar cells (DSSCs), Localized surface plasmon resonances (LSPRs), Plasmonic effect, Silver nanoparticles (Ag NPs), Gold nanoparticles (Au NPs).

Student Number: 2012-30074

Contents

List of Tables

List of Figures

Chapter 1

Introduction

1. 1. Solar cell

Due to lack of resources and pollution from fossil fuel, the development of renewable energy is needed urgently.[1, 2] The renewable energy includes wind power, wave power, tidal power, hydropower and solar energy power. Among them, the solar energy technologies play an important role in the green and renewable energy developments due to enormous source and the easier way to utilize. Solar energy has been used in many applications such as solar heating, solar thermal collector, solar photovoltaic cell etc. From among these, the solar photovoltaic cell can be used to generate electricity.[3, 4]

1. 1. 1. Classification of solar cells

The solar cell technologies can be divided in to three generations, which is silicon semiconductor, compound semiconductor and organic solar cell, as shown in Figure 1.1.[5, 6]

The crystalline silicon semiconductors are 1st generation solar cells. 1st generation solar cells include single and poly crystalline silicon solar cells. These are mainly commercialized in the market due to high stability and their good performance, about 15~20 %. However, they are fragile and relatively expensive to production.

2nd generation solar cells are based on amorphous silicon (a-Si) and compound semiconductors such as Copper Indium Callium Selenide (CIGS) and Cadmium Telluride/Cadmium Sulfide

(CdTe/CdS). The production costs of these solar cells are much cheaper than that of 1st generation solar cell. These solar cells are flexible to some degree. However, their performance is lower than the 1st generation solar cell, about 10~15%. The manufacturing processes, such as vacuum processes and high temperature treatments, are complicated and used materials are unusual elements, which is a limiting factor in the price.

3rd generation solar cells are organic solar cells. Their cost is very low and facile fabrication compared with other generation solar cells. The 3rd generation solar cells are promising but not yet commercial application. However, many groups are interested and research in this area. Their goal is to make solar cells cheap to produce and improve efficiency of solar cells.

In addition, the solar cell technologies can be classified into inorganic solar cells and organic solar cells by material used in device. Inorganic solar cells include the silicon semiconductor and compound semiconductor. On the other hands, dye sensitized solar cell (DSSC) and quantum dot solar cell (QDSC), which is comprised of organic materials such as polymer, dye molecules and quantum dots, are included in organic solar cells.[6, 7]

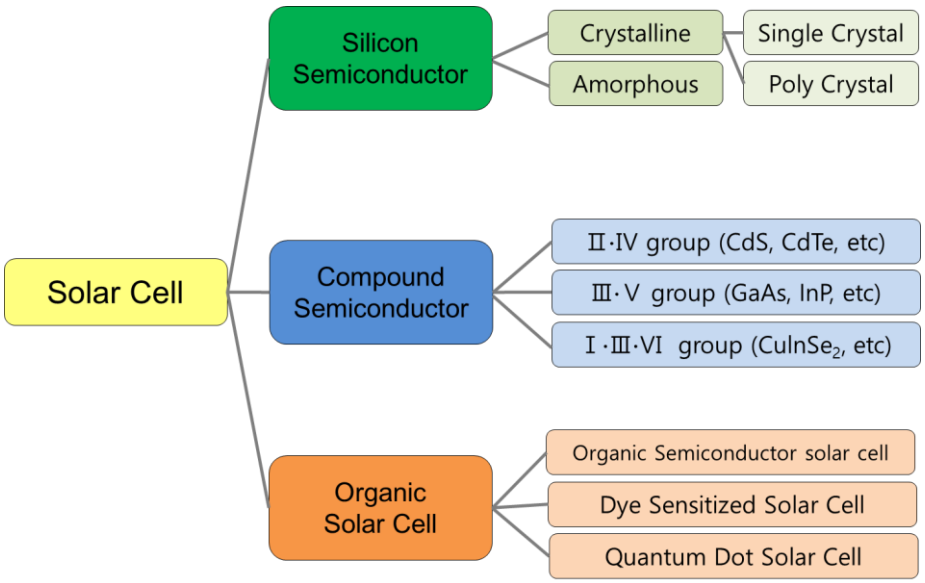

Figure 1. 1. Classification of solar cells; silicon semiconductor, compound semiconductor and organic solar cell.

1. 1. 2. Basic principle of solar cells

Above stated, photovoltaic solar cells convert sun light into usable energy such as electricity. The solar cell is composed of n-type and p-type semiconductor materials. A boundary between these two types of semiconductors is called p-n junction. Conversion of light into electricity is based on the photovoltaic (PV) effect[8, 9], which is generated in the p-n junction as shown in Figure 1.2. The principle of solar cells, the photovoltaic effect, can be demonstrated by three basic processes; Absorption, Separation and Migration. (1) When the sunlight shines the cell, an exciton, electron-hole pairs, is generated via absorption of incident photons. (2) Photo-generated charge carriers are separated in the p-n junction. The negatively-charged electrons move to n-type semiconductor, whereas the positively-charged holes move to p-type semiconductor. (3) The electricity is produced by flowing electrons through the external circuit between the two conductive electrodes.[10, 11]

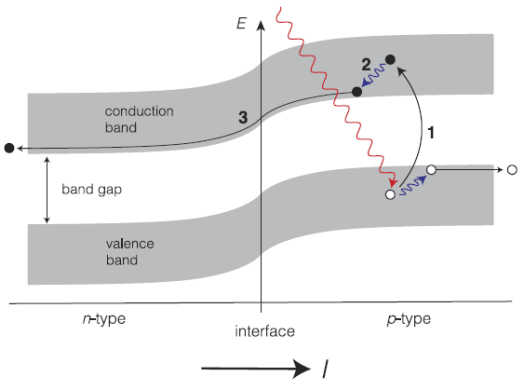

Figure 1. 2. A diagram showing the photovoltaic effect.[10]

1. 1. 3. Photovoltaic performance of solar cells

The photovoltaic performance of solar cells is usually measured under standard test conditions (STC); irradiance of 100mW/cm^2, air mass (AM) 1.5 and a cell temperature at 25 ℃. When forward bias is applied in solar cell, $J-V$ curve can be measured shown as Figure 1.3. The performance of solar cells can be determined by main 3 parameters; the short circuit current (J_{sc}), the open circuit voltage (V_{oc}) and the fill factor (ff).[12]

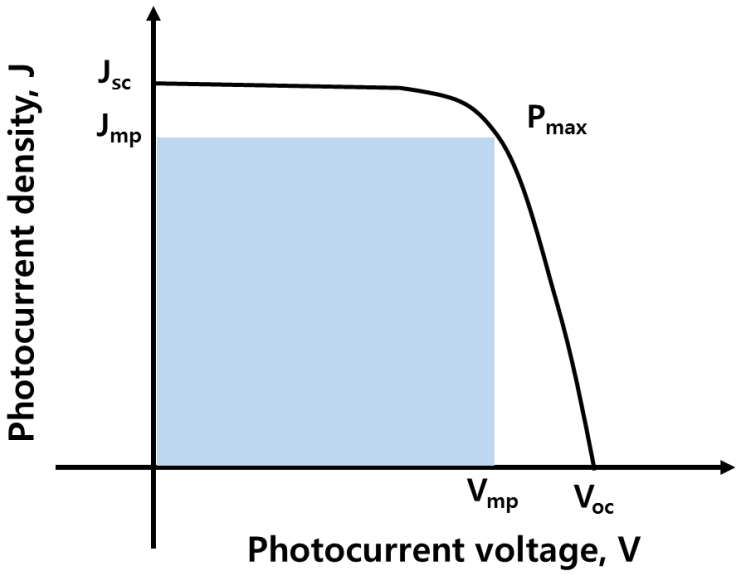

Figure 1. 3. Typical current−voltage ($J-V$) curve of illuminated solar cell.

The short circuit current, J_{sc}, is the current that flows through the external circuit when the voltage across device is zero. The J_{sc} is dependent of a number of factors such as the area, the optical property and the collection probability of solar cell, and the intensity and the spectrum of incident light.

The open circuit voltage, V_{oc}, is the voltage at zero current flows through the external circuit. The V_{oc} is determined by bandgap of semiconductor materials. The semiconductor materials, which have higher bandgap, get a higher V_{oc}, but lower J_{sc}.

The fill factor, *ff*, is the ratio between the maximum power P_{max} generated by a solar cell and theoretical power P_{theo} as shown Eq.1.[13]

$$P_{max} = J_{mp} \times V_{mp}$$

$$FF = \frac{P_{max}}{P_{theo}} = \frac{J_{mp} \times V_{mp}}{J_{sc} \times V_{oc}} \qquad \text{Eq.1}$$

The *ff* can be also represented by the area of the rectangle which will fit in an $J-V$ curve, shown as Figure 1.3. The *ff* depends on series resistance (R_s) and shunt resistance (R_{sh}). These parameters, R_s and R_{sh}, affect the shape of an $J-V$ curve.

The R_s is related in the diffusion of the electrolyte and the resistance at the interface between the semiconductor and the electrode. As the R_s increases, the J_{sc} and the *ff* decreases, whereas V_{oc} constants. The highest values of R_s will induce a great decrease

in J_{sc}, which results in resistor behavior, as shown in Figure 1.4(a). The shunt resistance (R_{sh}) is related with recombination of trapped electron. As the R_{sh} decreases, little recombination site generates and trigger current leakage. As the R_{sh} decreases, the V_{oc} and the *ff* decreases. The lowest values of R_{sh} will produce a significant reduction in V_{oc}, which is similar to operating characteristics of resistor, as shown in Figure 1.4(b). The higher R_s and the lower R_{sh} induce decrease in *ff* which results in a decrease of P_{max}.[11, 14]

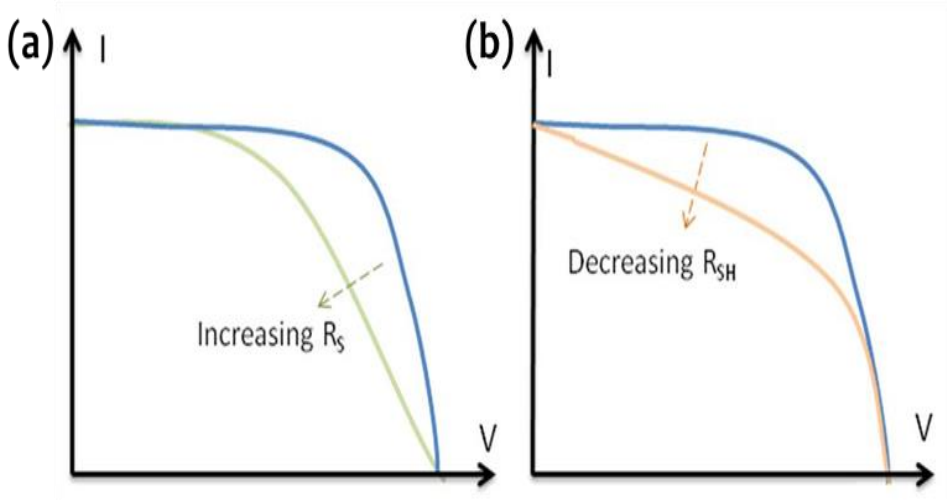

Figure. 1. 4. The effect (a) the series resistance, R_s, and (b) shunt resistance, R_{sh}, on the shape of the $I-V$ curve.

1. 1. 4. Efficiency of solar cells

To compare the performance of solar cell with another one, the power conversion efficiency (PCE), η, is the most commonly used parameter. The PCE describes the performance of the solar cell, which is the ratio of sun light energy that can be converted to electricity via solar cells. The PCE can be calculated by Eq.2. It is given by the ratio of power output (P_{out}) measured by J_{sc}, V_{oc} and ff of the cell versus the power input (P_{in}). Hence, the best performance of the solar cell is derived from the optimization of these three parameters.[15]

$$PCE = \frac{P_{out}}{P_{in}} = \frac{V_{mp} \times I_{mp}}{P_{in}} = \frac{V_{oc} \times J_{sc} \times FF}{P_{in}} \qquad \text{Eq.2}$$

The quantum efficiency (QE) of solar cells exhibits how efficiently the cells convert the incident sunlight into electricity. There are two types: external quantum efficiency (EQE) and internal quantum efficiency (IQE). The EQE is the efficiency of conversion whole incident photons into electric current under short circuit conditions. (Eq.3) The IQE is the efficiency of conversion absorbed photons into electric current under short circuit conditions. (Eq.4)[16, 17]

$$EQE = \frac{\text{electrons/sec}}{\text{photons/sec}} \qquad \text{Eq.3}$$

$$IQE = \frac{\text{electrons/sec}}{\text{absorbed photons/sec}} \qquad \text{Eq.4}$$

The QE is obtained by measuring the incident photon to current efficiency (IPCE). IPCE is percentage of incident photons in solar cell to excited charge carriers. It is measured as the photocurrent density in the external circuit under illumination divided by the photon flux of excitation wavelength. (Eq.5) [18]

$$IPCE\ (\%) = \frac{1240(eV \cdot nm) \times J(\mu A/cm^2)}{\lambda(nm) \times P(\mu W/cm^2)} \times 100 \qquad \text{Eq.5}$$

1. 2. Surface Plasmon Resonance(SPR)

The quasiparticle of the collective oscillation of the free electrons in a conduction material is called a plasmon. Especially in the case of metal NPs, plasmon can be designated surface palsmon resonances (SPRs) because it locally exists on the surface of metal nanoparticles. In general, the SPRs mean a kind of phenomena that visible or infrared frequency electromagnetic waves and plasmon combined along the interface between two media; a metal having negative dielectric constant and medium having positive dielectric constant. The combination generated plasmon-polariton and consequently led the optical absorption with locally increased electrical field.[19, 20] The generated plasmon-polariton is stronger than incident light and forms as evanescent wave that is exponentially declined as receding toward vertical direction from the interface. Through this phenomenon of SPRs, light energy is accumulated on the surface of the metal NPs and optical control is possible in the range less than optical diffraction limit.[21-24] Therefore, the SPRs have attracted significant attention in various fields like sensing, optoelectronics and biological applications due to their unique optical properties such as the light trapping and the capability of optical control. There are two different ways of SPRs phenomena, the one is propagating surface plasmon resonance (PSPR) and the other is localized surface plasmon resonance (LSPR).[25-29]

1. 2. 1. Propagating Surface Plasmon Resonance (PSPR)

The propagating surface plasmon resonance (PSPR) is observed on the interface between plate metal (100 nm – 1 μm) and dielectric substance. The PSPR is propagating electromagnetic wave along the metal–dielectric interface. The PSPR is generated by coupling between the electromagnetic waves and electron plasma oscillations of metal. The PSPR propagates in the *x*– and *y*–directions along the metal–dielectric interface, and decay faintly in perpendicular direction to the propagation, *z*–, as shown Figure 1.5.[30–33]

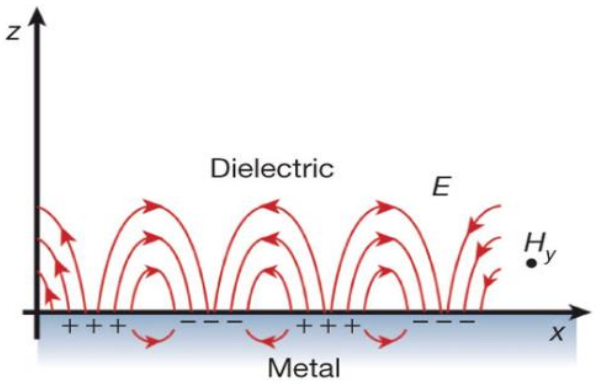

Figure. 1. 5. Schematic diagram of propagating surface plasmon resonance (PSPR).[33, 34]

1. 2. 2. Localized Surface Plasmon Resonance (LSPR)

The localized surface plasmon resonance (LSPR) is observed from the metal NPs having smaller size (5 – 20 nm) than the wave length of incident light. The LSPR occur when the oscillation frequency of free electrons in metal NPs well matches with the frequency of electric field of incident light as shown in Figure 1.6. In contrast to PSPR, the LSPR is non-propagating oscillation of the free electrons coupled to the electromagnetic field. The LSPR increases significantly the oscillation of free electrons and amplified local electromagnetic fields around metal NPs. This intense secondary electromagnetic field caused by metal NPs can more excite near located organic or inorganic semiconductor materials for additional electron-hole pairs generation. The LSPR is dependent of size[35, 36], shape[31] and dielectric local environment of the metal NPs.[37-40]

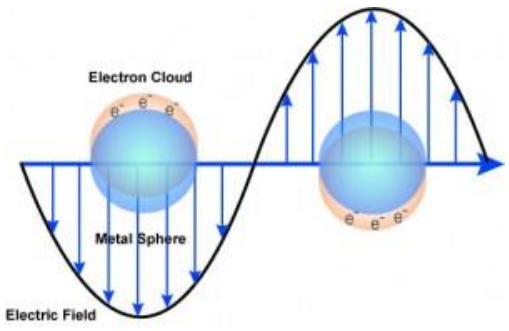

Figure. 1. 6. Schematic diagrams of localized surface plasmon resonance (LSPR).[34]

1. 2. 3. Plasmonic effect in solar cell

This SPR phenomenon capable of optical control can be used to trap light in solar cells. The SPR phenomenon is to be applicable to three kinds of methods in solar cells as shown in Figure 1. 7.

Firstly, metal NPs act as light scattering site, as shown in Figure 1.7(a). In this case, metal NPs increase optical path of the incident light and let more the incident light stay longer within the device, and consequently assists in more light absorption.[41-45]

Secondly, small metal NPs embedded in photoactive layer as shown in Figure 1.7(b). In this case, metal NPs can play the role of subwavelength antennas resulting from LSPR effect. It assists in generating more electric energy by enhancing electric field intensity at wavelength range that is possible of the LSPR. [46-49]

Lastly, if periodic corrugated metallic film is used, light is trapped by excitation states of surface plasmon-polartion at interface between the metal and the semiconductor material as shown Figure 1.7(c). It also assists in absorption of more light energy.[50-53]

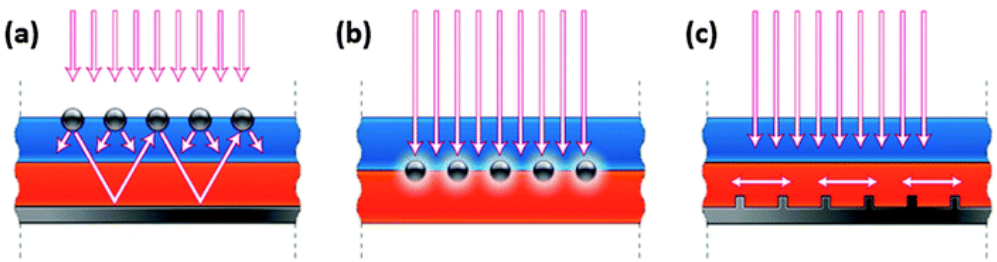

Figure. 1. 7. Schematic diagrams describing the principle of localized surface plasmon resonance (LSPR) applied to solar cell.[54]

1. 2. 4. Plasmonic metal nanoparticles

The brilliant color of noble metal NPs is attributed to collective oscillation of conduction band electrons, which is the LSPR. The LSPR in noble metal NPs significantly enhances light absorption such as strong light scattering to assist in absorbing more light from subwavelength antennas, and/or to generate plasmon-polaritons from incident light. The electromagnetic field near metal NPs can be also significantly enhanced.[55-57]

Scientific investigation of plasmonic metal NPs begun by Michael Faraday's research on Au colloidal solution.[58] Among the various noble metal NPs, Au and Ag NPs are the most generally used metal NPs for triggering plasmonic effect, because of their remarkable SPR optical properties.[59, 60] In case of nanosphere, Au NPs are generally used due to their air stability and LSPR wavelength in region more than 500nm. By contrast, Ag NPs have a high scattering efficiency and LSPR wavelength in region limited to 400- 500nm.[24, 61, 62]

The LSPR of plasmonic metal NPs can be modulated by adjusting their size and shapes.[31, 35, 36] Compared to spherical NPs, anisotropic NPs such as nanocubes, nanoplate, nanorods, and nanostars has larger surface area, higher absorption efficiency and extinction, and electromagnetic field localization at edges and corners.[63-65] Moreover, compared to the spherical Au or Ag NPs, which are commonly limited to a particular absorption region at approximately 400nm or 500nm, the anisotropic NPs exhibit a broad

absorption band including near infrared (NIR) region as shown in Figure 1.8.[66]

Due to their unique and tunable optical characteristics, plasmonic metal NPs are used in various applications such as sensing, optoelectronic, photovoltaics and biological applications. Many research group have performed to apply plasmonic metal NPs into the solar cells to increase the photocurrent and the efficiency of the solar cells.

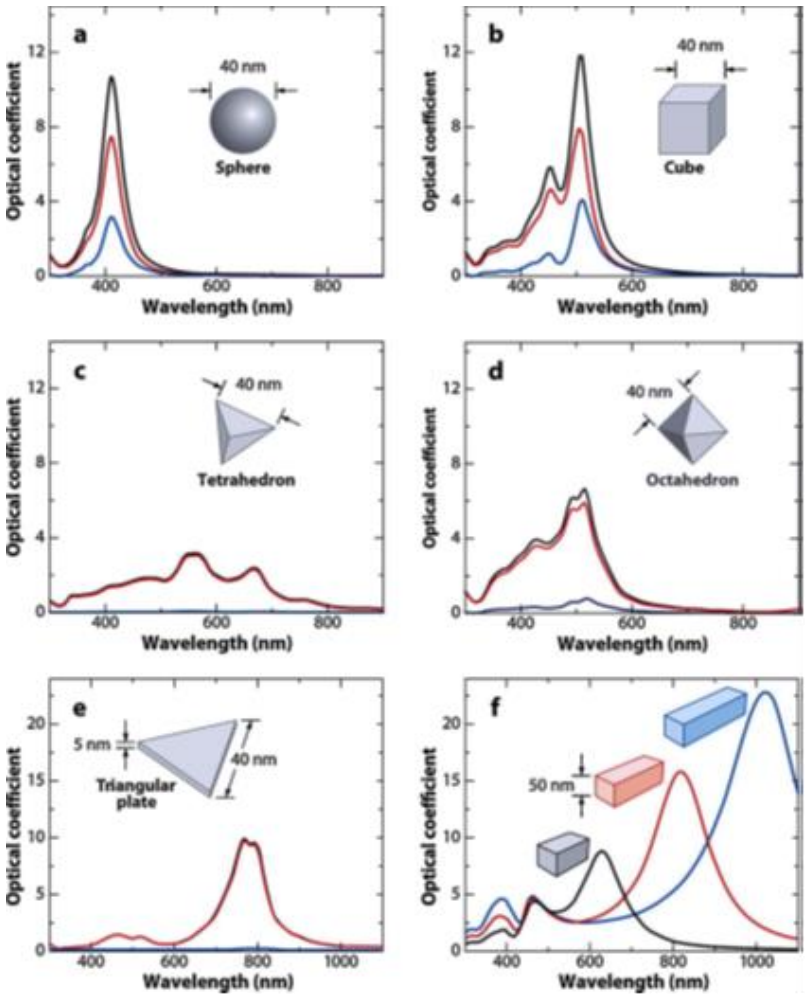

Figure. 1. 8. Extinction (black), absorption (red), and scattering (blue) spectra calculated for Ag nanoparticles of various shapes: (a) a sphere, (b) a cube, (c) a tetrahedron, (d) an octahedron, and (e) a triangular plate. (f) extinction spectra of rectangular bars with different aspect ratios.[66]

1. 2. 5. Synthesis methods for metal nanoparticles

There are diverse methods to fabricate metal NPs. It can be generally classified by two approaches: *Top-down* and *Bottom-up*.[67, 68]

The top-down methods are determined that the nanoparticles are fabricated by cutting the initial bulk materials into the micron or nanoscale particles through chemical, physical or mechanical processes as shown in Figure 1. 9. The top-down methods involve ball milling, lithography and etching etc. These methods are mainly used in industrial nanomaterial preparation and semiconductor manufacturing.[69]

The photolithography, which is the most used method in top-down methods, is used to manufacture computer chips and semiconductors.[70, 71] The designed pattern on the Si wafer can be obtained by etching through photochemical reaction between photoresist and UV light. In the mechanical milling method, strong mechanical shear forces are applied in the bulk material by milling technique to make nanoscale particles.[72] In the laser ablation method, the small portion of metal target are vaporized and converted to metal NPs by applying high energy laser beam.[73] In arc discharge method, the bulk materials are broken down by arc.[74] The top-down methods have disadvantages such as expensive and comprehensive technologies, physical limits and heat dissipation.

In contrast, the bottom-up methods are determined that the atoms or the molecules are self-assembled in solution or gas phase

to form nanostructures as shown in Figure 1. 9.[75] Fabrication with bottom-up methods is much less expensive than top-down methods. Bottom-up methods involve atomic layer deposition, sol-gel process, self-assembly process, chemical vapor deposition, and seed-mediated growth method etc.

By atomic layer deposition (ALD), it can be deposited thin film with desired thickness controlled on the atomic level. It is used for surface engineering of complex nanomaterials and semiconductor fabrication.[76] Sol-gel process has been widely used for the generation of the metal oxide nanoparticles, ceramic and glass materials from liquid solutions or colloidal nanoparticles.[77] Molecular self-assembly (MSA) means that molecules are self-assembled without the outside interactions. Self-assembled monolayers (SAMs), which are the most famous MSA technique, are fabricated by using molecules such as thiols and silanes. The basic building blocks are fabricated through chemical method, and combined by Van der Waals force to form various nanostructures.[78, 79] MSA method has been applied in various biomedical applications. In chemical vapor deposition (CVD) is a chemical reaction between the heated substrate surface and the vapor or gas phase precursor.[80] The CVD has been widely used to fabricate different types of carbon nanostructures such as carbon nanotubes. The seed-mediated growth method is generally used for formation of nanoparticles and modulation of their shape and size.

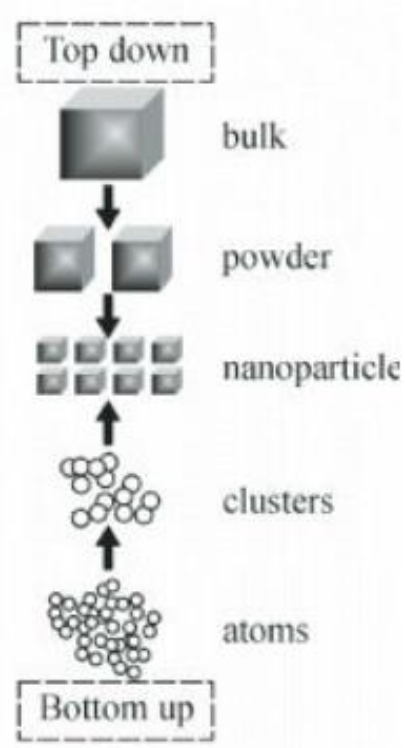

Figure. 1. 9. Illustration of Top-down and Bottom-up methods.[75]

1. 2. 6. Seed-mediated growth method

The seed-mediated growth process is a useful method to fabricate metal NPs with various shapes such as rod, wire, triangle, star, cube and so on. Many factors, which are stabilizer, nucleation time, reducing agent and so on, influence the size and shape of metal NPs.[81] It is a modified method of Zsigmondy's nuclear method.[82] This method includes two steps; (1) synthesis of seed (nucleation) and (2) growth of seed.

The first step is the preparation of seeds by chemical reduction. The metal ions are reduced to metal atoms by reducing agents in solution with stabilizer. In synthesis of seeds, the reducing agent is important factor. Generally, smaller metal NPs are fabricated by rapid reduction whereas larger metal NPs are fabricated by slow reduction. Among many reducing agents, sodium borohydride ($NaBH_4$) is mostly used as reducing agent. When $NaBH_4$ is used as reducing agent, it reduces metal ions rapidly and form seeds with increasing monodispersity due to strong reducing agent. While when citrate is used as reducing agent, the reduction rate lower which results in low monodispersity of seeds due to weak reducing agent. For monodispersity of the seeds, the nucleation time should be short.

Seeds are stabilized by a stabilizer such as ligand, polymer, surfactant, dendrimer in solution. The stabilizers, which bind to the surface of seeds, retard further growth and agglomeration of seeds. The shape and growth of nanoparticles are controlled by binding affinity and selectivity of stabilizer. In synthesis of seed, the

stabilizer has medium or low binding affinity to exchange in growth process.

The second step is the growth of seeds into nanoparticles with the desired various morphology. The growth solution involves a metal precursor, stabilizers and weak reducing agent. In growth of seeds, the added metal precursors are reduced on the surface of the seeds, and seed stabilizers exchange to growth stabilizers which have a higher bonding affinity. The stabilizers, which have various affinities for binding across a particle, fabricated metal nanoparticles with desired morphology such as cubes, rods and so on. The size of metal NPs is modulated by the amount of added seeds. A low concentration of seeds in the growth solution fabricated larger metal NPs.

For instance, Murphy et al. prepared Au nanorods with aspect ratios by a seed-mediated growth method.[83] In synthesis of seeds, $HAuCl_4$ is reduced to citrate-capped Au NPs by borohydride. And then, by adjusting the ratio of seeds, the aspect ratio of the Au nanorods is controlled in growth process.

1. 3. Dye-Sensitized Solar Cells

Dye-sensitized solar cells (DSSCs) are one of alternative to silicon based solar cells. O'Regan and Grätzel firstly fabricated DSSC used by ruthenium based dye and mesoporous TiO_2 nanoparticle film of 10 μm thickness.[84] In this case, PCE of 7% and then it was high enough to lead further studies for the cells having similar structure. The DSSCs have some advantages; these are high performance in comparison with relatively low cost, low handling expenses, low strength of optical and incidence angle, mechanical durability and light weight. Moreover, various color and transparency can be displayed, and it can be efficiently operated at the wide range of wavelength. Even though DSSCs have a lot of advantages, these have disadvantages like lower PCE of the DSSCs than that of the other solar cells.[85-88] To overcome disadvantages, many fields of studies related to DSSC are being progressed.[89-92]

1. 3. 1. Components and Structure of DSSCs

DSSCs are composed with a transparent conducting substrate, a working electrode based on porous nanocrystalline TiO_2, a sensitizer (dye), an electrolyte and a counter electrode as shown Figure 1. 10.

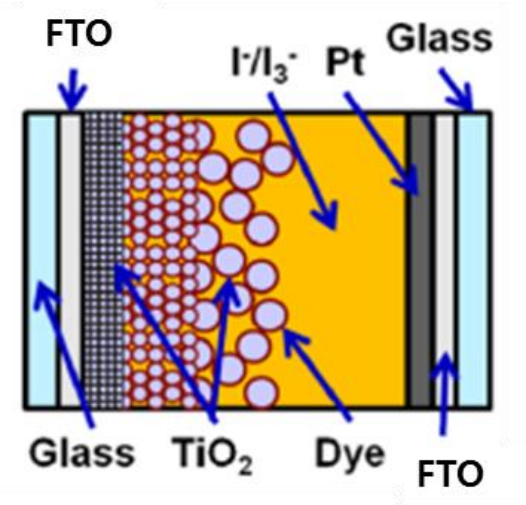

Figure 1. 10. Diagram of a conventional dye-sensitized solar cell.

As a transparent conducting substrate in solar cell, both a fluorine doped tin oxide (FTO) and an indium tin oxide (ITO) glass have been used. The transparent conducting oxide (TCO) as a photoanode in DSSCs is required high optical transparency, high conductivity and low sheet resistance which improve carrier mobility and reduce carrier loss. In fabrication of mesoporous TiO_2 working electrode, TiO_2 NPs paste coated on the transparent conducting substrate is sintered at high temperature, 450-500 ℃, to enhance the electronic contact. Above 300 ℃, the sheet resistance of ITO glass significantly increases which results in a decrease of efficiency. Hence, the transparent conducting substrate of DSSCs prefers FTO to ITO glass due to thermally stability.[93]

Many oxide semiconductors have been used as electron acceptors for DSSCs. The semiconductor is significantly required to high mobility of the charge carrier to reduce the resistance. Despite

the existence of oxide semiconductor with wide band gap such as tin dioxide (SnO_2) and zinc oxide (ZnO), the titanium dioxide (TiO_2) thin films are the most promising materials as photoelectrode to be used in DSSCs due to non-toxic, ultra-violet light absorption, and a large surface area. In the TiO_2 based DSSCs, the light harvesting efficiency of TiO_2 is influenced by its crystalline forms. TiO_2 nanoparticles have three mainly different crystalline structures, such as rutile, anatase, and brookite structures. Three different TiO2 crystalline structures have different physical and chemical properties. Among their structures, only rutile and anatase TiO_2 play any role on DSSCs. In comparison to the photoelectron chemical properties of the DSSCs, the PCE and the J_{sc} of the DSSC with rutile-TiO_2 film is lower than those of the DSSCs with anatase-TiO_2 film. The difference in the J_{sc} between them is attributed to lower the surface area of the rutile-TiO_2 film than that of the anatase-TiO_2 film. Consequently, the amount of adsorbed dye in rutile-TiO_2 film is lower than in anatase-TiO_2 film. In addition, electron transport is slower in the rutile-TiO_2 film than in the anatase-TiO_2 film due to differences in the low extent of coordination number related with the packing density of particle. Therefore, the anantase-TiO_2 is appropriate materials as semiconductor for the DSSCs due to large surface area and great electron mobility.[94]

One drawback with DSSCs based on TiO_2 film is that TiO_2 has good absorption in UV region but not visible region, which is mainly utilized solar spectrum region, due to the wide band gap (anatase

3.2eV and rutile 3.4eV). To solve this problem, dye molecules are adsorbed on the TiO_2 nanoparticle surface as a photosensitizer.

Dye, the main characteristic of DSSCs, is the most important component of DSSC because it determines the performances of overall device.[95-97] Dye molecules absorb energy of the sunlight and inject electrons into the conduction band of the oxide semiconductor layer. As a photosensitizer, dye is required to excellent absorption in all incident light such as panchromatic absorption , suitable the HOMO and LUMO of the sensitizer, good solubility in organic solvent and the existence of surface anchoring group such as carboxylate or phosphonate group. Ruthenium (Ru) polypyridyl complexes, such as N3, N719 and N749, are mostly used as dye in DSSCs.[98-101] Figure 1.11 shows the molecular structures of N3, N719 and N749 dyes.[102] The N3 dye has two bipyridine and two thiocyanato (NCS) ligands attached loosely. And the N3 dye has red color. The N3 dye can provide high J_{sc}, whereas V_{oc} is not. The N719 dye molecular structure is similar to N3 dye molecular structure; hydrogen ions (H^+) of two carboxyl groups are substituted with tetrabutylammonium ion (TBA^+). The N719 dye has maximum absorption wavelength at 393nm and 533nm. Compared to N3 dye, the N719 dye can increase V_{oc}. It is resulted from the replacement of the cations which is related with proton concentration at the surfaces. The N749 dye, which is called black dye, has terpyridine ligands. The N749 dye has green color and the panchromatic absorption up to 920nm. The N749 dye has a disadvantage which requires thicker TiO_2 film to more adsorb dye

due to lower absorption coefficient than N3 and N719 dye. The thicker TiO_2 film results in decrease of J_{sc} and V_{oc}.

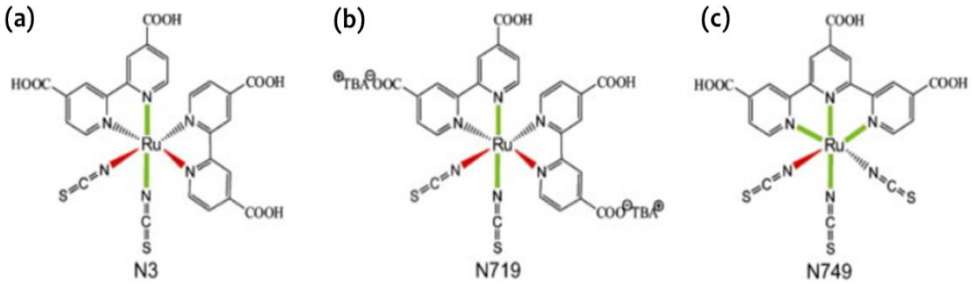

Figure 1. 11. The molecular structures of Ruthenium (Ru) polypyridyl complexes dye (a)N3, (b) N719, (c) N749.[102]

The electrolyte is responsible for the charge transport between the positive and negative electrodes, and regeneration of the oxidized dye and itself during DSSC operation.[103] The electrolyte is a key factor for determining the PCE and stability of DSSC. The liquid electrolytes are utilized as redox mediator for DSSCs due to facile preparation, good solubility, suitable redox potential and high conductivity. The iodide/triiodide (I^-/I_3^-) electrolyte in the liquid electrolyte system is commonly used and the best liquid electrolyte in DSSCs. The electrons in TiO_2 and I_3^- are slowly recombined whereas the oxidized dye is quickly regenerated by the I^-/I_3^- electrolyte. By incorporation of 4-tertbutyl pyridine and guanidine in the I^-/I_3^- electrolyte, the V_{oc} and the *ff* of DSSC increase due to decrease of recombination rate.[104] By incorporation of LiI in the liquid electrolyte, the J_{sc} of DSSC enhance due to increase the

mobility of electrons in TiO_2 nanoparticle network, but V_{oc} of DSSC decrease due to easy combination of ambipolar Li^+ and I_3^-.[105] The utilization of the liquid electrolyte in DSSC has problems such as volatilization of solvent and leakage which results in instability of DSSCs. Hence, the solid-state or quasi-solid state electrolytes have been used in DSSCs instead of the liquid electrolyte.[106]

The counter electrode in DSSCs plays role as a catalyst to reduce the redox species and regenerate dye. And electrons flowing through external load are collected at the counter electrode. Platinum (Pt) is generally used as a material for counter electrode in DSSCs due to its excellent chemical and physical properties such as stability in air or water, electro catalytic activity and good electrical and thermal conductivity. Due to high expenses, it is required to find cheaper materials which are available to replace Pt. There are many promising alternatives to Pt, such as carbon materials and conducting polymers etc.[107-109]

1. 2. 2. Working principle of DSSCs

All of the photovoltaic devices convert sunlight into electrical power by the photovoltaic effect. The working principle of DSSCs is different from the conventional photovoltaic devices with a p−n junction. In conventional solar cell with p−n junction, the processes of light absorption, charge carrier separation and transportation are achieved in the semiconductor material. In contrast to p−n junction solar cell, these processes are separated in DSSC. Dye absorbs the incident light and charge carriers separate at the surfaces between the dye, semiconductor and electrolyte. The excited electrons from dye transport to semiconductor material. The charge transport only occurs in semiconductor material. The working mechanism of the DSSCs is simple as shown in Figure 1.12.[110]

When incoming photon is absorbed by dye, the dye molecules excite an electron from HOMO to LUMO level of dye as represented by Eq.1. Then, the excited electron is injected to conduction band of the semiconductor material, such as TiO_2, and generate the oxidized of dye in the process as represented by Eq.2.

The electrons are transported to the transparent conducting oxide (TCO) substrate through the TiO_2 nanoparticle network. Finally, electrons reach the counter electrode pass through the external circuit as represented by Eq.3. At the counter electrode, the oxidized dye is reduced by electron donation of I^- in the electrolyte. This process is exhibited by Eq.4. I_3^- is donated electron from the external loads and regenerates to I^- as represented by Eq.5.

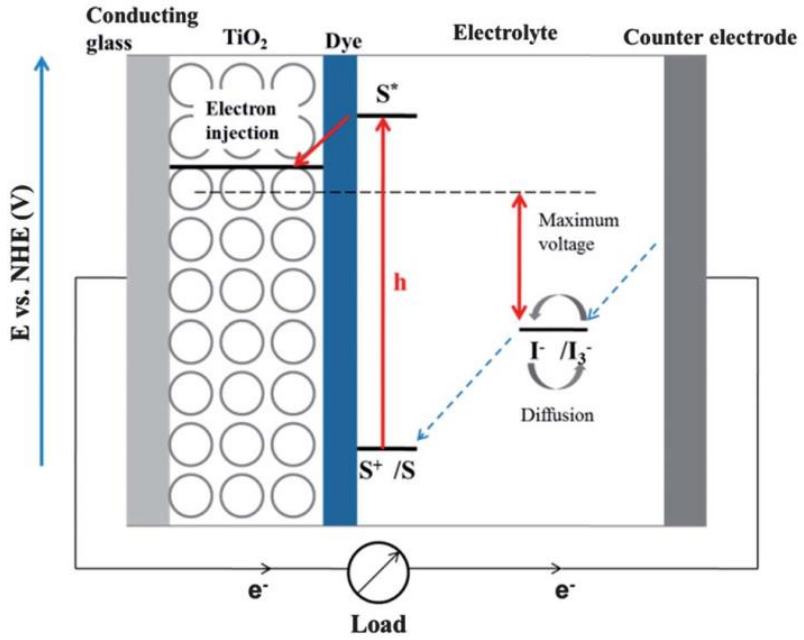

$$S + photon \rightarrow S^{*} \qquad \text{Eq.1}$$

$$S^{*} + TiO_2 \rightarrow e^{-}_{(TiO_2)} + S^{+} \qquad \text{Eq.2}$$

$$e^{-}_{(TiO_2)} + C.E. \rightarrow TiO_2 + e^{-}_{(C.E.)} + electrical\ energy \qquad \text{Eq.3}$$

$$S^{+} + \frac{3}{2}I^{-} \rightarrow S + \frac{1}{2}I_3^{-} \qquad \text{Eq.4}$$

$$\frac{1}{2}I_3^{-} + e^{-}_{(C.E.)} \rightarrow \frac{3}{2}I^{-} + C.E. \qquad \text{Eq.5}$$

Figure 1. 12. Scheme and equation of working mechanism of DSSC.[110]

1. 3. 3. Plasmonic enhanced DSSCs

In recent reports, it is shown that the surface plasmon resonance in noble metal NPs enhance light absorption due to strong light scattering. By applying the plasmonic metal NPs, the photocurrent and the device efficiency could be increased. Generally, Au and Ag NPs are the most commonly used as metallic materials for triggering plasmonic enhancement in solar cells because of their remarkable SPR optical properties. Several groups have attempted to apply noble metal NPs to improve the performance in DSSCs.

Park et al. fabricated DSSCs based on ~100nm diameter Au NPs embedded in TiO_2 NPs photoanode.[111] As compared with one based on only TiO_2 NPs film, it has strong light absorption and prolonged optical paths by light scattering. However, when the metal NPs are directly exposed to dye molecules or electrolyte, it has problems such as corrosion of metal NPs, recombination or back reaction of the charge carriers leading to loss of charge carriers and poor charge separation at the electrodes. One of the approaches to overcome these problems is to coat the metal NPs with metal oxide shell, such as SiO_2 and TiO_2. It not only preserves the metal NPs from corrosion by I^-/I_3^- electrolyte, but also increases the dye absorption. Therefore, it decreases the thickness of photoanodes and then, maximizes the effect of LSPRs on optical absorption of dye molecules and the PCE of DSSCs with thin photoactive layer.

Qi et al. synthesized core-shell Ag@TiO_2 NPs and fabricated DSSCs.[91] Because the TiO_2 coating of Ag NPs can protect metal

core from electrolyte, as a result, the PCE of DSSCs was enhanced from 7.8% to 9.0% by the high extinction coefficient of Ag NPs. Au NPs coated with silica shells for use in DSSCs were also reported. The DSSCs incorporating Au@SiO_2 NPs demonstrated stable device performance more than one month; this provides evidence that the SiO_2 shells prevent the metal core from being damaged by the electrolyte and dye molecules.[112] The performances of plasmonic DSSCs with two different types of shell materials (i.e. TiO_2 or SiO_2) were compared. Choi et al. prepared Au@TiO_2 NPs and Au@SiO_2 NPs to investigate the effect of the shell material on the performance of the DSSCs. For the DSSC with Au@TiO_2 NPs, it was found that electrons were transferred to the Au core and charged the metal core resulting in higher open circuit voltage (V_{oc}) as a result of the charging effect. While for the DSSC with Au@SiO_2 NPs, the SiO_2 shell prevents electron charging of the metal core, which results in higher J_{sc} by surface plasmonic effect.[113]

The metal oxide shell thickness can influence the plasmonic effect in DSSCs. Liu et al. have studied the effect of the shell thickness on the enhancement effect in plasmonic DSSCs with Au@TiO_2 core-shell NPs by controlling the thickness of the TiO_2 shell. When Au NPs with 5 nm TiO_2 shell were incorporated into DSSCs, the PCE of DSSCs was enhanced from 6 % to 7.38 %, corresponding to a 23% enhancement. When Au@TiO_2 NPs with thinner TiO_2 shell (<5nm) were incorporated into DSSCs, the photocurrent of DSSCs enhanced. While incorporation of the Au@TiO_2 NPs with a thicker shell (>5nm) was enhanced the open-

circuit voltage of DSSCs.[114] Standridge et al. also demonstrated the shell thickness dependence of the plasmon-enhanced properties in DSSCs using Ag@TiO_2 NPs. The DSSC with 2 nm TiO_2 shell thickness exhibited the best efficiency. As the TiO_2 shell thickness increased, the efficiency of the DSSCs with Ag@TiO_2 NPs was decreased due to decrease plasmon coupling between dye molecules and metal NPs. However, since different optimum shell thickness for best efficiency on DSSCs, the thickness of oxide shell needs to be optimized to improve light harvesting and stability.[115] The PCE of the DSSCs is highly dependent on the concentration of core-shell metal NPs. Hossain et al. prepared a series of DSSC with various concentrations of Ag@SiO_2 NPs in order to investigate the effect of the concentration of Ag@SiO_2 NPs on the performance of DSSCs. As the concentration of Ag@SiO_2 NPs on photoanode in DSSCs was increased, the intensity of the light-absorption spectra of the photoanode gradually increased, whereas the amount of dye adsorption decreased. At the optimum Ag@SiO_2 NPs concentration, the DSSCs had a 43.25% increase in the PCE due to increased light absorption of the dye and the light coupling caused by the plasmonic effect from Ag@SiO_2 NPs. However, the excess amounts of Ag@SiO_2 NPs, more than 3 wt%, adversely affected the PCE due to a reduction in the effective surface area of the films and the amount of dye absorbed, as well as an increase in the charge-carrier recombination.[116] Therefore, it is required to use optimal concentration of metal NPs to effectively improve the PCE of the DSSCs.

In addition to, various shaped metal NPs are used in photoanode of DSSCs to maximize broad light absorption and efficiency of DSSCs. The LSPR of metal NPs can be easily modulated by controlling their size and shape. Compared to nanospheres, anisotropic nanoparticles such as cubes, nanoplates, nanorods, and nanostars has higher absorption efficiency and extinction, and electromagnetic field localization at edges and corners, and larger surface area, as shown in Figure 1.8.

Zarick et al. incorporated Au@SiO_2 nanocubes into the photoanodes of DSSCs to enhance light harvesting in DSSCs. Finite difference time domain (FDTD) simulations showed that the light extinction by Au@SiO_2 nanocubes is very high in the 700−900nm due to their strong light scattering and absorption in this region. The photocurrent behavior and IPCE spectra have shown that device performance is controlled by the concentration of Au@SiO_2 nanocubes. Accordingly, the J_{sc} was significantly increased with 1.8 wt% Au@SiO_2 nanocubes, resulting in an enhancement of the PCE from 5.8% to 7.8%, corresponding a 34% improvement in DSSC performance. The best performance of plasmon−enhanced DSSC is attributed to intense electromagnetic fields at the corners and edges of the nanocubes, which increases the plasmonic molecular coupling, amplifying the carrier generation and the efficiency of the DSSC.[117]

Besides, Elbohy et al. incorporated Au nanostars, which have broad and strong NIR light absorption at λ_{max} *ca* 785 nm, into DSSC based on N719 dye. The PCE of the DSSC with Au nanostars was increased by 20%, from 7.1% to 8.4%. Meanwhile, for a DSSC based

on N749 dye, which has longer maximum absorption wavelength (at 410 nm and 610 nm) than N719, the PCE of the DSSC with Au nanostars was increased by 30%, from 3.9% to 5.0%. This improvement of PCE is attributed to the strong and broad LSPRs in the NIR region from 500 nm up to 1,000 nm.[118]

By simply modulating the aspect ratio of the nanorods (NRs), two spectrally separated LSPR bands were created, due to dependence the optical properties of NRs on their aspect ratio. Li et al. fabricated DSSCs with Au NR@SiO_2 composite photoanode. When Au NR@SiO_2, which has its λ_{max} at 514 nm and 656 nm, was incorporate into the DSSCs, the efficiency increased from 5.86% to 7.21%, showing 23% enhancement, compared with that of the DSSCs without Au NR@SiO_2. The improvements in the performance of DSSCs are attributed to the enhancement of the spectral response of the dye that results from the longitudinal plasmon absorption of Au NRs.[119] The Ag NW@SiO_2 core–shell structure had also applied to DSSCs with various concentrations by Guo et al. In the results, the PCE of DSSC was enhanced from 5.45 % to 6.26% by improvement of J_{sc}, from 9.69 mA/cm^2 to 11.83 mA/cm^2. By incorporating of Ag NW@SiO_2, the light absorption and the photon capture ability of the dye molecules were significantly increased, which resulted in improvement of J_{sc} and PCE due to the increased light coupling by the LSPR at 350 nm and 388 nm of AgNW@SiO_2 in the photoanode.[120] Incorporation of triangular nanoprisms and nanoplates in DSSCs was also explored. In contrast to the spherical Ag NPs which have the LSPR absorption at *ca* 400 nm, anisotropic

NPs such as triangular Ag nanoprisms and nanoplates have a red-shifted extinction, and the position of the LSPR can be tuned from the blue-violet to the NIR region by changing the aspect ratio. Incorporation of 0.05 wt% triangular Ag@SiO_2 nanoprisms in the photoanode of DSSCs can significantly improve the PCE by 32% due to an increase the light-harvesting efficiency in the red and NIR regions, 550-750 nm.[121] Kim et al. prepared Ag nanoplates whose extinction maximum wavelengths are 470, 540, 620nm via a rapid thermal process. The panchromatic quasi-manolayer of Ag NPs was fabricated by immobilizing these three kinds of Ag nanoplates on the film coated with poly(4-vinyl pyridine) (P4VP). The LSPR of the panchromatic quasi-monolayer with three kinds of Ag nanoplates takes place over the entire visible region. The efficiency of the DSSC incorporating a quasi-monolayer of Ag NPs improves up to 11.4% due to increased light absorption in the entire visible region.[122]

As well as modulating the shape and size of metal NPs, Alloy NPs incorporated in DSSCs can an effective way to achieve broad plasmonic absorption, high intensity of plasmonic absorption, and the capacity to tune the optical properties, compared with individual NPs. Mostly mixed alloy (Ag-Au alloy) NPs and core-shell bimetal NPs (Au@Ag) were applied in DSSCs to generate better optical properties than mono-metal NPs. As an example of mixed alloy usage, Al-Asawi et al. prepared Ag-Au alloy NPs by a two-step synthesis method, mixing and irradiating the as-prepared Au and Ag colloids. After being irradiated by the laser pulses, the mixed Au and

Ag suspension exhibited a broad single absorption peak at 501 nm. The DSSC with Au–Ag alloy NPs had maximum values of J_{sc} and PCE equal to 11.67 mA/cm^2 and 5.81%, respectively. Compared with the DSSC without Au–Ag alloy NPs, the PCE in these DSSCs had 52.1% of improvement as a result of incorporating Au–Ag alloy NPs.

This result is ascribed to broad optical absorption of dye molecules because of the plasmonic effects of Au–Ag alloy NPs.[123] DSSCs with popcorn–shaped Au–Ag alloy NPs were fabricated by Huang and co–workers. The irregular popcorn–shaped Au–Ag alloy NPs enhance the absorption from 350 nm to 800 nm. At 2.38 wt% of popcorn–shaped Au–Ag alloy NPs, the PCE of their DSSCs had a 16% improvement, from 5.26% to 6.09%, because of the broad light absorption band.[124] Alloy NPs with core–shell bimetal NPs have also been synthesized, and applied in DSSCs. Yun et al. synthesized hollow TiO_2 nanoparticles (HNPs) decorated with Au@Ag core–shell nanoparticles (Au@Ag/TiO_2 HNPs). In the UV–visible spectra, the Au@Ag/TiO_2 HNPs exhibited stronger and broader absorption from 350 nm to 800 nm. When 0.2 wt% of Au@Ag/TiO_2 HNPs were incorporated into the photoanode, the PCE was enhanced from 7.8% to 9.7%, corresponding to a 24% enhancement. This improvement is due to the broad light–absorption band, which results in enhanced light–harvesting efficiency.[125] Dong et al. introduced Au@Ag NRs in the photoanode to achieve both increased adsorption by the dye and a broad light–absorption band on the photoanode. The Au@Ag NRs have a wider plasmonic region from 350 to 900 nm with stronger peaks than simple Au nanostructures. In the DSSC with

3.68 wt% Au@Ag NRs, the PCE reached 8.43% with 16.53 mA/cm^2 of optimized photocurrent, which was almost a 40% increase compared to the DSSCs without Au@Ag NRs. The improvement can be mainly attributed to the strong plasmonic absorption and effective light-harvesting efficiency in the visible and NIR region by the introduction of Au@Ag NRs.[126]

Chapter 2

Experimental Details

2. 1. Preparation of Metal nanoparticles

2. 1. 1. Synthesis of Ag seeds

0.30 mL of 10 mM silver nitrate ($AgNO_3$) solution is inserted in 20 mL of 1 mM trisodium citrate solution with stirring vigorously. After 3~5min, 1.8 mL of 10 mM sodium borohydride ($NaBH_4$) is rapidly added to the solution and mixture is stirred vigorously for 5min. Finally, it turns out light yellow Ag seeds solution. After aging for 3h at room temperature, the Ag seeds solution is used.

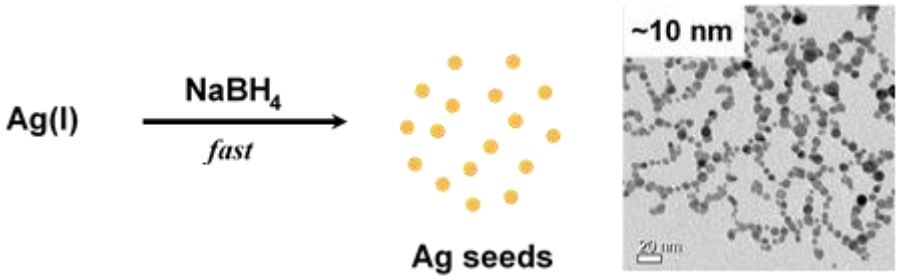

Figure 2. 1. Scheme of preparation of Ag seeds solution

2. 1. 2. Synthesis of Ag nanoparticles

Ag nanoparticles are fabricated via seed-growth method.[127] Each 6, 9, 10, 12 mL of the Ag seed solution is mixed with 14, 11, 10, 8 mL of distilled water, respectively. (Total solution: 20mL) 1.2 mL of 20 mM sodium ascorbate solution are inserted in mixed solution. To this solution, 1.2 mL of 10 mM $AgNO_3$ solution is rapidly inserted and mixture stirred vigorously. The fabricated Ag nanoparticle solution has absorption near 400nm as shown in Figure 2. 3(a). By modulating amount of Ag seed solution, the average size of Ag nanoparticles can be controlled as shown in Figure 2. 3(b).

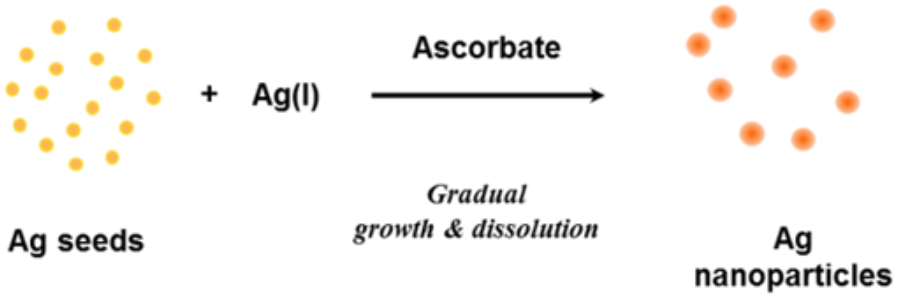

Figure 2. 2. Scheme of preparation of Ag nanoparticles

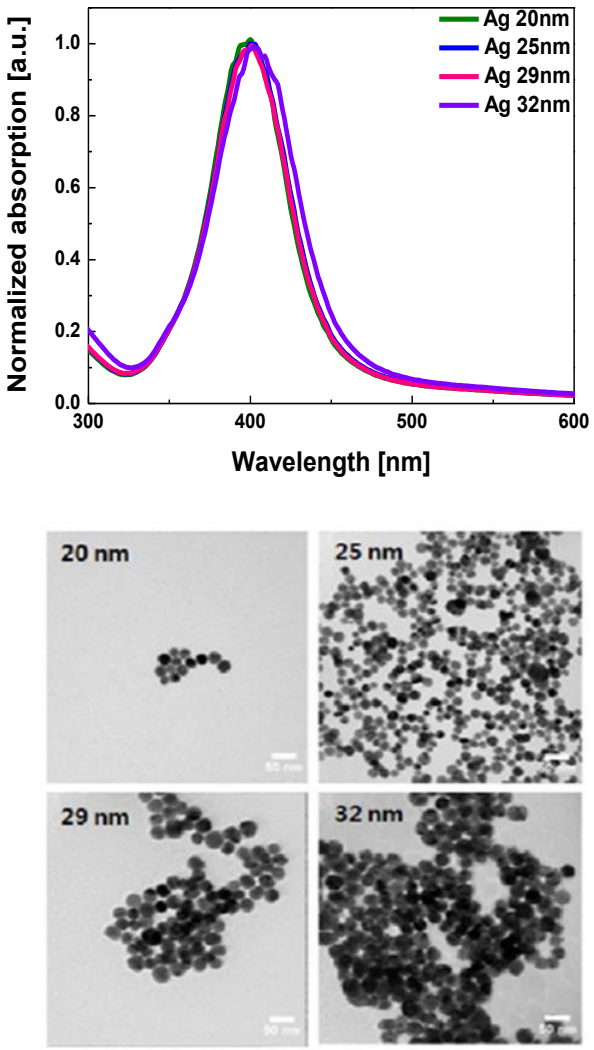

Figure 2. 3. (a) UV-visible spectra and (b) TEM images of prepared Ag nanoparticles with 6, 9, 10, 12 mL Ag seed solution, respectively. The average size of Ag nanoparticles is 20, 25, 29, 32 nm respectively.

2. 1. 3. Synthesis of Au nanoparticles

Au nanoparticles are fabricated by Turkevich method.[128] 0.5 mM of $HAuCl_4$ (50 mL) is heated to boiling point for 1 h. 0.3−1.5 mL of a 1% sodium citrate solution is added to the $HAuCl_4$ solution. And the resulting mixture, which colors light red, is kept for 30 min under stirring at 100 ℃. And then the Au nanoparticle solution is slowly cooled at room temperature. The fabricated Au nanoparticle solution has absorption near 520nm as shown in Figure 2. 5(a). By modulating amount of sodium citrate solution, the average size of Au nanoparticles can be controlled as shown in Figure 2. 5(b).

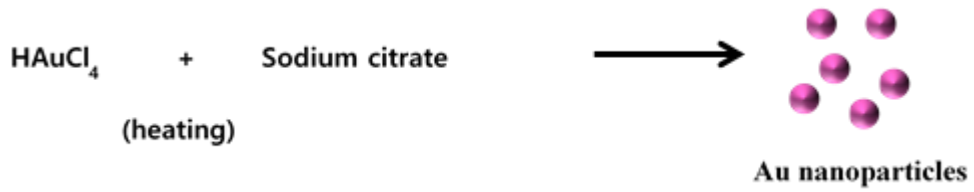

Figure 2. 4. Scheme of preparation of Au nanoparticles

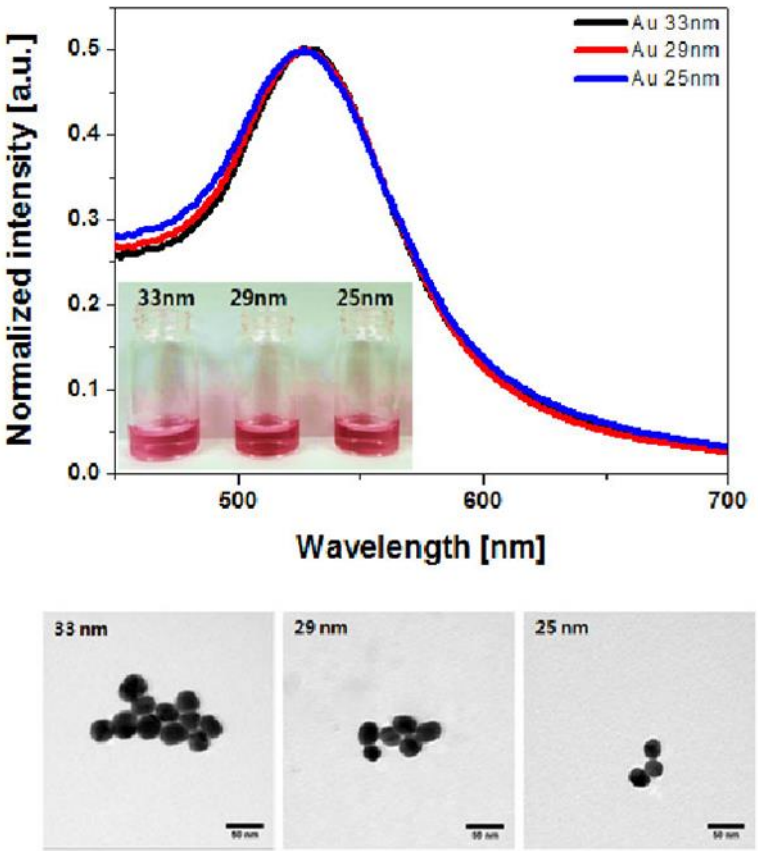

Figure 2. 5. (a) UV-visible spectra and (b) TEM images of prepared Au nanoparticles with different amount of sodium citrate solution.

2. 2. Fabrication of DSSCs

FTO glass is cleaned in ultrasonic bath with detergent, DI water, and acetone for 30min, respectively. A TiO_2 blocking layer is deposited on FTO glass by spin-coating with 5 wt% of titanium di-isopropoxidebis(acetylacetonate) in butanol and sintered at 450 ℃ for 30min. To deposit the mesoporous TiO_2 photoactive layer, TiO_2 pastes (T/SP, solaronix) is doctor bladed on the TiO_2 blocking layer. The photoanode with TiO_2 film is sintered in air at 450 ℃ for 30min. Sequentially, the scattering layer (DSL 18NR-AO, Dyesol) is doctor bladed on the mesoporous TiO_2 photoactive layer and sintered in air at 450 ℃ for 30min. The TiO_2 photoanode of DSSC is treated by dipping with titanium isopropoxide (TIP) solution (0.1 M in isopropyl alcohol) at 90 ℃ for 30 min, and followed by sintering at 450 ℃ for 30 min. The TiO_2 photoanode is immersed into a N719 (solaronix) dye solution in ethanol under heating at 50 ℃ oven for overnight. To prepare the Pt-deposited counter electrode, H_2PtCl_6 solution (0.5 M in EtOH) is dropped onto FTO glass and sintered at 400 ℃ for 30 min. The TiO_2 photoanode and the Pt counter electrode are sandwiched by a 60 ㎛-thick surlyn. The liquid electrolyte is composed of 0.7 M of 1 butyl -3-methyl imidazolium iodide (BMII), 0.03 M of I_2, 0.1 M of guanidium thiocyanate (GSCN), and 0.5 M of 4 tert-butyl pyridine (TBP) in a mixture solution of acetonitrile and valeronitrile (85: 15 v/v). The active area of DSSCs is 0.25 cm^2. Figure 2.6 shows the scheme of the DSSC fabrication process.

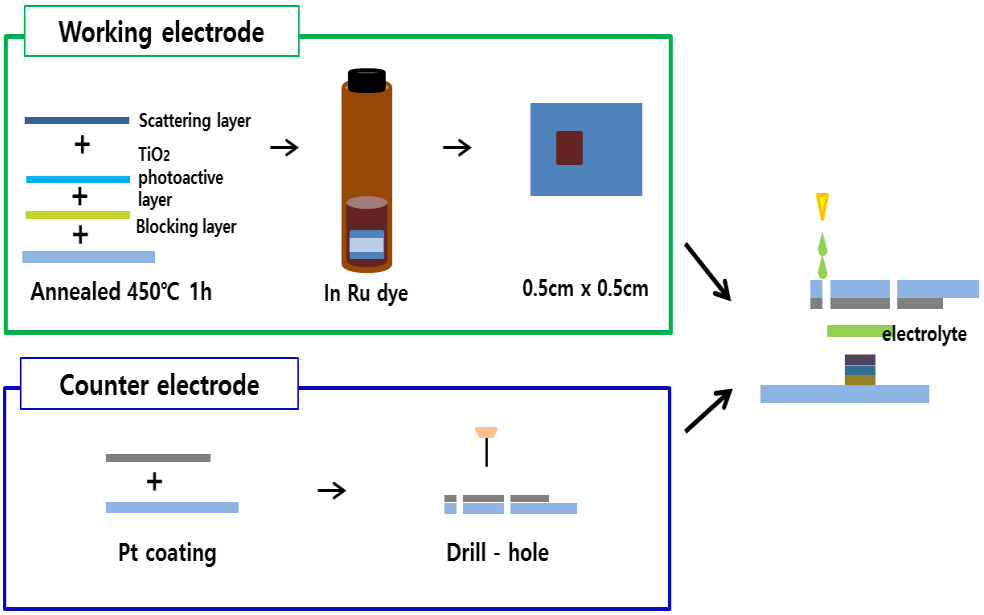

Figure 2. 6. The scheme of the DSSC fabrication process.

2. 3. Characterizations

2. 3. 1. UV-visible spectroscopy

The ultraviolet and visible (UV-Vis) spectroscopy measures the amount of the absorbed and scattered light from sample. By UV-visible spectroscopy measurement, the absorption, reflectance and transmittance of various samples in ultraviolet (UV), visible and near-infrared (NIR) ranges can be obtained.

In these experiments, the absorption spectra of Au, Ag colloid and dye solutions and the extinction spectra films with immobilized Au and Ag NPs were analyzed by UV-visible spectroscopy, Neosys-2000 system (Scinco). Samples are prepared as following; the liquid samples are placed in a cuvette, and the samples of the metal nanoparticles are immobilized on the surface of cover glass or TiO_2 film with P4VP. After preparation of blank sample for zero, the sample is inserted and measured. The measured wavelength range is 200-1000 nm in these experiments.

2. 3. 2. Field emission scanning electron microscope (FE-SEM)

The Au and Ag nanoparticles are immobilized on cover glass. These samples are pasted on the sample holder with carbon tape. The samples on the holder are coated by Pt. The shape and size of metal NPs and the surface morphology of fabricated films are confirmed by measurement of a field emission scanning electron microscope (FE-SEM, MERLIN Compact, ZEISS Inc.). The MERLIN Compact offers the 1.0nm resolution at the 15kv and the 1.7nm resolution at the 1kv. We can use accelerating voltage 10 kv, emission current 20 μA and 4.4×10^{-5}Pa vacuum. The SEM images are obtained in the magnification from 50,000 to 120,000 times. And energy dispersive x-ray spectroscopy (EDS) analysis is used to investigate the elements in double layered DSSCs based on Au NPs/TiO_2 and Ag NPs/TiO_2.

2. 3. 3. Energy filtered transmittance electron microscope (EF-TEM)

The morphological, compositional and crystallographic information are obtained by the transmittance electron microscope (TEM). To confirm the structure and size of metal nanoparticles, the images of an energy-filtered transmittance electron microscope (EF-TEM) are obtained by measurement of a Carl Zeiss, LIBRA 120.

2. 3. 4. Solar simulator

When the characteristics of the DSSCs are measured, it requires to stable light source which is closely the sunlight. A solar simulator is a light source which provides illumination similar to the sunlight and can be measured the characteristics of the DSSCs in indoor laboratory environments. Under AM 1.5 illumination (100 mW/cm^2) provided by a solar simulator (1 kW xenon with AM 1.5 filter, PEC-L01, Peccel Technologies), current density–voltage (*J*–*V*) characteristics of the DSSCs are measured by using an electrometer (KEITHLEY 2400).

2. 3. 5. Incident photon-to-current conversion efficiency (IPCE)

To know ability to convert the incident light into electricity of device, the external quantum efficiency (EQE) spectra are measured by using Polaronix K3100 IPCE measurement (McScience) with a 300 W xenon lamp light source. A standard single-crystal Si cell is used as reference to calibrate the intensity of the light at each wavelength.

2. 3. 6. Electrochemical impedance spectroscopy (EIS)

The electrochemical impedance spectroscopy (EIS) is a convenient measurement to investigate the electron transport properties and resistance in DSSC. The EIS is measured with a potentiostat (Solartron 1287) and a frequency response analyzer (Solartron 1260) over the frequency range from 10^{-1} to 10^{5} Hz. The applied bias voltage and AC amplitude are set at open circuit voltage (V_{oc}) of the DSSCs and 10 mV, respectively. The impedance measurements are performed at V_{oc} under one-sun light illumination (AM 1.5G, 100mW/cm^2).

Chapter 3

Surface plasmon-enhanced dye-sensitized solar cells based on double-layered composite films consisting of TiO_2/Ag and TiO_2/Au nanoparticles

3. 1. Overview

We have prepared Ag and Au nanoparticles (NPs) whose maximum absorption wavelengths are near 390nm and 530nm respectively. By using them, we fabricated surface plasmon-enhanced dye-sensitized solar cells (DSSCs) based on N719 dye. The N719 dye, which is the most greatly applied dye molecules in DSSCs, has two bands of strong absorbance centered at 393 nm and 533 nm. The localized surface plasmon absorption band of Ag NPs was well matched with the higher energy band of N719 dye, while that of Au NPs matched with the lower one.

Therefore, Ag and Au NPs were incorporated together in DSSCs to enhance two absorption bands of N719 dye at the same time for highly efficient DSSCs. We fabricated plasmonic DSSCs based on double layered composite films consisting of Ag-TiO_2 and Au-TiO_2 composite film.

We fabricated and compared conventional DSSCs, plasmonic DSSC and double-layered plasmonic DSSC to demonstrate the localized surface plasmon resonance (LSPR) effect of Ag and Au NPs on photovoltaic characteristics of DSSCs. By including metal NPs, the efficiency of DSSCs improved. The efficiency of DSSC based on double-layered composite film with Ag-TiO_2 and Au-TiO_2 composite films was higher than that of single-layered composite film with Ag-TiO_2 or Au-TiO_2 composite film. By optimizing the weight percent of Ag and Au NPs to TiO_2 NPs and the geometry of Ag-TiO_2 and Au-TiO_2 composite film in double-

layered plasmonic DSSC, the PCE significantly improved from 8.42% to 10.03%, corresponding 19% enhancement. The high efficiency of double-layered plasmonic DSSC might be due to a well optical spectra matching between the LSPRs of Ag and Au NPs and two strong absorption bands of N719 dye. For double-layered plasmonic DSSCs, the plasmonic metal NPs were dispersed into the TiO_2 photoactive layer and play a role as light harvesting and charge separation sites. By LSPR effect of Ag and Au NPs, the electric field around the metal NPs enhances and the light absorption cross section of the dye and the number of generated photoelectrons increase which in turn increases the efficiency of DSSCs.

3. 2. Fabrication of double-layered plasmonic DSSCs

As the photoactive layer, the mixtures consisting of metal (Ag or Au) NPs and TiO_2 NPs were prepared using the following procedure: By sonication and stirring, metal NPs were mixed with TiO_2 NP paste (T/SP, Solaronix) in ethanol with various weight percent, from 0 to 1.05 wt%. In case of the bare metal NPs, they are corroded by directly contacting the electrolyte and results in the back reaction and the recombination of charge carriers. To resolve the problems, the surfaces of metal NPs were coated with metal oxide layer such as TiO_2. By pretreating with titanium isopropoxide (TIP), the surfaces of Ag and Au NPs were coated with TiO_2. The solvent in the mixture was evaporated in vacuum for metal-TiO_2 paste with suitable viscosity. The TiO_2 paste or the metal-TiO_2 paste was deposited onto the blocking layer by the doctor blade technique. Firstly, Ag-TiO_2 paste was coated, and then Au-TiO_2 paste was coated on the Ag-TiO_2 layer. It was annealed gradually at 450 ℃ for 30 min. A TiO_2 scattering paste (DSL 18NR-AO, Dyesol) was deposited on the double-layered TiO_2 layer with Ag and Au NPs by doctor blade technique and annealed gradually at 450 ℃ for 30min. The photoactive films were treated in titanium isopropoxide (TIP)solutions (0.1 M in isopropyl alcohol) at 90 ℃ for approximately 30 min, and followed by annealing at 450 ℃ for 30 min. The TiO_2 or metal-TiO_2 films were dipped into a N719 (Solaronix) dye or black dye solution in ethanol at 50 ℃ for overnight.

3. 3. Result and Discussion

3. 3. 1. Characterization of metal nanoparticles

3. 3. 1. 1. TEM images of Ag and Au nanoparticles

Figure 3.1 shows the TEM images of Ag and Au NPs. Ag NPs were prepared by seed mediated growth method. Au NPs were prepared by Turkevich method. Ag NPs were synthesized with various sizes by adjusting amount of Ag seeds. And Au NPs were synthesized with various sizes by adjusting amount of sodium citrate. As shown in Figure 3.1, the shape of Ag and Au NPs is spherical and the average size of them is about 29nm and 33nm respectively.

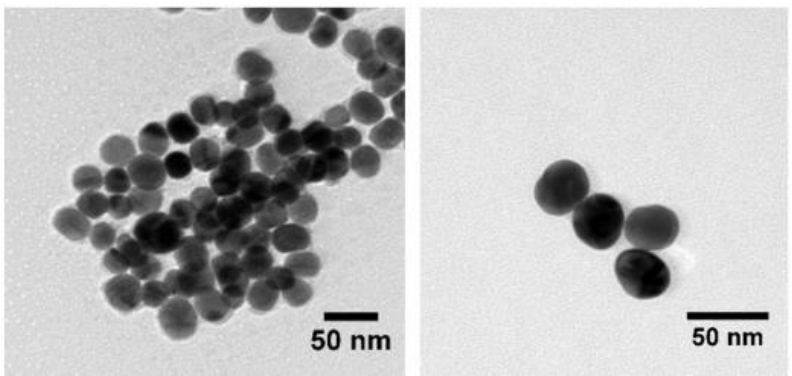

Figure 3. 1. The TEM images of colloidal silver (left) and gold (right) NPs.

3. 3. 1. 2. UV-visible spectra of Ag and Au nano particles

Figure 3.2 shows the UV-visible extinction spectra of Ag and Au colloid solutions and comparison to the UV-visible absorption spectrum of N719 dye. The maximum extinction wavelength (λ_{max}) of Ag colloid solution is near 390 nm, while that of Au colloid solution is near 530 nm. In the absorption spectrum of N719 dye, it exhibits two strong absorption band centered at 393 nm and 533nm. The extinction band of Ag NPs was well matched with the higher energy absorption band of N719 dye, while that of Au NPs matched with the lower one. Therefore, the extinction bands of Ag and Au NPs are well matched with two strong absorption bands of N719 dye.

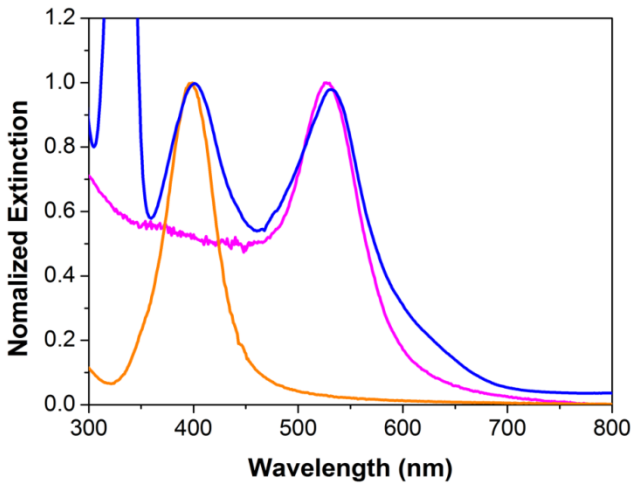

Figure 3. 2. UV-visible absorption spectrum of N719 dye (blue) and extinction spectra of silver (orange) and gold (pink) colloid solutions.

3. 3. 2. Photovoltaic properties of double-layered plasmonic DSSCs

To investigate the LSPR effect of Ag and Au NPs on photovoltaic parameters of DSSCs, three types of DSSCs, (1) conventional DSSCs, (2) plasmonic DSSC and (3) double-layered plasmonic DSSC, were fabricated. The conventional DSSC is based on only TiO_2 NPs. The plasmonic DSSC is based on a composite film consisting of TiO_2 NPs and one kind of metal NPs (Ag or Au NPs). And the double-layered plasmonic DSSC is based on two composite films consisting of Ag-TiO_2 NPs and Au-TiO_2 NPs. When metal NPs were incorporated in plasmonic DSSCs, pretreatment with TIP (titanium(IV)isoproxide, Aldrich) was required to prevent the corrosion of metal NPs and photo-generated charge recombination by electrolyte and dye molecules.[113, 129, 130] Hence, all of the metal NPs were pretreated with TIP and the surfaces of metal NPs were coated with TiO_2.

Figure 3.3(a) shows the photocurrent density-voltage (*J-V*) curves measured from the DSSCs based on the film of only TiO_2 NPs, composite film of Ag-TiO_2 NPs or composite film of Au-TiO_2 NPs, and double-layered film consisting of Ag-TiO_2 NPs and Au-TiO_2 NPs. The photovoltaic parameters of these DSSCs are listed in Table 3.1. By incorporating metal NPs, the short-circuit current (J_{sc}) increased substantially, while the open-circuit voltage (V_{oc}) and fill factor (*ff*) unchanged significantly. For the plasmonic DSSC based on Ag-TiO_2 NPs composite film, J_{sc} increased from 14.94 mA/cm^2 to

15.86 mA/cm^2. For the plasmonic DSSC based on Au−TiO_2 NPs composite film, J_{sc} increased from 14.94 mA/cm^2 to 16.67 mA/cm^2. For the double−layered plasmonic DSSC, the J_{sc} increased from 14.94 mA/cm^2 up to 18.17 mA/cm^2, which was the highest value. The increase in J_{sc} of the plasmonic DSSCs is due to the enhanced light−harvesting properties of the plasmonic metal NPs.

Consequently, the double−layered plasmonic DSSC had the highest PCE of DSSC, 10.03%, corresponding 19.12 % enhancement compared to that of DSSC based on only TiO_2 NPs film. The PCE of the DSSC based on double−layered film was higher than that of single−layered film.

Figure 3.3(b) shows IPCE spectra measured from the DSSCs based on the film of only TiO_2 NPs, composite film of Ag−TiO_2 NPs or composite film of Au−TiO_2 NPs, and double−layered film consisting of Ag−TiO_2 NPs and Au−TiO_2 NPs. By incorporating metal NPs, the values of IPCE over the wavelength range 400 nm to 700 nm were enhanced. In the double−layered plasmonic DSSC, the integrated IPCE value showed higher than that from the DSSC without metal NPs by a factor of 1.28. The relative intensity of IPCE spectra seems to be related considerably to the spectral overlap between the extinction bands of Ag and Au NPs and absorption bands of N719 dye. The relative intensity near 530 nm was stronger in the spectrum of the DSSC based on Au−TiO_2 NPs composite film than that of the DSSC based on Ag−TiO_2 NPs composite film.

Thus, the improvement in efficiency and IPCE values of the double−layered plasmonic DSSCs is due to the LSPR effect of Ag

and Au NPs. For double-layered plasmonic DSSCs, the plasmonic metal NPs were dispersed into the TiO_2 photoactive layer and play a role as light harvesting and charge separation sites. By LSPR effect of Ag and Au NPs, the electric field around the metal NPs enhances and the light absorption cross section of the dye and the number of generated photoelectrons increase which in turn increases the efficiency of DSSCs.

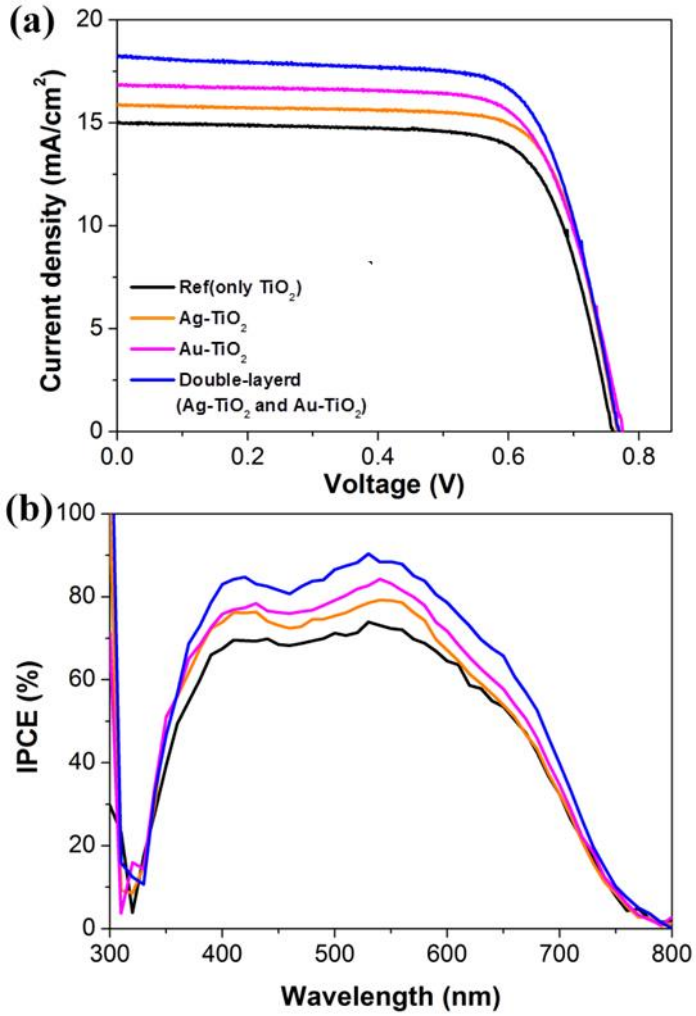

Figure 3. 3. (a) Photocurrent density−voltage ($J-V$) curves and (b) IPCE spectra measured from the conventional DSSC (only TiO_2 NPs), plasmonic DSSCs(Ag−TiO_2 NPs film or Au−TiO_2 film) and double−layered plasmonic DSSCs (Ag−TiO_2 NPs film at bottom and Au−TiO_2 film at top).

Table 3. 1. Photovoltaic parameters of the conventional DSSC (only TiO_2 NPs), plasmonic DSSCs (Ag−TiO_2 NPs film or Au−TiO_2 film) and double−layered plasmonic DSSCs (Ag−TiO_2 NPs film at bottom and Au−TiO_2 film at top). The concentration of Ag and Au NPs in plasmonic DSSCs is 0.7 wt% and 0.52 wt%, respectively.

	J_{sc} (mA/cm²)	V_{oc} (V)	ff (%)	η (%)
TiO_2 film	14.94	0.76	0.74	8.42
Ag- TiO_2composite film	15.86	0.77	0.74	9.04
Au-TiO_2composite film	16.67	0.78	0.72	9.36
Double-layered film	18.17	0.77	0.72	10.03

3. 3. 3. Plasmonic effect in double-layered plasmonic DSSCs

To demonstrate the plasmonic effect from Ag and Au NPs, the UV-visible extinction spectra of TiO_2 NPs film and double-layered film consisting of Ag-TiO_2 NPs and Au-TiO_2 NPs before and after N719 dye adsorption were measured as shown in Figure 3. 4. All of the films were conducted with TIP treatment. Before N719 dye adsorption, the significant increase in the intensity of the UV-visible extinction spectra didn't show. While after N719 dye adsorption, there was a significant difference in the intensity of the UV-visible extinction spectra. The intensity of the peaks corresponding to the LSPRs of Ag and Au NPs, near 390 and 530 nm, was significantly higher in the extinction spectrum measured from the double-layered film consisting of Au-TiO_2 NPs and Ag-TiO_2 NPs than that measured from the TiO_2 NPs film. The number of dye molecules adsorbed on both films was almost equal, since the thickness of both films was the same as about 5 μm. The higher extinction intensity is due to the plasmonic effects of metal NPs. An enhanced light absorption of dye molecules could take place on or near surface of metal NPs and far surface of metal NPs. The LSPR decays either radiative such as absorption, scattering or into quasi- particles such as formation of electron-hole (e-h) pairs.[132, 133] Therefore, the absorption of dye molecules adsorbed on or near the surface of metal NPs could be enhanced greatly by the latter decay path.

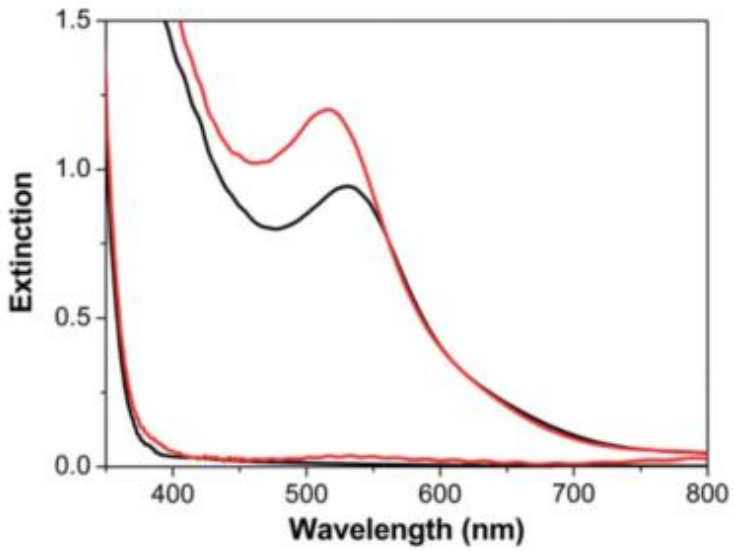

Figure 3. 4. Extinction spectra of TiO_2 NPs film (black) and double-layered film consisting of Ag- TiO_2 NPs and Au-TiO_2 NPs (red) before (bottom two spectra) and after N719 dye adsorption. Both films were treated with TIP before adsorption of dye molecules.

3. 3. 4. EIS of double-layered plasmonic DSSCs

To investigate charge transfer resistance at the interfaces in the DSSCs, we measured the characteristic electrochemical impedance spectroscopy (EIS) spectra for DSSCs. Figure 3.5 shows the Nyquist plot of the EIS for DSSCs based on TiO_2 film and double-layered film with Ag-TiO_2 and Au-TiO_2 NPs. The equivalent circuit is shown as the inset. In Nyquist plot of DSSCs, each spectrum contains three distinct semicircles. The first semicircle in the high-frequency region is determined to the parallel combination of the resistance and capacitance at the Pt-FTO/electrolyte and to the uncovered FTO/electrolyte. It is attributed to mainly charge transfer at Pt/electrolyte interfaces. The second semicircle in the intermediate frequency region is determined to the electron diffusion in the TiO_2 film and electron back reaction with electrolyte at the TiO_2/electrolyte interface. It is attributed to the resistance and capacitance at the TiO_2/electrolyte interface. The third semicircle in low-frequency regions is determined to the diffusion process of I_3^- in the electrolyte solution.[135]

To investigate effect of metal NPs on electrochemical impedance characteristics, the second semicircle, which determines the electron diffusion in the TiO_2 film and electron back reaction with electrolyte at the TiO_2/electrolyte interface, is mainly important. In Nyquist plot of the EIS of DSSCs, the two EIS spectra have no significant difference. It might be represented that a relatively low weight percent of Ag and Au NPs does not affect to the resistance

and capacitance of the DSSCs.

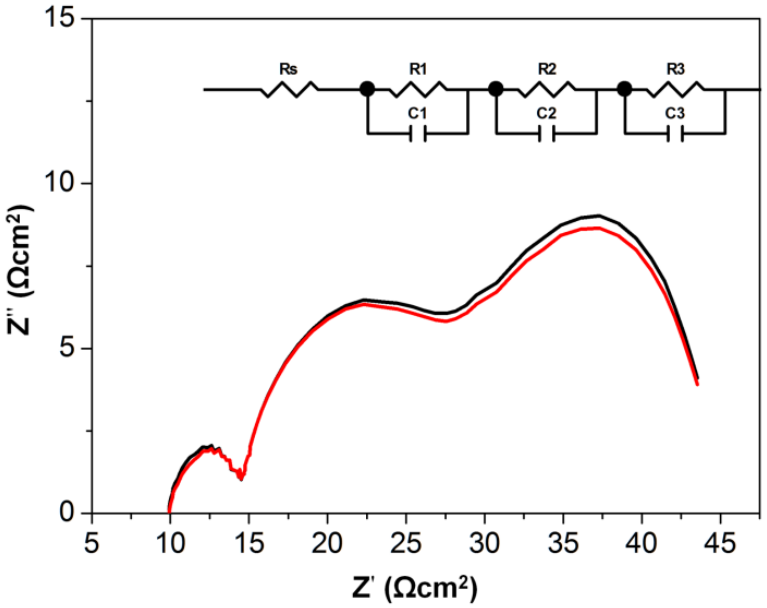

Figure 3. 5. The Nyquist plot of the electrochemical impedance spectra (EIS) of DSSCs based on TiO_2 film (black) and double-layered film consisting of Ag-TiO_2 and Au-TiO_2 NPs (red).

3. 3. 5. Optimization of plasmonic DSSCs

3. 3. 5. 1. Optimization depends on geometry of metal nanoparticles composite film

The photoactive layer of double-layered plasmonic DSSC was composed of Ag-TiO_2 film, Au-TiO_2 film and scattering layer. It can be confirmed by the cross-section SEM image as shown in Figure 3.6. Through energy dispersive x-ray (EDX) spectroscopy on the SEM, the position of Ag and Au NPs in composite film of double-layered plasmonic DSSC can be determined as shown in Figure 3.7.

For highly efficient DSSCs, several factors were optimized. The PCE, η of DSSC is affected by geometry of two composite films with Ag or Au NPs. To optimize the geometry condition, we fabricated double-layered plasmonic DSSCs with different geometry. One is composed of Ag-TiO_2 film at bottom and Au-TiO_2 film at top. Another is composed of Au-TiO_2 film at bottom and Ag-TiO_2 film at top. With the geometry of the composite film consisting of Ag-TiO_2 NPs under that of Au-TiO_2 NPs, the efficiency was higher than the upside down geometry as shown in Table 3.2. The dependence of the η on geometry is due to difference of absorption and scattering wavelength in Ag and Au NPs. Ag NPs could absorb and scatter much shorter wavelength light than Au NPs, since the LSPR of Ag NPs centered at 390 nm in relative shorter wavelength region, while

that of Au NPs at 530 nm in relative longer wavelength region. The weight percent of Ag or Au NPs to the TiO_2 NPs is less than 1%, and TiO_2 NPs are the dominant species. Therefore, the incident light may be reduced mostly by the scattering of TiO_2 NPs, since TiO_2 NPs have no absorption in visible region. With increasing the optical path length, relative loss of shorter wavelength light is greater than that of longer wavelength light. Therefore, a better efficiency might be achieved from the DSSC whose composite film included Ag NPs, which absorb and scatter much shorter wavelength light than Au NPs, was placed at bottom, which was the front under front side illumination.

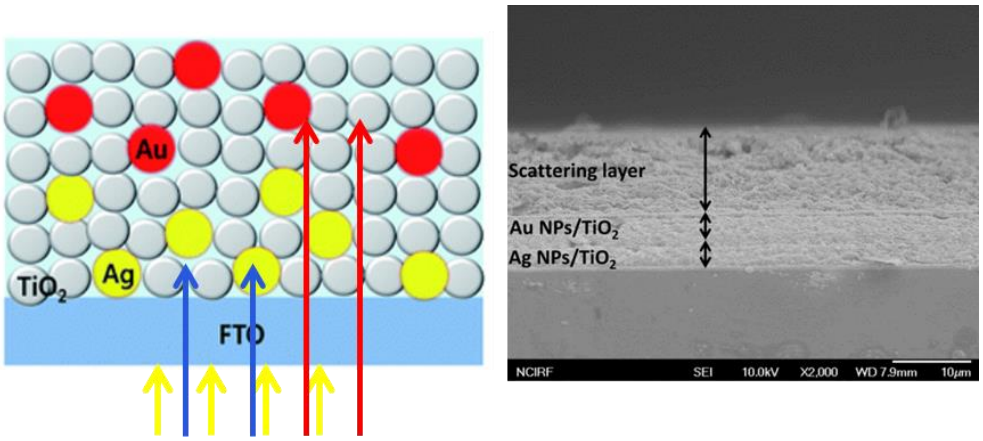

Figure 3. 6. Structure (left) and cross-section SEM image (right) of double-layered dye-sensitized solar cells based on composite films consisting of Ag-TiO_2 and Au-TiO_2 nanoparticles

Table 3. 2. The photovoltaic parameters of the double-layered DSSCs dependent of geometry of metal nanoparticles composite film

	J_{sc} (mA/cm²)	V_{oc} (V)	*ff* (%)	*h* (%)
Reference (without metal NPs)	15.06	0.79	0.73	8.69
The composite film consisting of **Ag and TiO_2 NPs is at bottom**	17.14	0.78	0.75	10.05
The composite film consisting of **Au and TiO_2 NPs is at bottom**	16.71	0.78	0.74	9.65

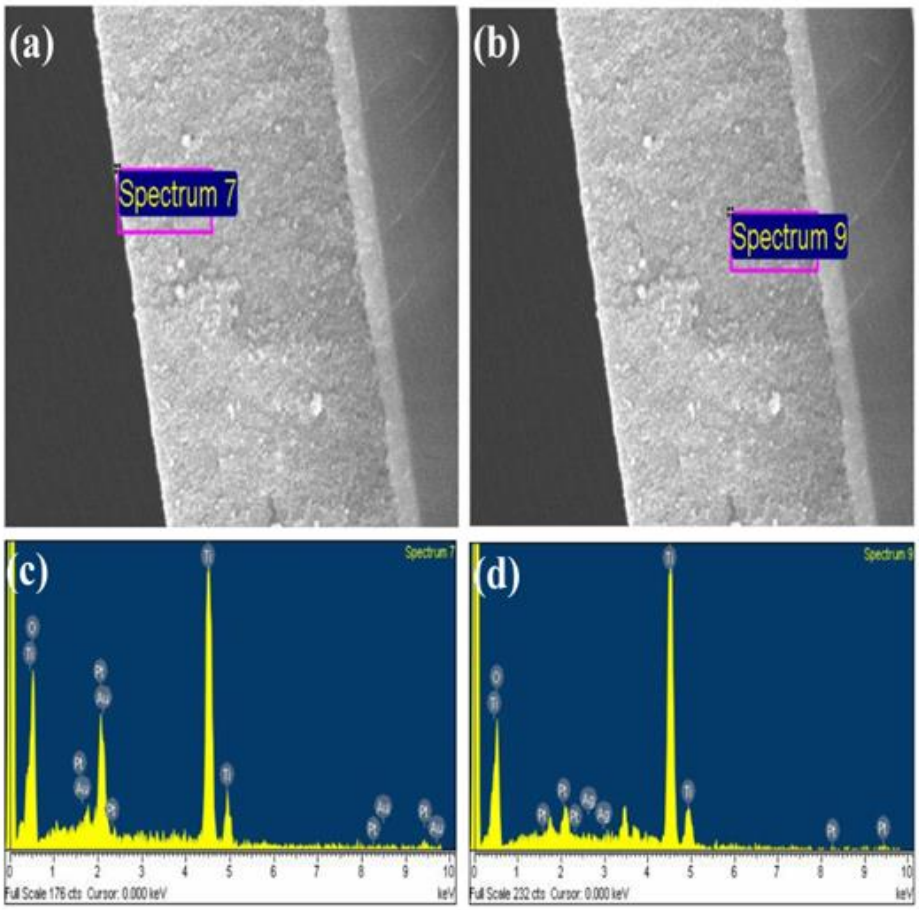

Element	Weight%	Atomic%
O K	42.38	73.92
Ti K	40.58	23.64
Pt M	16.79	2.40
Au M	0.25	0.03
Totals	100.00	

Element	Weight%	Atomic%
O K	40.61	69.18
Ti K	52.34	29.78
Ag L	0.48	0.12
Pt M	6.57	0.92
Totals	100.00	

Figure 3. 7. SEM images (a, b) and EDX spectra (c, d) of the cross section of the double-layered composite films consisting of Ag-TiO_2 and Au-TiO_2 nanoparticles.

3. 3. 5. 2. Optimization depends on concentration of metal nanoparticles

The efficiency of the DSSCs is affected by the concentration of metal NPs to TiO_2 NPs. To optimize concentration of metal NPs, the dependence of the PCE (η) and J_{sc} of plasmonic DSSCs on weight percent of Ag or Au NPs was investigated, respectively.

Figure 3.8 shows the $J-V$ curves of the DSSCs based on Ag-TiO_2 NPs film (Ag-TiO_2 DSSCs) with various weight percent of Ag NPs. The photovoltaic parameters of Ag-TiO_2 DSSCs are listed in Table 3.3. The J_{sc} increased from 14.94 mA/cm^2 to 15.86 mA/cm^2 as the weight percent of Ag NPs raised up to 0.70 wt%. And then, η and J_{sc} gradually decreased over 0.7wt% of Ag NPs. For Ag-TiO_2 DSSCs, the highest value of η, 9.04%, was obtained when the weight percent of Ag NPs was 0.70 wt%.

Figure 3.9 shows the $J-V$ curves of the DSSCs based on Au-TiO_2 NPs film (Au-TiO_2 DSSCs) with various weight percent of Au NPs. The photovoltaic parameters of Au-TiO_2 DSSCs are listed in Table 3.4. As the weight percent of Au NPs raised up to 0.52 wt%, the η of the Au-TiO_2 DSSCs gradually increased from 8.42% up to the maximum value, 9.36%. Further increase in the weight percent of Au NPs to 1.05 wt% actually caused a decrease in the η values to 9.03%.

In conclusion, when 0.7wt% Ag NPs or 0.52wt% Au NPs are mixed in TiO_2 film of DSSCs, it has the best efficiency of each plasmonic DSSC as shown in Figure 3.10.

With increasing the weight percent of metal NPs to TiO_2 NPs, the PCE of the plasmonic DSSCs increased up to a specific weight percent, and then it decreased over that weight percent. In case of J_{sc}, it has also same tendency as that of the η. This behavior is related to the plasmon-enhanced dye absorption and aggregation of metal NPs. To demonstrate it, we have studied the dependence of Au NPs weight percent on $J-V$ curves of the Au-TiO_2 DSSCs adsorbed N719 dye or black dye. Figure 3.11 shows the $J-V$ curves of Au-TiO_2 DSSCs based on black dye with various weight percent of Au NPs. The photovoltaic parameters of them are listed in Table 3.5. As increasing the weight percent of Au NPs, the η value continuously increased from 1.24 % to 2.08 %. In case of J_{sc}, it has also same tendency as that of the η. In contrast to Au-TiO_2 DSSCs with N719 dye, the η and J_{sc} of Au-TiO_2 DSSCs with black dye continuously increased as increasing the weight percent of Au NPs to TiO_2 NPs as shown in Figure 3.12. The dependence of Au NPs weight percent on IPCE spectra of the Au-TiO_2 DSSCs based on N719 dye or black dye also compared as shown in Figure 3.13. For black dye, the IPCE values increased continuously with increasing the weight percent of Au NPs, while for N719 dye, the values decreased steeply when the weight percent of Au NPs increased further than 0.52 wt%. This tendency is same as that of the

dependence of metal NPs weight percent on η and J_{sc} values as shown in Figure 3.12.

With increasing weight percent of Au NPs, the probability of aggregation between Au NPs in the composite films would be increased, and the concentration of the dimer Au NPs might be increased. The resonance wavelength of the longitudinal mode of the monomer Au NPs centered at near 540nm. When Au NPs aggregated, the resonance wavelength of the longitudinal mode of the dimer Au NPs was red-shifted and centered at near 760nm. N719 dye has two strong visible absorption bands centered at 393nm and 533nm, while black dye centered at 410nm and 610nm. It is suggested that the spectral overlap with black dye (absorption band centered at 410 nm and 610 nm), is much greater for the dimer of Au NPs (centered at near 760nm) than the monomer (centered at near 540 nm), while that with N719 dye (centered at 393 nm and 533 nm) is much lesser for the dimer than the monomer. The plasmon-enhanced absorption increases with increasing the spectral overlap between the LSPRs of metal NPs and absorption of dye molecules which results in enhance the efficiency of the surface plasmon-enhanced DSSCs.[134] Therefore, to fabricate a high PCE of plasmonic DSSCs, it is required to prevent from the aggregation of metal NPs in the process of the composite film with TiO_2 and metal NPs.

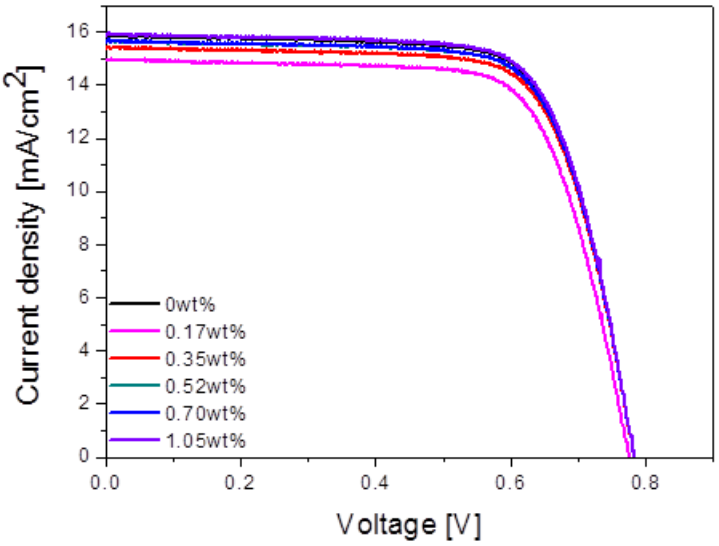

Figure 3. 8. The photocurrent density – voltage ($J-V$) curve of Ag–TiO_2 DSSCs with various weight percent of Ag nanoparticles.

Table 3. 3. The photovoltaic parameters of the Ag–TiO_2 DSSCs with the weight percent of Ag nanoparticles.

Ag wt%	V_{oc} (V)	J_{sc} (mA/cm^2)	ff (%)	η (%)
0	0.76	14.94	0.74	8.42
0.17	0.78	15.36	0.71	8.51
0.35	0.76	15.60	0.72	8.54
0.52	0.77	15.61	0.73	8.78
0.70	0.77	15.86	0.74	9.04
1.05	0.77	15.80	0.72	8.76

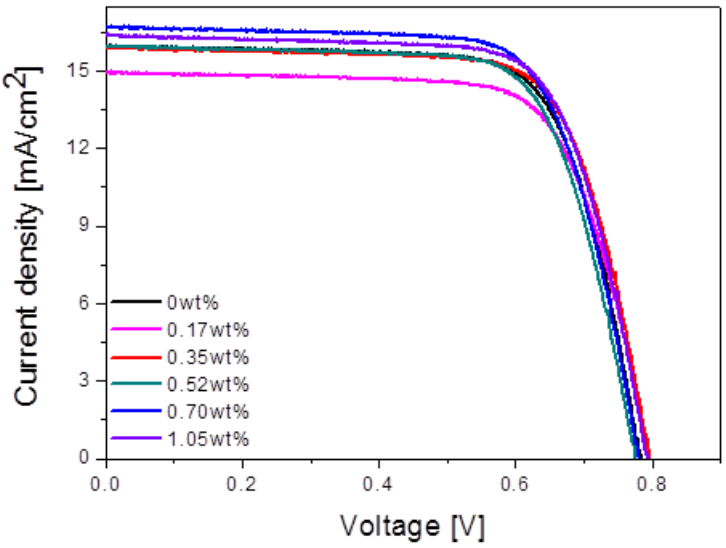

Figure 3. 9. The photocurrent density – voltage ($J-V$) curve of Au–TiO_2 DSSCs with various weight percent of Au nanoparticles.

Table 3. 4. The photovoltaic parameters of the Au–TiO_2 DSSCs with the weight percent of Au nanoparticles.

Au wt%	V_{oc} (V)	J_{sc} (mA/cm²)	ff (%)	η (%)
0	0.76	14.94	0.74	8.42
0.17	0.80	15.89	0.71	9.03
0.35	0.80	15.94	0.72	9.18
0.52	0.78	16.67	0.72	9.36
0.70	0.78	16.39	0.72	9.21
1.05	0.80	15.89	0.71	9.03

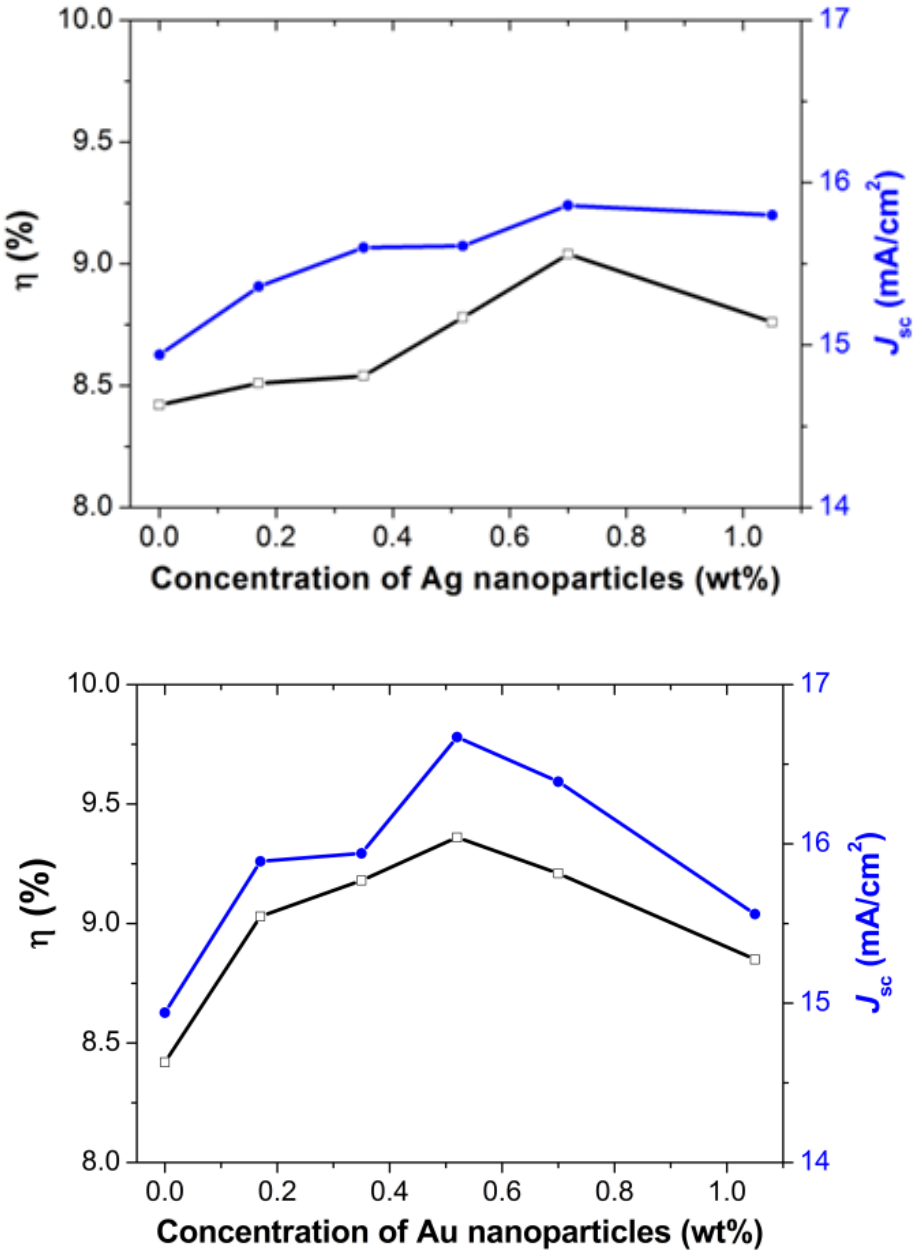

Figure 3. 10. Dependence of metal nanoparticles weight percent on η and J_{sc} values measured from the DSSCs based on Ag−TiO_2 film (top) and Au−TiO_2 film (bottom).

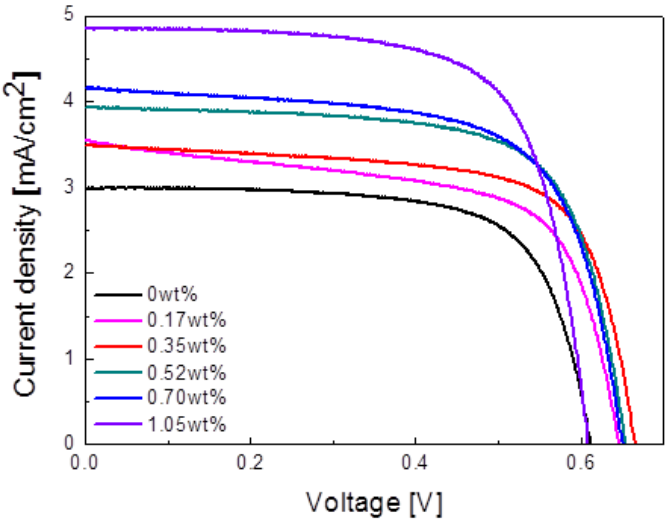

Figure 3. 11. The photocurrent density – voltage ($J-V$) curve of Au–TiO_2 DSSCs based on black dye with various weight percent of Au nanoparticles.

Table 3. 5. The photovoltaic parameters of the Au–TiO_2 DSSCs based on black dye with the weight percent of Au nanoparticles.

Au wt%	V_{oc} (V)	J_{sc} (mA/cm^2)	ff (%)	η(%)
Ref	0.62	2.98	0.7	1.28
0.17	0.65	3.55	0.64	1.46
0.35	0.67	3.49	0.7	1.62
0.52	0.66	3.93	0.7	1.8
0.70	0.65	4.16	0.67	1.81
1.05	0.62	4.86	0.7	2.11

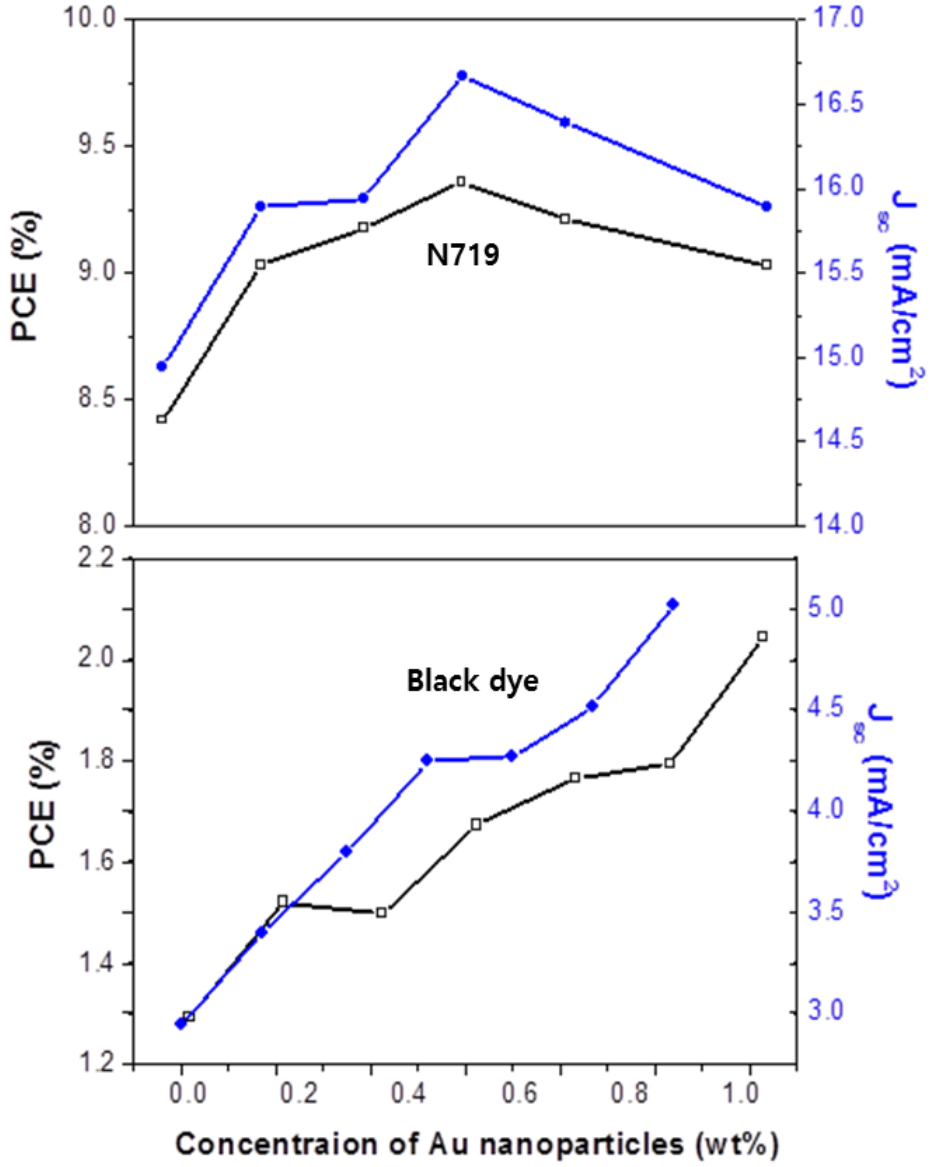

Figure 3. 12. Dependence of Au NPs weight percent on η and J_{sc} values measured from the Au–TiO_2 DSSCs based on N719 dye (top) and black dye (bottom).

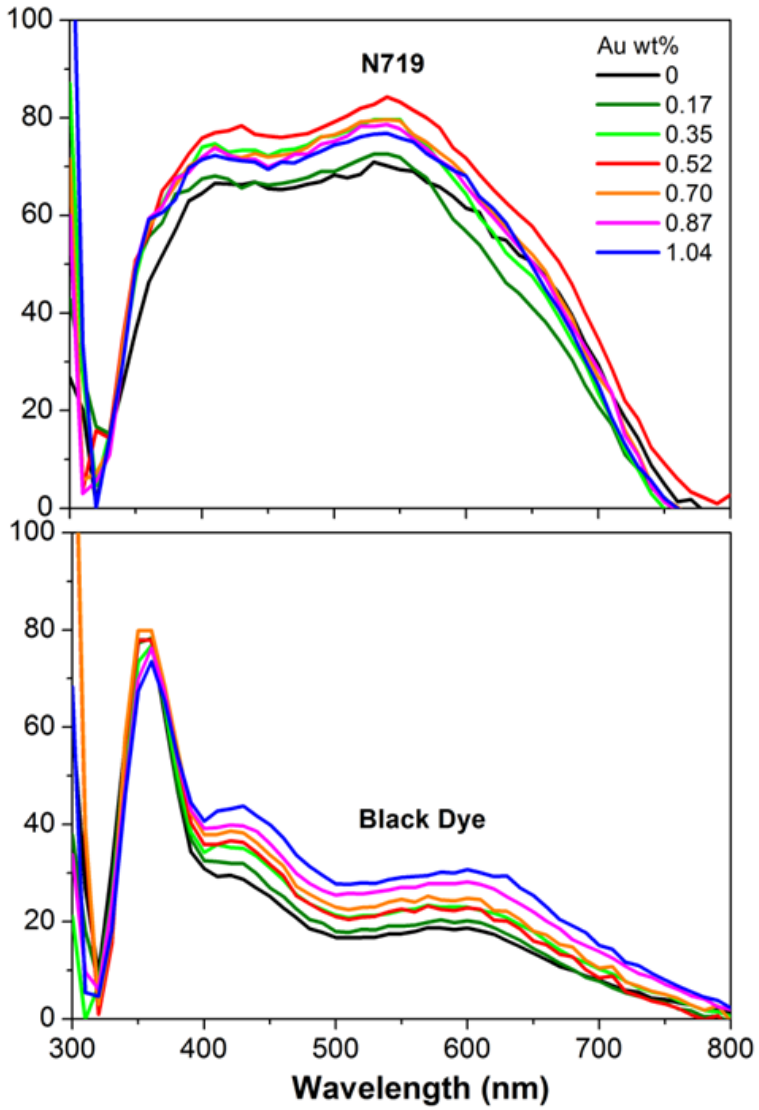

Figure 3. 13. Dependence of Au NPs weight percent on IPCE spectra of Au-TiO_2 NPs DSSCs based N719 dye (top) and black dye (bottom).

3. 4. Conclusion

We have fabricated N719 dye-sensitized solar cells based on double-layered films whose bottom layer consists of TiO_2 and Ag NPs, while the top one consists of TiO_2 and Au NPs. N719 dye, which is the most heavily used dye in DSSCs, has two strong absorption bands centered at 393 and 533 nm. The localized surface plasmon absorption of isolated Au NPs is well matched with the longer wavelength band of N719 dye, while that of isolated Ag NPs with the shorter one. The PCE of the DSSC based on double-layered film was 10.03%, corresponding to 19% enhancement. The enhancement in efficiency of the DSSC may be due to a close optical matching between two visible absorptions of N719 dye and the LSPR effect of Ag and Au NPs. By LSPR effect of Ag and Au NPs, the electric field around the metal NPs enhances and the light absorption cross section of the dye and the number of generated photoelectrons increase which in turn increases the efficiency of DSSCs.

Chapter 4

Preparation of plasmonic monolayer with Ag and Au nanoparticles for dye-sensitized solar cells

4. 1. Overview

We fabricated plasmonic layers with both Au and Ag nanoparticles(NPs) for dye-sensitized solar cells (DSSCs) with the aim of preventing the aggregation of metal NPs and achieving enhanced absorbance of N719 dye, light harvesting efficiency, and power conversion efficiency (PCE).

The plasmonic layer was fabricated by immobilizing plasmonic metal NPs on the surface of the photoactive layer coated with P4VP. The optimal conditions, immobilizing time and order, for metal NPs were examined. With immobilizing each Au or Ag NPs on the surface of the photoactive layer, the PCE improved from 8.82% to 9.53% or 9.33% (8.05% or 5.78% enhancement), respectively. When both Au and Ag NPs were employed together as the plasmonic layer, the PCE further improved from 8.39% to 10.17%, corresponding to 21.16% enhancement. The significant improvement of the PCE could be attributed to the LSPRs of plasmonic layer consisting of Au and Ag NPs. The plasmonic layer, which is located between the photoactive and scattering layers, functions as light scattering site and results in increase optical path length of the incident light, the light absorption and the electron transfer yield.

4. 2. Fabrication of DSSC with a plasmonic layer consisting of Au and Ag nanoparticles

The fabrication scheme of the DSSC with a plasmonic layer consisting of Au and Ag nanoparticles (NPs) is shown in Figure 4.1. The photoanode is composed of a blocking layer, a mesoporous TiO_2 photoactive layer, and a scattering layer. First, the poly(4-vinylpyridine) (P4VP) was coated on TiO_2 film, as shown in Figure 4.1(a). Then, Au NPs were immobilized on the surface of TiO_2 film by immersing the TiO_2 film in an Au colloid solution, as shown in Figure 4.1(b). Afterwards, Ag NPs were immobilized on the surface of TiO_2 film that was already coated with Au NPs by P4VP, by immersing in an Ag colloid solution, as shown in Figure 4.1(c). After immobilizing the Au and Ag NPs on the surface of TiO_2 film as the plasmonic layer, P4VP was removed by an annealing process. A TiO_2 scattering pastes (DSL 18NR-AO, Dyesol) were doctor-bladed on the TiO_2 film immobilized Ag and Au NPs, and annealed gradually at 450 ℃ for 30min. The photoanode were treated in titanium isopropoxide (TIP)solutions (0.1 M in isopropyl alcohol) at 90 ℃ for approximately 30 min, and followed by annealing at 450 ℃ for 30 min. The TiO_2 NPs or metal-TiO_2 NPs film were immersed into a N719 (Solaronix) dye ethanolic solution at 50 ℃ for overnight. Finally, the DSSC was subsequently fabricated by assembling the photoanode and the Pt counter electrode and injecting the electrolyte, as shown in Figure 4.1(d).

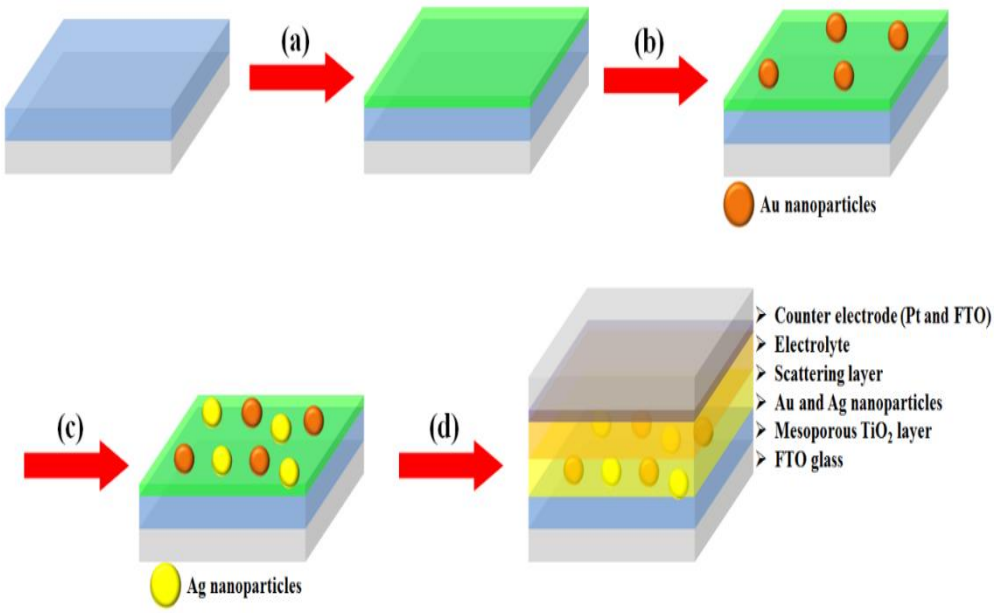

Figure 4. 1. Fabrication of the DSSC using plasmonic layer with Au and Ag nanoparticles: (a) coating of P4VP, (b) immobilization of Au nanoparticles, (c) immobilization of Ag nanoparticles, and (d) assembly of the DSSC.

4. 3. Result and discussion

4. 3. 1. Characterization of plasmonic layer with Au and Ag NPs

The Au and Ag NPs were used to fabricate plasmonic layer. The plasmonic layer was prepared by immobilizing metal NPs on the surface of the TiO_2 film via P4VP.[136] Firstly, Au NPs were immobilized on the surface of the TiO_2 film coated with P4VP. Figure 4.2 shows the SEM images of immobilized Au NPs on the cover glasses by increasing immobilizing time, from 30 min to 240 min. It should be commented that when metal NPs were immobilized on the TiO_2 film, it is difficult to distinguish immobilized metal NPs from TiO_2 NPs. Therefore, to identify their immobilized state on the surface by SEM images, metal NPs were immobilized on the cover glass. We suggested that the immobilized state of metal NPs on the cover glass is almost same as that of metal NPs on TiO_2 film.

When the films were immersed in Au colloid solution for 30min, Au NPs immobilized without aggregation on the surface. As increased immobilizing time, the amount of immobilized Au NPs on the surface increased and aggregated. Figure 4.3 shows the UV-visible extinction spectra of immobilized Au NPs on the cover glasses by increasing immobilizing time. The maximum absorption wavelength (λ_{max}) of the film coated with Au NPs was *ca* 530 nm. After further immobilizing Au NPs, λ_{max} of the film with Au NPs was

red-shifted and it included the shoulder near 600nm. When metal NPs aggregate, the conduction electrons near the surface of metal NPs become delocalized and shared with neighboring NPs. It results in the extinction peak to red-shift to longer wavelengths. When Au NPs were immobilized for 240 min, the intensity of extinction peak decreased due to the depletion of stable NPs. As the particles destabilize, the intensity of the extinction peak will decrease.

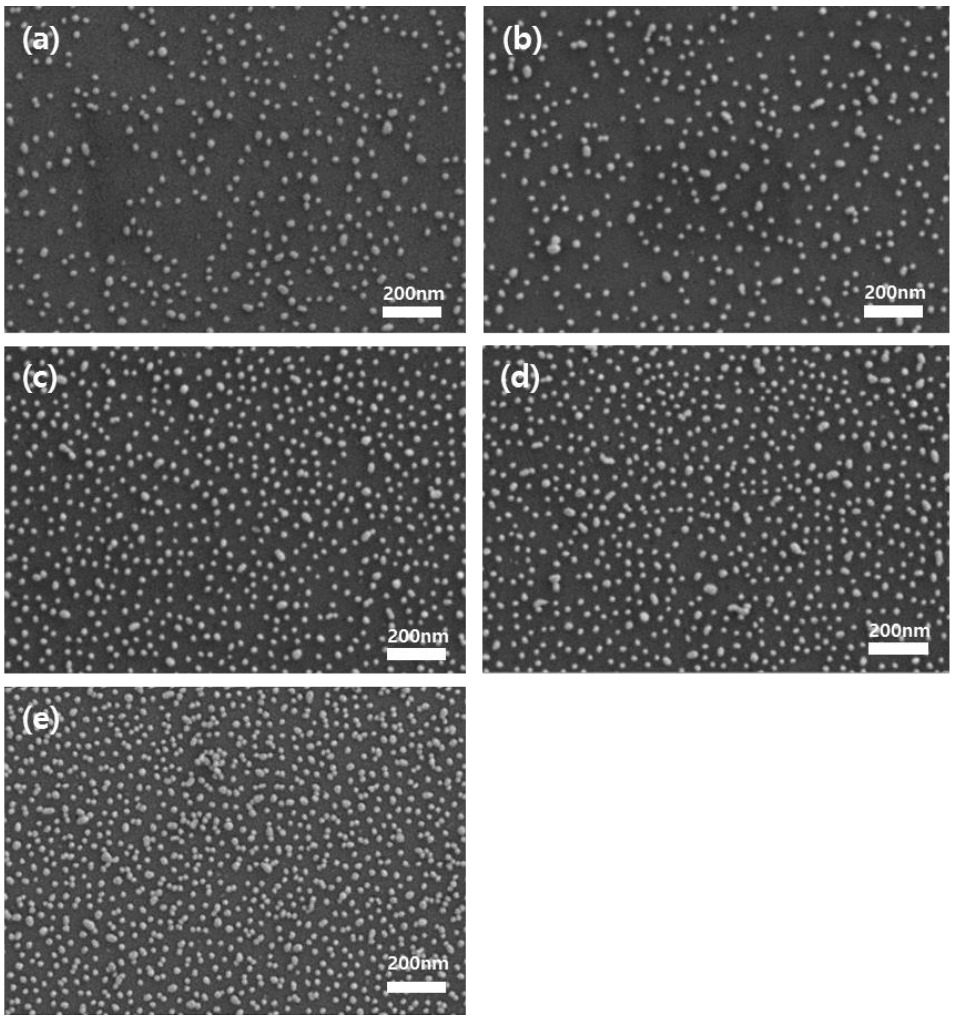

Figure 4. 2. The SEM images of immobilized Au nanoparticles on the cover glasses with P4VP for (a)30 min, (b)70 min, (c)120 min, (d)180 min, (e)240 min.

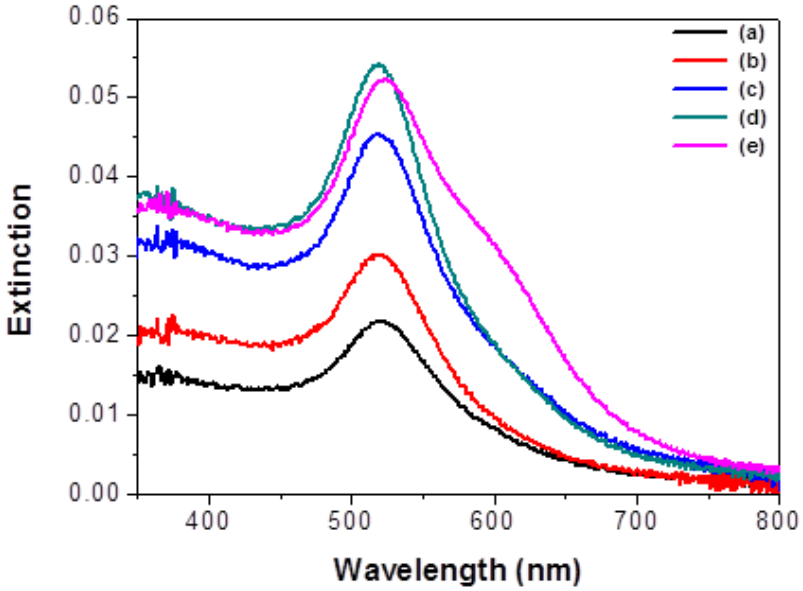

Figure 4. 3. The UV−visible extinction spectra of Au nanoparticles immobilized on the cover glasses for (a)30 min, (b)70 min, (c)120 min, (d)180 min, (e)240 min.

Afterward, Ag NPs were immobilized on the plasmonic TiO_2 film that was already immobilized Au NPs. Figure 4.4 shows the SEM images of immobilized Ag NPs on the cover glasses coated Au NPs, by increasing immobilizing time from 0 min to 25 min. As increased Ag NPs immobilizing time, the amount of immobilized Ag NPs on the surface increased and aggregated with metal NPs. Figure 4.5 shows the UV-visible extinction spectra of plasmonic layer with Au and Ag NPs by various immobilizing time of Ag NPs. The maximum absorption wavelength (λ_{max}) of the film with Au NPs was *ca* 530 nm. When Ag NPs were immobilized on the film coated Au NPs, the UV-visible extinction spectra of plasmonic layer with Au and Ag NPs exhibited a red-shifted peak for Au NPs at 554 nm and another peak for Ag NPs at 436 nm. As increased immobilizing time of Ag NPs, the λ_{max} of both Au and Ag NPs become red-shifted and absorption range was broadened due to aggregation. The resulting broad absorption range well covered that of the N719 dye. When Ag NPs were immobilized over 15min, the intensity of extinction spectra decreased due to unstable metal NPs.

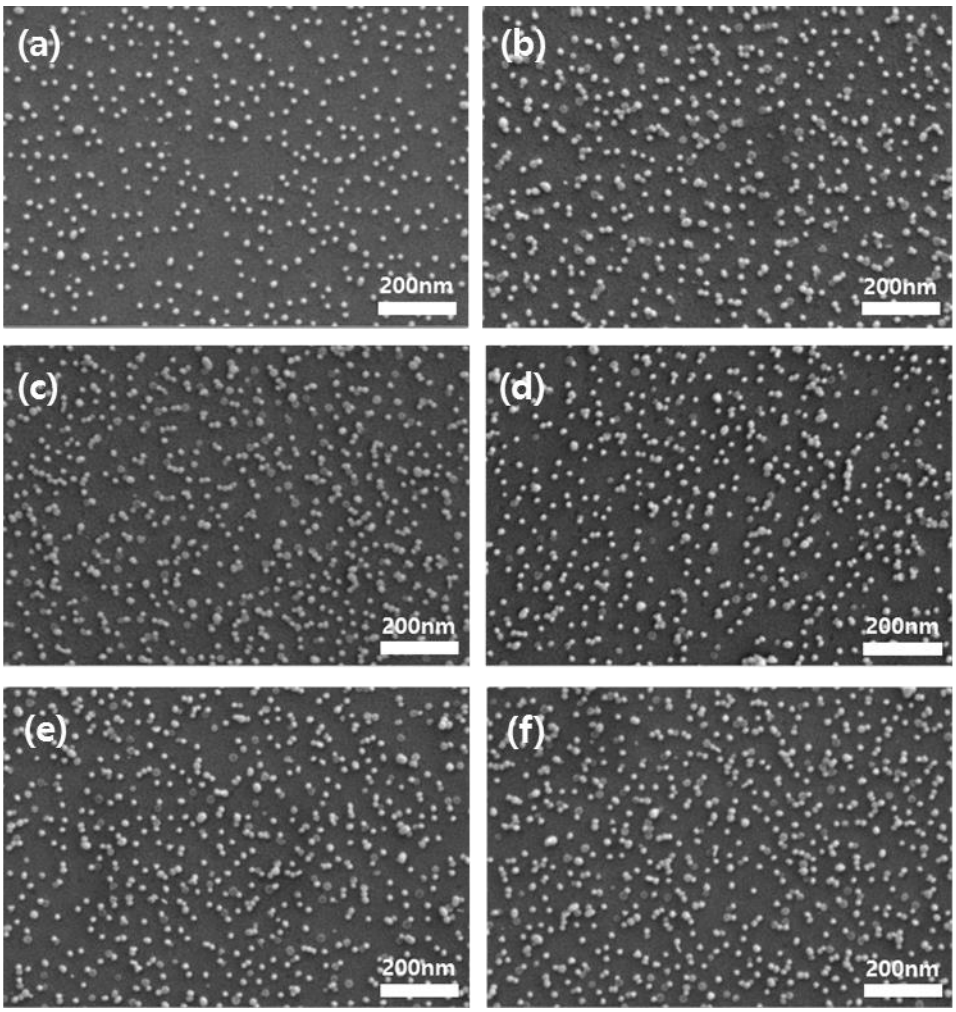

Figure 4. 4. The SEM images of immobilized Ag nanoparticles on the cover glasses, which are already immobilized Au nanoparticles for 70min, for (a)0 min, (b)5 min, (c)15 min, (d)20 min, (e)25 min

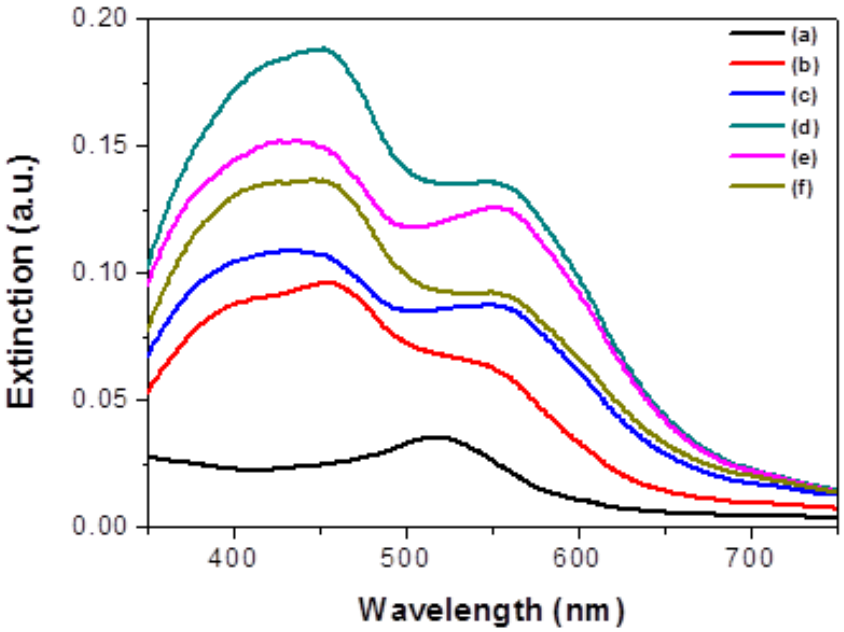

Figure 4. 5. The UV-visible extinction spectra of plasmonic layer with Au and Ag nanoparticles with various Ag nanoparticles immobilizing time (a)0 min, (b)5 min, (c)10 min, (d)15 min, (e)20 min, (f)25min. The Au NPs were immobilized on the cover glasses for 70min.

4. 3. 2. Optimization of plasmonic layer with Au and Ag NPs for DSSCs

4. 3. 2. 1. Optimization depends on immobilizing time of metal nanoparticles for DSSCs

The performance of DSSCs can depend on the type of metal NPs[40, 137] and their immobilizing time.[122] Therefore, we first studied the optimal immobilization conditions for the Au and Ag NPs.

To identify the optimal immobilizing time for the Au NPs, the DSSCs incorporated a plasmonic layer consisting of only Au NPs were fabricated with different immobilizing time of Au NPs. Figure 4.6 shows the photocurrent density – voltage ($J-V$) curves of them. Their photovoltaic parameters, the short-circuit current density (J_{sc}), open-circuit voltage (V_{oc}), fill factor (ff), and power conversion efficiency (PCE), are summarized in Table 4.1. As increased the immobilizing time up to 70 min, the PCE gradually increased from 8.82% up to 9.53%, and then decreased to 9.19% when the immobilizing time was further extended to 120 min. A similar tendency was observed in the J_{sc} value, which increased from 16.58 mA/cm^2 to 17.66 mA/cm^2 and then decreased to 17.03 mA/cm^2, respectively. All of the DSSCs with immobilizing Au NPs for 30-120 min improved J_{sc} and PCE. Under the immobilizing for 70 min, J_{sc} and the PCE of the DSSC were enhanced by 6.51% and 8.05%, compared to those of the DSSC without Au NPs, respectively.

Figure 4.7 shows the $J-V$ curves of DSSCs incorporated a plasmonic layer consisting of only Ag NPs with various immobilizing times, and the photovoltaic parameters of them are listed in Table 4.2. As increased the immobilizing time up to 10 min, the J_{sc} and PCE values of the DSSC increased from 16.58 mA/cm^2 to 17.09 mA/cm^2 and from 8.82% to 9.33%, representing 7.28% and 5.78% enhancement, respectively.

The dependence of J_{sc} and PCE on the immobilizing time for DSSCs incorporated a plasmonic layer of Au or Ag NPs is schematized in Figure 4.8. For both DSSCs, the tendency in change of J_{sc} and PCE is same that is increased up to certain optimal value and then decreased over that value. With increasing immobilizing time of metal NPs, the probability of aggregation between metal NPs would be increased, and localized surface plasmon resonance (LSPR) peaks of metal NPs are red-shifted. Therefore, by increasing immobilizing time further optimal values, J_{sc} and PCE of the DSSCs decrease due to a decrease in the spectral overlap between the LSPR absorption of metal NPs and dye absorption.

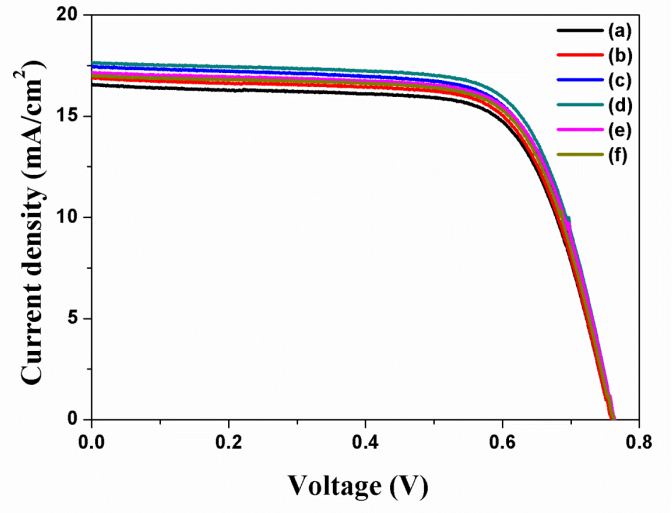

Figure 4. 6. $J-V$ curves of DSSCs with Au nanoparticles by immobilization times. (a) 0 min (no dipping), (b) 30 min, (c) 50 min, (d) 70 min, (e) 100 min, and (f) 120 min.

Table 4. 1. Photovoltaic parameters of DSSCs with Au nanoparticles by immobilization time.

DSSCs with Au nanoparticles by immobilization time	J_{sc} (mA/cm^2)	V_{oc} (V)	ff	η (%)
0 min	16.58	0.76	0.70	8.82
30 min	16.92	0.76	0.70	9.00
50 min	17.44	0.76	0.70	9.28
70 min	17.66	0.76	0.71	9.53
100 min	17.16	0.76	0.71	9.26
120 min	17.03	0.76	0.71	9.19

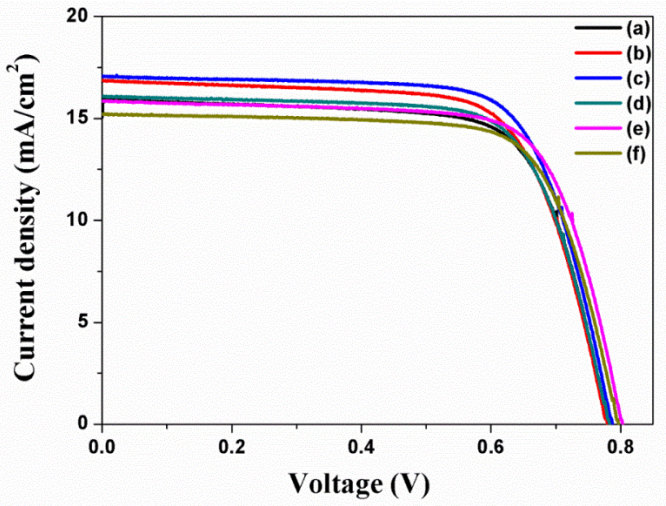

Figure 4. 7. $J-V$ curves of DSSCs with Ag nanoparticles by immobilization times. (a) 0 min (no dipping), (b) 5 min, (c) 10 min, (d) 15 min, (e) 20 min, and (f) 25 min.

Table 4. 2. Photovoltaic parameters of DSSCs with Ag nanoparticles by immobilization time.

DSSCs with Ag nanoparticles by immobilization time	J_{sc} (mA/cm^2)	V_{oc} (V)	ff	η (%)
0 min	15.93	0.78	0.71	8.82
5 min	16.87	0.78	0.70	9.21
10 min	17.09	0.78	0.70	9.33
15 min	16.08	0.79	0.71	9.02
20 min	15.85	0.78	0.71	8.78
25 min	15.23	0.80	0.72	8.77

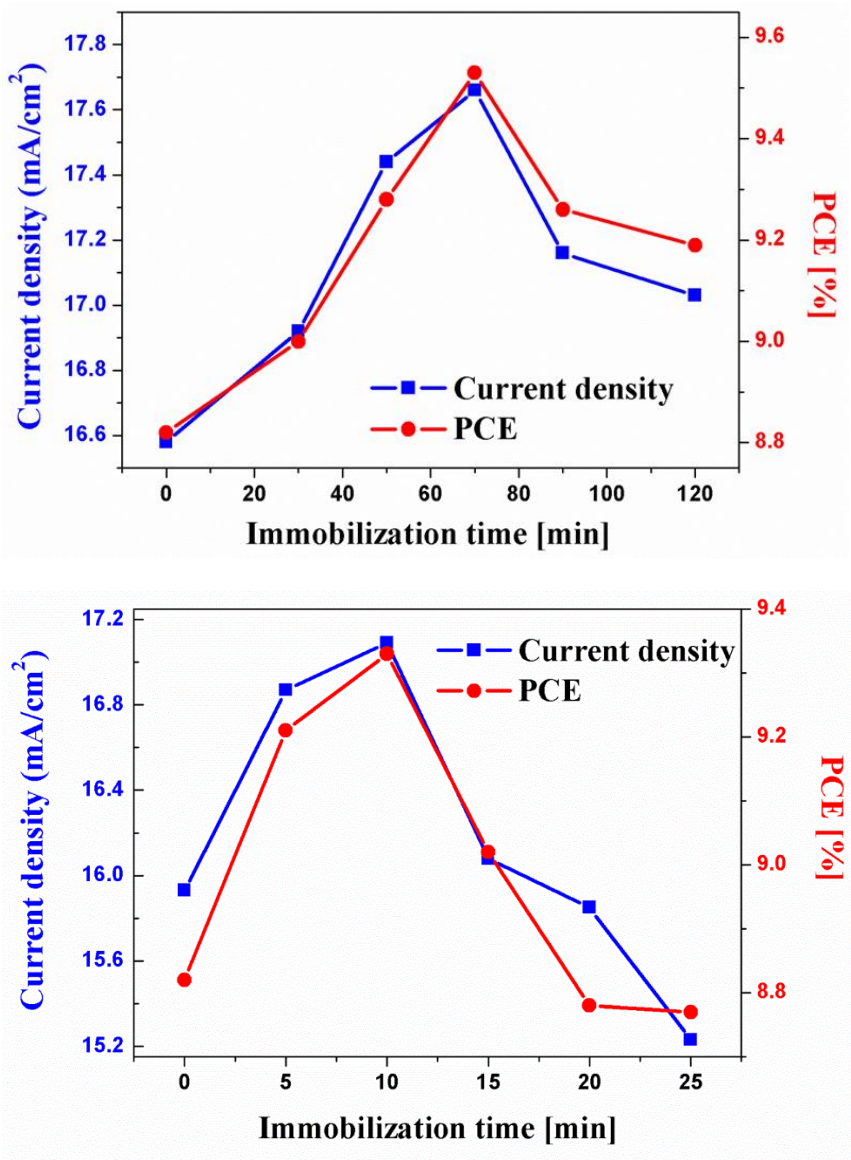

Figure 4. 8. Dependence of J_{sc} (blue) and PCE (red) on immobilization time, for DSSCs using a plasmonic layer of Au nanoparticles (top) or Ag nanoparticles (bottom).

4. 3. 2. 2. Optimization depends on immobilizing order of metal nanoparticles for DSSCs

When the DSSCs incorporated a plasmonic layer with metal NPs are fabricated, the immobilizing order on the surface of the TiO_2 film affect on the efficiency of the DSSCs. To identify the optimum immobilizing order, we fabricated serieses of the DSSCs incorporated plasmonic layer with different immobilizing order and time. One series was composed of the DSSCs firstly immobilized Au NPs (70min) and then Ag NPs (5, 10, 15, 20 min). Another series was composed of the DSSCs firstly immobilized Ag NPs (10min) and then Au NPs (30, 50, 70, 100min). The metal NPs, which were firstly immobilized, were immobilized for optimum immobilizing time. Figure 4.9 shows the UV-visible extinction spectra of immobilized metal NPs with different immobilizing order and time. The photovoltaic parameters of DSSCs incorporated a plasmonic layer with metal NPs are summarized in Table 4.3. As shown in Table 4.3, DSSCs firstly immobilized Au and then Ag NPs have higher PCE than firstly immobilized Ag and then Au NPs. In the DSSCs with immobilizing Ag and Au NPs, the J_{sc} and the PCE increased with increasing immobilizing time of Au NPs which were immobilized afterward. While in the DSSC with immobilizing Au and Ag NPs, the J_{sc} and the PCE increased up to optimum immobilizing time of Ag NPs and then decreased further immobilizing time of Ag NPs.

To demonstrate this phenomena, the UV-visible extinction spectra of plasmonic layer immobilized firstly Au NPs(70min) and

then Ag NPs(10min), plasmonic layer immobilized firstly Ag NPs(10min) and then Au NPs(70min) and the UV-visible absorption spectra of N719 dye were compared as shown in Figure 4.10. The maximum absorption wavelength (λ_{max}) and the full width half maxium (FWHM) of N719 dye were 400 nm and 99nm in higher energy absorption band, and 531 nm and 109nm in lower energy absorption band. The λ_{max} and FWHM of plasmonic layer immobilized firstly Au NPs and then Ag NPs were 398 nm and 122 nm in higher energy absorption band, and 413 nm and 112 nm in lower energy absorption band. The λ_{max} and FWHM of plasmonic layer immobilized firstly Ag NPs and then Au NPs were 413 nm and 112 nm in higher energy absorption band, and 524 nm and 168 nm in lower energy absorption band. Therefore, the λ_{max} and FWHM of N719 dye well matched and overlapped with those of plasmonic layer immobilized firstly Au NPs and then Ag NPs than upside down immobilizing order.

It was reported that Ag NPs are faster adsorption on P4VP film than Au NPs by 2times.[138] The adsorption strength of Ag NPs with immobilized the pyridine N atoms on the surface is more greater than that of Au NPs. Based on this, the J_{sc} and the PCE of DSSCs immobilized firstly Ag NPs and then Au NPs continuosely increased by increasing immobilizing time of Au NPs because immobilization of Au NPs are distruppted by Ag NPs immobilized on TiO_2 film which results in further take immobilizing time of Au NPs. Therfore, it is optimal condition that Au NPs, which have slower adsorption and lower adsortpion strength than Ag NPs, are firstly immobilized.

Consequently, the DSSC incorporated plasmonic layer immobilized firstly Au NPs (70 min) and then Ag NPs (10 min) has the highest efficiency, 9.74%, corresponding to 24 % enhancement compared to the DSSC without plasmonic layer.

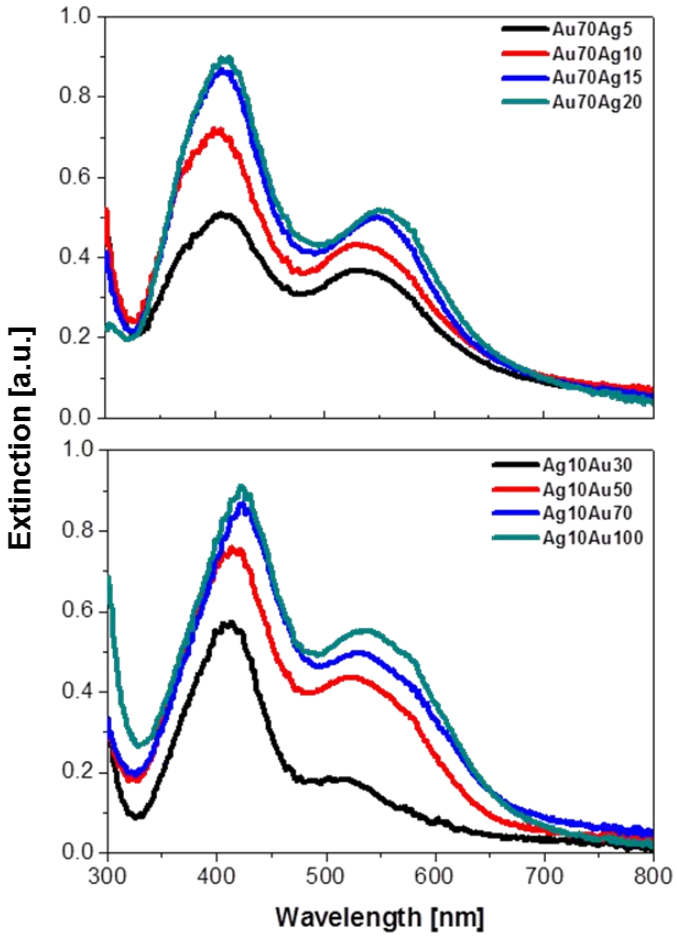

Figure 4. 9. The UV-visible extinction spectra of immobilized metal nanoparticles with different immobilizing order and time

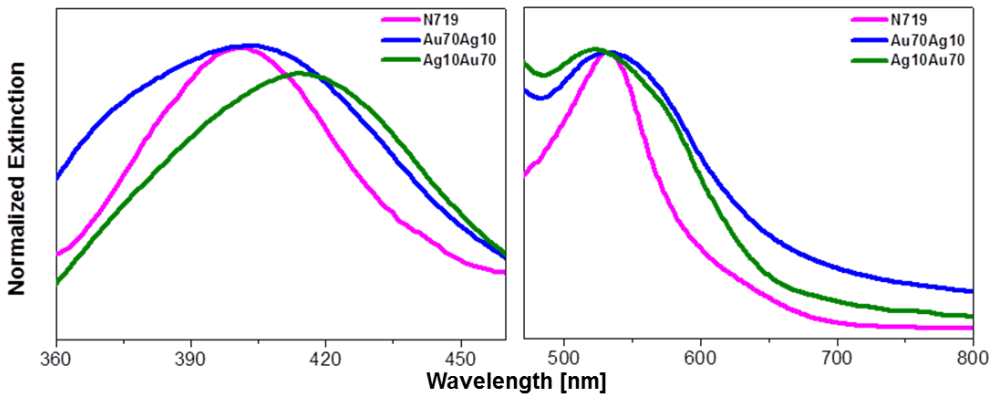

Figure 4. 10. Comparison to the UV-visible extinction spectra of plasmonic layer with immobilized Au(70min) and Ag(10min) (blue) and plasmonic layer with immobilized Ag (10min) and Au (70min) (green), and the UV-visible absorption spectra of high energy absorption band of N719 dye (left) and low energy absorption band of N719 dye (right).

Table 4. 3. Photovoltaic parameters of DSSCs with Au and Ag nanoparticles by different immobilizing order.

	J_{sc} (mA/cm^2)	V_{oc} (V)	ff (%)	η (%)
Ref	14.82	0.78	0.68	7.86
Ag10Au30	15.34	0.78	0.70	8.38
Ag10Au50	16.25	0.80	0.68	8.84
Ag10Au70	16.02	0.79	0.70	8.86
Ag10Au100	16.68	0.80	0.69	9.21
Au70Ag5	16.89	0.80	0.69	9.32
Au70Ag10	17.39	0.80	0.70	9.74
Au70Ag15	16.59	0.79	0.69	9.04
Au70Ag20	15.74	0.80	0.69	8.69

4. 3. 3. Photovoltaic properties of DSSCs based on plasmonic layer with Au and Ag NPs

Based on optimal immobilized condition, we fabricated DSSC incorporated plasmonic layer. Firstly, Au NPs immobilized on the surface of the TiO_2 film coated with P4VP for 70min, and then Ag NPs immobilized on the surface of the TiO_2 film coated with Au NPs for10min. Figure 4.11(a) shows the SEM image of the surface immobilized Au NPs on the TiO_2 film via P4VP for 70min. Then, the SEM image of the Ag NPs immobilized on the surface of the same film for 10min is shown in Figure 4.11(b).

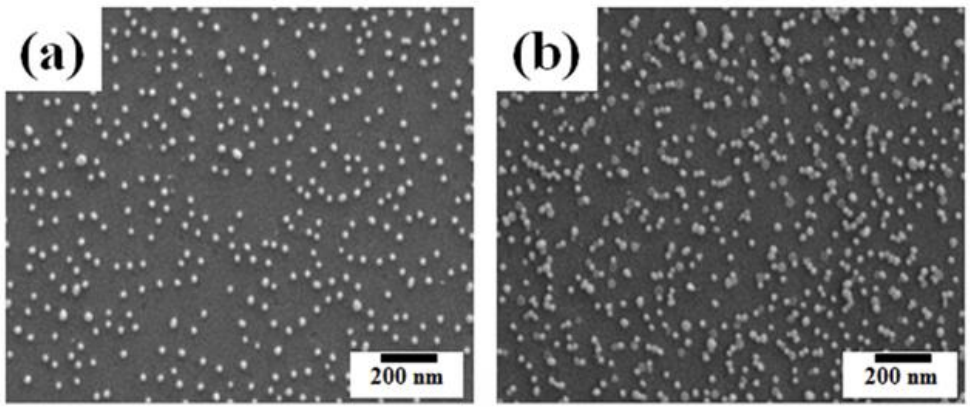

Figure 4. 11. SEM images of the surface immobilized (a) the Au nanoparticles, (b) the Au and Ag nanoparticles on the TiO_2 film.

The $J-V$ curves are shown in Figure 4.12, and the photovoltaic parameters are summarized in Table 4.4. Between the DSSCs without plasmonic layer and with plasmonic layer consisting of Au

and Ag NPs, the values of J_{sc}, V_{oc}, *ff*, and PCE increased from 15.83 mA/cm^2 to 17.88 mA/cm^2, 0.78 V to 0.81 V, 0.68 to 0.70, and 8.39% to 10.17%, respectively. In the presence of the plasmonic layer, more electrons are generated from the dye by the plasmonic effect which results in increasing the electron density of the mesoporous TiO_2 layer with Au and Ag NPs. The Fermi level shifts more negative in potential as reflected by the increased V_{oc} and *ff*.[139, 140] And the plasmonic layer, which is located between the photoactive and scattering layers, functions as light scattering site and results in increase optical path length of the incident light and light absorption. As a result, the DSSC incorporated plasmonic layer with Au and Ag NPs exhibited the highest PCE value, 10.17%, corresponding to 21.16% enhancement compared to that based on the plasmonic layer without metal NPs.

Figure 4.13 shows the incident photon to electron conversion efficiency (IPCE) spectra of the DSSCs. The intensity of IPCE over the wavelength range 350 nm to 700 nm increased by immobilizing Au and Ag NPs. It seems to be related to the overlap between the absorption bands of N719 dye and that of Au and Ag NPs. In the DSSC incorporated plasmonic layer consisting of Au and Ag NPs, the enhancement of intensity over 530 nm to 550 nm was induced by Au NPs and that of the intensity over 380 nm to 400nm was induced by Ag NPs. In conclusion, the DSSC incorporated plasmonic layer consisting of Au and Ag NPs shows higher intensity of IPCE than that of the DSSC without metal NPs.

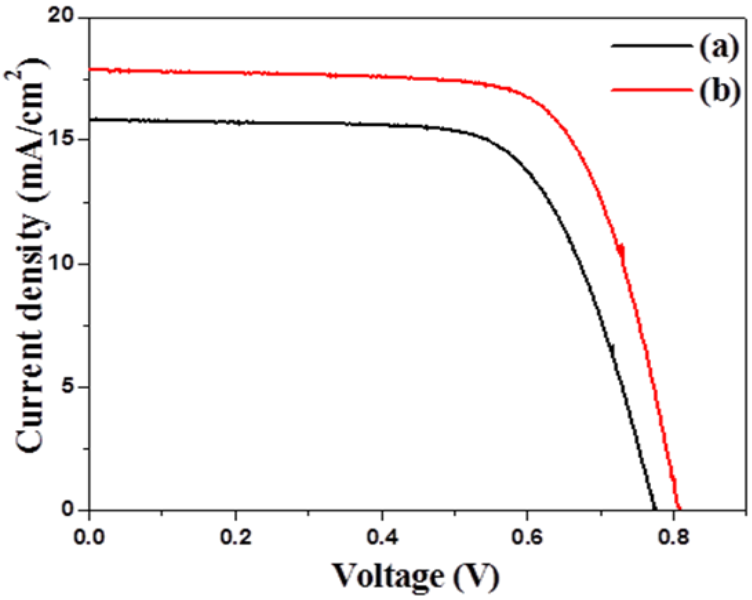

Figure 4. 12. J−V curves of DSSCs (a) without plasmonic layer and (b) with Au and Ag nanoparticles immobilized for 70 min and 10 min, respectively.

Table 4. 4. Photovoltaic properties of DSSCs with Ag and Au nanoparticles by immobilization time.

DSSCs with Au and Ag nanoparticles for	J_{sc} (mA/cm^2)	V_{oc} (V)	ff (%)	η (%)
0 min	15.83	0.78	0.68	8.39
70 min and 10min	17.88	0.81	0.70	10.17

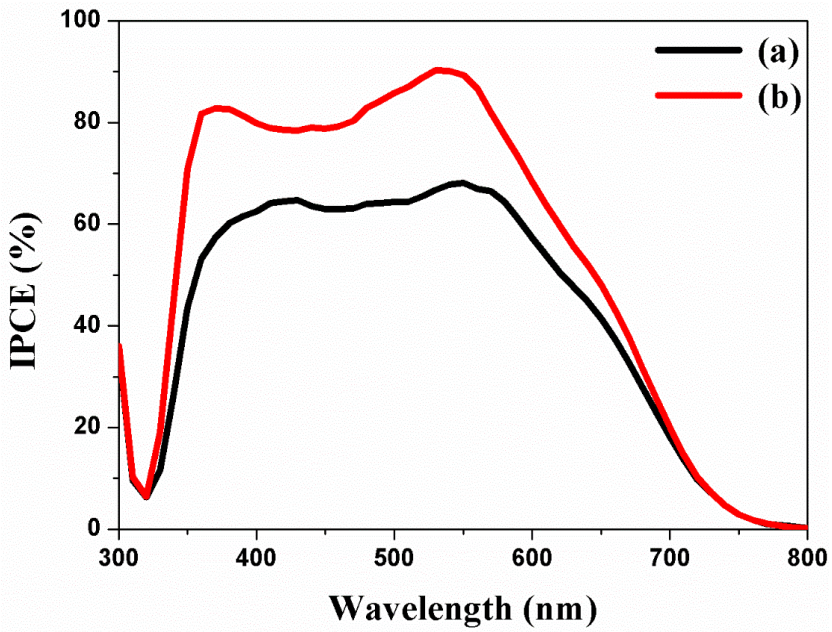

Figure 4. 13. IPCE spectra of the DSSCs (a) without plasmonic layer and (b) with Au and Ag nanoparticles immobilized for 70 min and 10 min, respectively.

4. 3. 4. Plasmonic effect in DSSCs based on plasmonic layer with Au and Ag NPs

To prove the plasmonic effect of Au and Ag NPs in DSSCs incorporated plasmonic layer, the UV-visible absorption spectra of TiO_2 film and plasmonic TiO_2 films without dye adsortpion, with N719 dye adsorption and the desorbed N719 dye in NaOH solution from dye-adsorbed TiO_2 film and plasmonic TiO_2 film were measured as shown in Figure 4.14. Figure 4.14(a) shows the absorption spectra of the plasmonic TiO_2 films without dye adsorption with different immobilizing time of metal NPs. It is observed increase LSPR peak of Au and Ag NPs in TiO_2 film with increasing immobilizing time of metal NPs. Figure 4.14(b) shows the absorption spectra of the plasmonic TiO_2 films with N719 dye adsorption with different immobilizing time of metal NPs. The enhanced absorption spectra exhibited at near 400nm and 530nm due to the LSPR of Au and Ag NPs. The more immobilizing time of metal NPs increased, the higher intensity of absorption spectra increased. The improved absorption spectra were attributed to the plasmonic effect of Au and Ag NPs. To confirm this argument, the absorption spectra of the desorbed N719 dye in NaOH solution from dye-adsorbed TiO_2 film and plasmonic TiO_2 film were measured. The intensity of the absorption peak in the desorbed N719 dye solution from plasmonic TiO_2 film slightly decreased with increasing immobilizing time of metal NPs, compared to only TiO_2 film. It can be evidenced that the amount of adsorbed N719 dye in

plasmonic TiO_2 film is less than that of only TiO_2 film. Based on these results in Figure 4.14, the enhancement of the absorption is not due to increase in the amount of dye but the plasmonic effect of Au and Ag NPs.

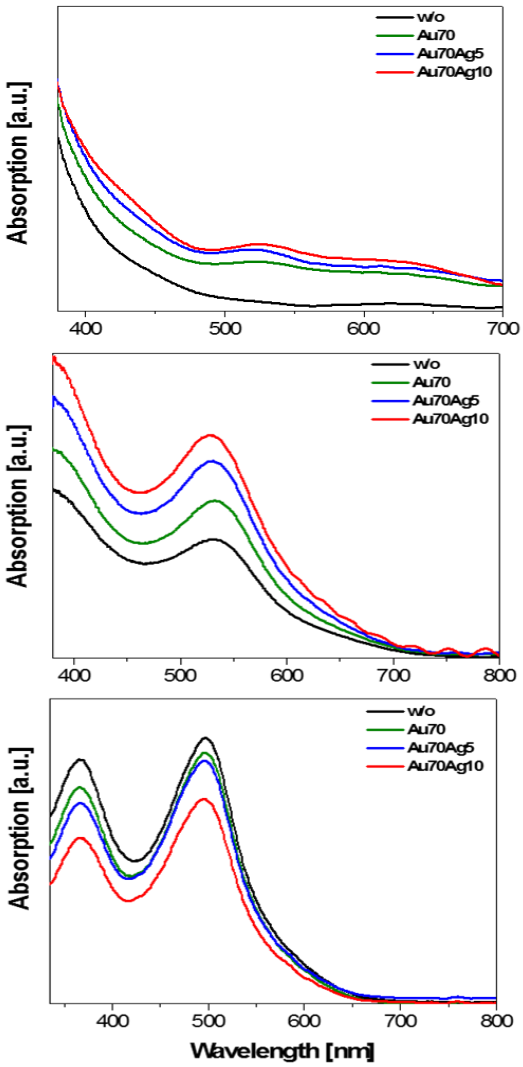

Figure 4. 14. Absorption spectra of (a) photoanodes with different immobilizing time of metal nanoparticles, (b) photoanodes with different immobilizing time of metal nanoparticles with adsorbed dyes. (c) the desorbed N719 in NaOH solution from dye-loaded TiO_2 film.

Also, to prove the plasmonic effect of Au and Ag NPs in DSSCs incorporated plasmonic layer, the photovoltaic properties of the DSSCs based on only TiO_2 film and the DSSCs based on plasmonic layer with Au and Ag NPs by different thickness of TiO_2 film were compared, as shown in Table 4.5. Generally, the light absorption of the photoanode in DSSC is affected by amount of adsorbed dye molecules on the TiO_2 film, up to optimal photoanode thickness. As the thickness of photoanode is thicker, the recombination current is larger which results in reduce the loss of the electrons during transportation in photoanode. In the DSSCs based on only TiO_2 film, the J_{sc} and the PCE of DSSCs increased with thicker TiO_2 film due to increase the amount of adsorption dye on the TiO_2 film. The DSSC with 9 μm TiO_2 film has the highest efficiency, 8.05 %, compared to that of 3 μm and 4.5 μm TiO_2 film, 7.79% and 7.70%. While, the DSSC with 4.5 μm TiO_2 film has the highest efficiency, 9.65 %, in the DSSCs based on plasmonic layer with Au and Ag NPs. The thicker TiO_2 film is not exactly a good thing in DSSCs with plasmonic layer due to reduction in amount of the light, which is reached at the metal NPs in TiO_2 film. By incorporating plasmonic layer on the TiO_2 film, the efficiency of the DSSC increased and the thickness of the photoanode in DSSC decreased than that of the DSSCs without plasmonic layer.

Table 4. 5. The photovoltaic parameters of the conventional DSSCs (only TiO_2 film) and the DSSCs based on plasmonic layer with Au and Ag NPs by different thickness of TiO_2 film

Active+Scatter (μm)	J_{sc} (mA/cm²)	V_{oc} (V)	FF (%)	η (%)
Ref-3 + 8.5	14.90	0.75	0.7	7.79
Ref-4.5 + 8.5	15.31	0.74	0.68	7.70
Ref-9 + 8.5	15.89	0.74	0.68	8.05
AuAg-3 + 8.5	16.12	0.77	0.71	8.78
AuAg-4.5 + 8.5	17.91	0.77	0.7	9.65
AuAg-9 + 8.5	16.54	0.77	0.7	8.92

4. 4. Conclusion

To improve the efficiecny of the DSSCs, a plasmonic layer consisting of Au and Ag NPs was prepared by dipping P4VP-coated mesoporous TiO_2 layer in the colloid solutions. Separate experiments with Au and Ag NPs showed the optimal immobilization times of 70 min for Au and 10 min for Ag, which resulted in 8.05% (from 8.82% to 9.53%) and 5.78% (from 8.82% to 9.33%) enhancement of the PCE, respectively. When Au and Ag NPs were used together in the plasmonic layer, the PCE further improved to 10.17%, corresponding to 21.16% enhancement, due to the increased values of J_{sc}, V_{oc}, and *ff*. The highest efficiency of DSSCs is due to LSPRs of a plasmonic layer consisting of Au and Ag NPs. The plasmonic layer located between the photoactive and scattering layers functions as light scattering site. It enhanced optical path length of the incident light thereby increasing the light absorption and the electron transfer from metal NPs to electrode.

Chapter 5

Multi-shaped Ag nanoparticles in a plasmonic layer in dye-sensitized solar cells for increased power conversion efficiency

5. 1. Overview

We have prepared Ag NPs by one-step seed-mediated process with different amount of Ag seed solution. As increased amount of Ag seed solution, the shape of Ag NPs changes from sphere to discal plate with increasing their size, and the maximum absotprion wavelength (λ_{max}) of them was red-shifted, from 400 nm to 550 nm. The DSSC incorporated Ag NPs whose have broad absorption with λ_{max} near 420nm and various shapes such as sphere, rod, triangular plate (so called multi-shaped Ag nanoparticles) has the highest PCE due to broad absorption covered with higher energy band of the N719 dye at 393 nm (λ_1). When the Ag NPs, which have λ_{max} over 500 nm and discal plate, are incorporated in DSSCs, the PCE of DSSCs decreased due to decrease in matching with λ_1 of the N719 dye.

We have compared the effect of spherical Ag NPs and multi-shaped Ag NPs on the photovoltaic properties of DSSCs based on layer-by-layer structure with Ag and Au NPs. The λ_{max} of spherical Ag and multi-shaped Ag NPs are near absorption band of the N719 dye at 393 nm (λ_1), while the λ_{max} of Au NPs is near absorption band of the N719 dye at 533 nm (λ_2). The λ_{max} of the multi-shaped Ag NPs is 420 nm, including the shoulder with a full width at half maximum (FWHM) of 121 nm. This is a broad absorbance wavelength compared to spherical Ag NPs, whose λ_{max} is 400 nm, without the shoulder of 61 nm FWHM. Therefore, when multi-shaped Ag NPs were incorporated in DSSCs based on a layer-by-

layer structure, the PCE increased from 8.44% to 10.22%, a 21.09% enhancement compared to DSSCs without metal NPs. Moreover, we also confirmed the plasmon-enhanced effect in DSSCs based on the composite film structure, the PCE of DSSCs based on the composite film structure with multi-shaped Ag NPs increased from 8.48% to 10.34%, a 21.93% enhancement, compared to DSSCs without metal NPs.

5. 2. Fabrication of Ag nanoparticles by one-step seed-mediated process

Ag NPs were prepared by a one-step seed-mediated process. To prepare the Ag seed solution, 0.30 mL silver nitrate ($AgNO_3$, 10 mM) and trisodium citrate (1 mM) solutions were mixed by stirring for 5 min. Subsequently, 1.8 mL sodium borohydride ($NaBH_4$, 10 mM) was injected into the mixed solution and stirred for 5 min. To grow Ag seeds to Ag NPs, 4, 6, 10, 12 or 16 mL of the Ag seed solution and 16, 14, 10, 8 or 4 mL trisodium citrate solution mixed respectively to make total 20mL of solution. And then, 0.2 mL ascorbic acid (20 mM) solution and 0.8 mL $AgNO_3$ solution were injected into this mixture solution. The mixture was stirred for 30 min.

5. 3. Fabrication of DSSCs based on layer by layer structure with multi-shaped Ag and Au nanoparticles.

We fabricated the DSSCs based on a layer-by-layer structure with multi-shaped Ag and Au NPs by poly (4-vinylpyridine) (P4VP) (Figure 5.1).[136] First, the TiO_2 blocking layer was coated on the fluorine-doped tin oxide (FTO) glass (Figure 5.1(a)). The mesoporous TiO_2 layer was coated using the doctor-blade technique, which became the 1st TiO_2 layer (Figure 5.1(b)). The P4VP was coated on a mesoporous TiO_2 layer (Figure 5.1(c)). Multi-shaped Ag NPs were immobilized on the 1st TiO_2 layer coated with the P4VP, which became the first plasmonic layer (Figure 5.1(d)). The mesoporous TiO_2 layer was recoated using the doctor-blade technique, which became the 2nd TiO_2 layer, and P4VP was recoated on the 2nd TiO_2 layer (Figure 5.1(e)). Subsequently, Au NPs were immobilized on the 2nd TiO_2 layer with the P4VP, which became the second plasmonic layer (Figure 5.1(f)). Finally, the scattering layer was coated using the doctor-blade technique, and the DSSCs were fabricated with an electrolyte and a counter electrode after the removal of the P4VP by sintering (Figure 5.1(g)).

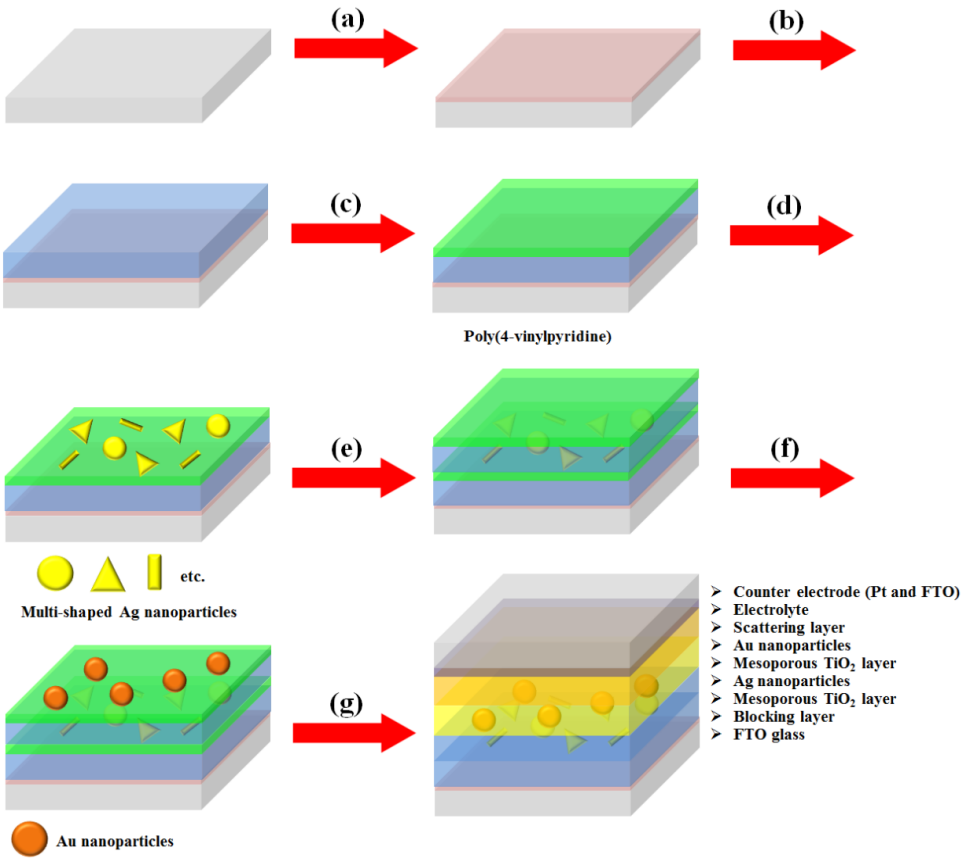

Figure 5. 1. Fabrication process of DSSCs based on the layer-by-layer structure with multi-shaped Ag and Au nanoparticles (NPs): (a) coating of TiO_2 blocking layer, (b) coating of mesoporous TiO_2 layer on TiO_2 blocking layer (c) coating of the poly(4-vinylpyridine) on mesoporous TiO_2 layer, (d) immobilization of multi-shaped Ag NPs, (e) recoating of the mesoporous TiO_2 layer and poly(4-vinylpyridine), (f) immobilization of Au NPs, and (g) fabrication of the DSSC.

5. 4. Fabrication of DSSCs based on composite film structure with multi-shaped Ag and Au nanoparticles.

Another type of DSSC fabricated with a composite film structure was used to confirm the plasmon-enhanced effect of the multi-shaped Ag NPs.[131]

The fabrication of DSSCs based on composite film structure with multi-shaped Ag and Au NPs is shown in Figure 5. 2. Firstly, a TiO_2 blocking layer was coated on FTO glass (Figure 5.2(a)). To prepare the first plasmonic layer for the λ_1 of the N719 dye at 393 nm in the composite film structure of DSSCs, the multi-shaped Ag and mesoporous TiO_2 NPs were mixed and coated on the TiO_2 blocking layer using the doctor-blade technique (Figure 5.2(b)). To prepare the second plasmonic layer for the λ_2 of the N719 dye at 533 nm in the composite film structure of DSSCs, the Au and mesoporous TiO_2 NPs were mixed and coated on the first plasmonic layer using the doctor-blade technique (Figure 5.2(c)). Finally, the scattering layer was coated using the doctor-blade technique, and the DSSCs were fabricated with an electrolyte and a counter electrode (Figure 5.2(d)).

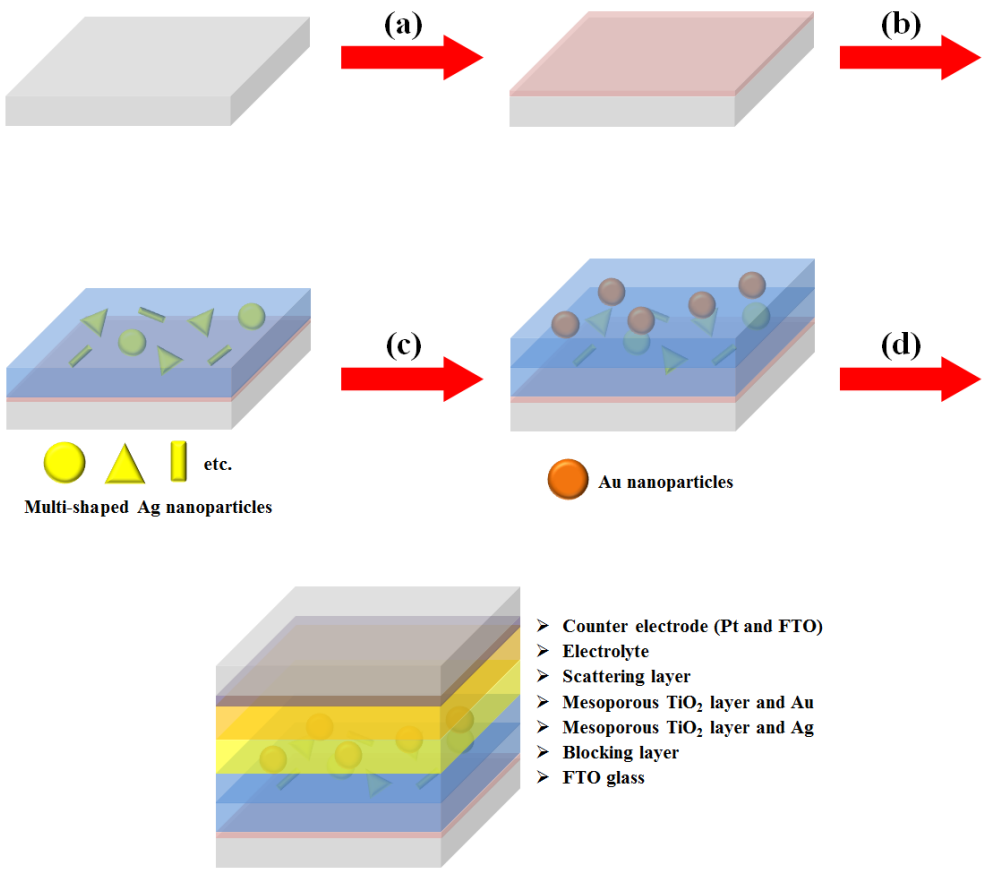

Figure 5. 2. Fabrication process of dye-sensitized solar cells based on a composite film structure with multi-shaped Ag and Au nanoparticles (NPs): (a) coating of TiO_2 blocking layer, (b) coating of multi-shaped Ag NPs and mesoporous TiO_2 NPs, (c) recoating of Au NPs and mesoporous TiO_2 NPs, and (d) fabrication of DSSC.

5. 5. Result and discussion

5. 5. 1. Characterization of Ag nanoparticles by one-step seed-mediated process.

Figure 5.3 shows TEM images of synthesized Ag NPs with different amount of Ag seed solution; 16, 12, 10, 6, 4 mL. When the amount of Ag seed solution was 16 mL, fabricated Ag NPs were spherical, and their average size was ca. 10 nm. When the amount of Ag seed solution was 10 mL, triangular Ag nanoplates were exhibited, and their average size was ca. 15 nm. When the amount of Ag seed solution was 6 mL, dical Ag nanoplates were exhibited, and their average size was ca. 20 nm. In lower amount of Ag seed solution, 4 mL, Ag nanoplates were lager triangular and discal Ag nanoplates, ca. 24 nm. As decrease the amount of Ag seed solution in synthesis process, the average size of fabricated Ag NPs increased, and their shapes changed from sphere to triangular or discal plate.

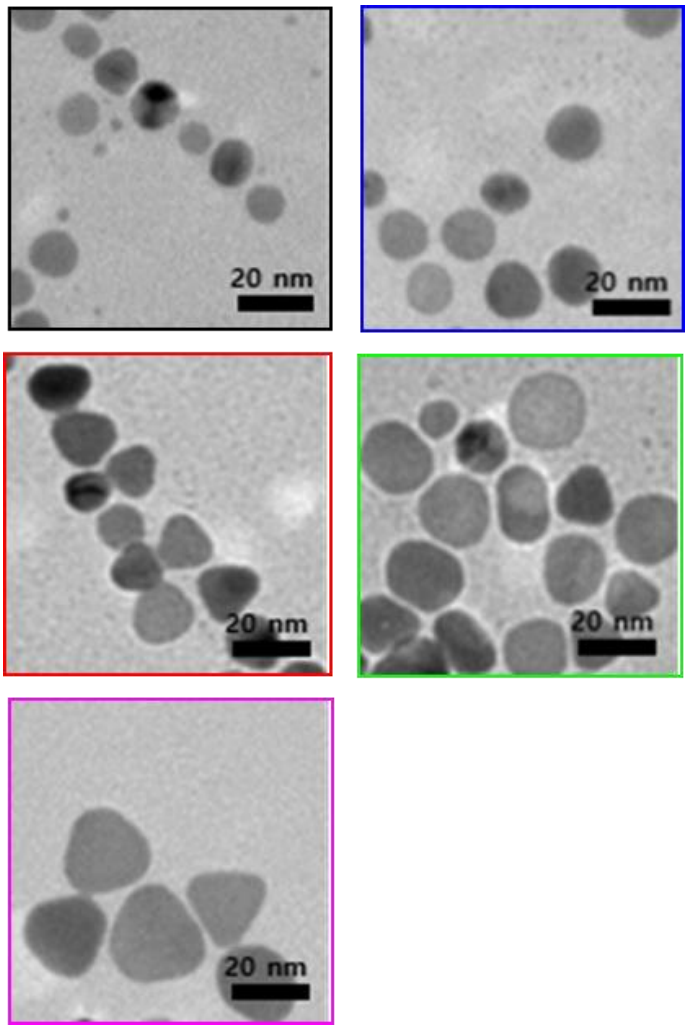

Figure 5. 3. TEM images of Ag nanoparticles which are fabricated by one-step seed-mediated method with different amount of Ag seed solution: 16mL(black), 12mL (blue), 10 mL (red), 6 mL (green), 4 mL (pink).

The UV-visible extinction spectra of the Ag NPs solutions are shown in Figure 5.4. The Ag nanospheres, which were synthesized by one-step seed-mediated method with 16 mL of Ag seed solution, had maximum absorption wavelength (λ_{max}) at ca. 400 nm. (black line in Figure 5.3.) When the Ag tirangular nanoplates were synthesized with 10 mL of Ag seed solution, their λ_{max} red-shifted to ca. 420nm. (red line in Figure 5.3.) The λ_{max} of Ag discal nanoplates, which were synthesized with 6 mL of Ag seed solution, was ca. 495 nm. (green line in Figure 5.3.) As increased the size of Ag discal nanoplates, which were synthesized with 4 mL of Ag seed solution, λ_{max} red-shifted ca. 550 nm. (pink line in Figure 5.3.) As decreased the amount of Ag seed solution in synthesis process, the λ_{max} of Ag nanoparticles solutions red-shifted, from 400 nm to 550 nm, and the intensity of extinction decreased due to the change in the shapes of Ag NPs from nanosphere to discal nanoplate with increase their size.

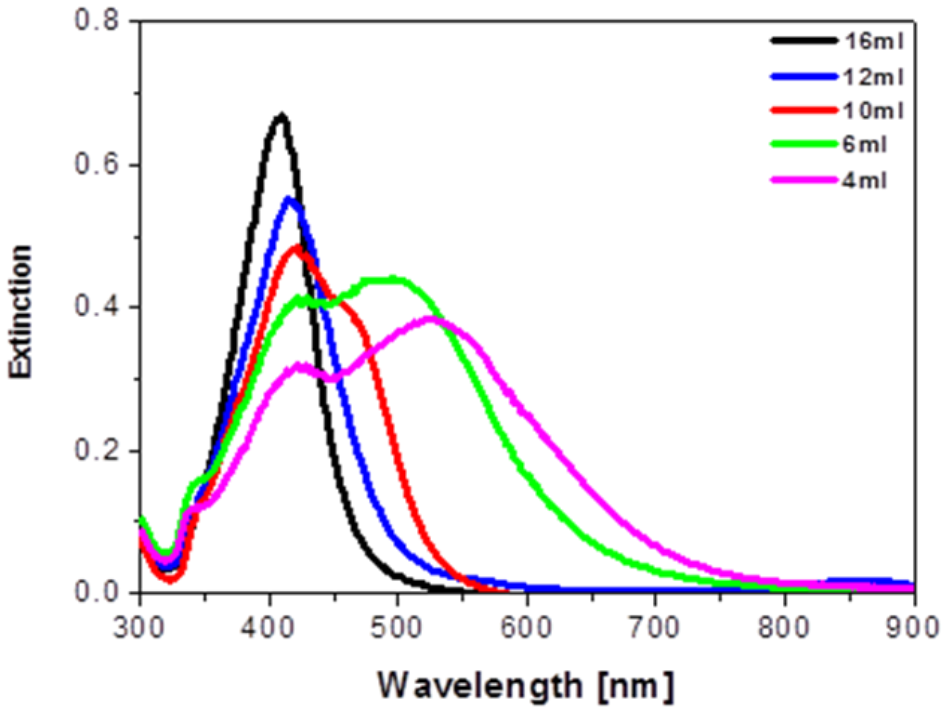

Figure 5. 4. The UV-visible extinction spectra of the Ag nanoparticles solutions which are fabricated by one-step seed-mediated method with different amount of Ag seed solution.

5. 5. 2. Photovoltaic properties of the DSSCs with Ag nanoparticles by one-step seed-mediated process.

To investigate the effect of Ag NPs on the photovoltaic properties of the DSSCs, we fabricated DSSCs with Ag NPs, which are synthesized by one-step seed-mediated process with different amount of Ag seed solution. Figure 5.5 shows the $J-V$ curves obtained from the DSSCs with Ag NPs and the photovoltaic parameters of them are summarized in Table 5.1.

For the DSSCs without Ag NPs, the short-circuit current density (J_{sc}), open-circuit voltage (V_{oc}), fill factor (ff), and PCE were 15.54 mA/cm^2, 0.78 V, 0.68, and 8.24%, respectively. For the DSSCs with Ag nanospheres, which has the average size at ca. 10 nm, J_{sc}, V_{oc}, ff and PCE were 15.95 mA/cm^2, 0.79 V, 0.68 and 8.56 %, repectively. The higer PCE of the DSSC, 9.14%, exhibited in DSSC with trianglular Ag nanoplates, which has the average size at ca. 15 nm. And then, The PCEs of DSSCs decreased when Ag discal nanoplates, which have the average size at 20 nm and 24nm, were incorporated in the DSSCs, 8.41% and 7.80%.

Consequently, the highest PCE of the DSSC exhibited from the DSSC with Ag NPs, which have broad absorption with λ_{max} near 420nm and various shapes such as sphere, rod, triangular plate (so called multi-shaped Ag nanoparticles), due to broad absorption covered with higher energy absorption band of the N719 dye at 393 nm. While the PCE of DSSCs decreased when the Ag NPs, which have λ_{max} over 500 nm and discal plate, were incorporated in

DSSCs, due to decrease in matching with higher energy band of the N719 dye at 393 nm.

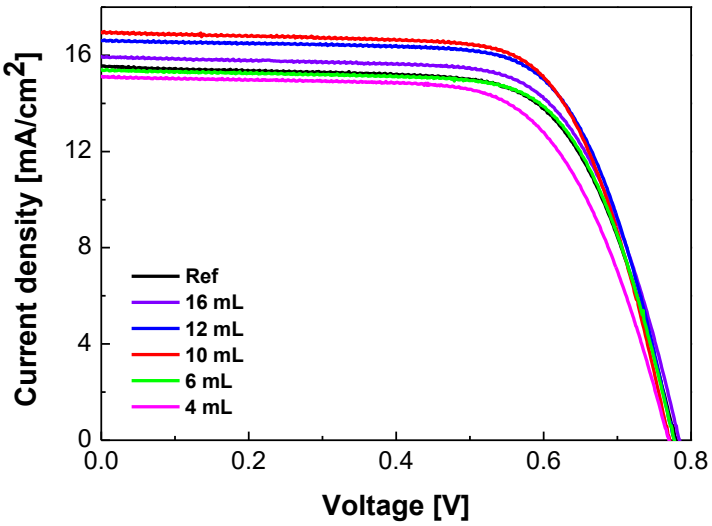

Figure 5. 5. $J-V$ curves of DSSCs with Ag nanoparticles, which are synthesized with different Ag seed solution.

Table 5. 1. Photovoltaic parameters of DSSCs with Ag nanoparticles, which are synthesized with different Ag seed solution.

	J_{sc} (mA/cm²)	V_{oc} (V)	*ff*	η (%)
Ref	15.54	0.78	0.68	8.24
16 mL	15.95	0.79	0.68	8.56
12 mL	16.61	0.78	0.7	9.07
10mL	16.96	0.77	0.7	9.14
6 mL	15.41	0.78	0.7	8.41
4 mL	15.12	0.77	0.67	7.80

5. 5. 3. Characterization of plasmonic layers with Ag and Au Nanoparticles in DSSCs based on layer-by-layer structure

Figure 5.6 shows TEM images of synthesized spherical Ag, multi-shaped Ag, and Au NPs, which were used to fabrication of plasmonic layer in the DSSCs based on layer-by-layer structure, respectively. The Ag and multi-shaped Ag NPs were prepared by the seed-mediated method. The Ag NPs were spherical (Figure 5.6(a)), and their average size was 29±1.8 nm. The multi-shaped Ag NPs comprised spherical, rod, and triangle shapes (Figure 5.6(b). The Au NPs were prepared by the Turkevich method, and their average size was 19±1.5 nm (Figure 5.6(c)). The size distribution histograms of Ag and Au NPs are as shown in Figure 5.7.

Figure 5.8 shows the UV-visible spectra of spherical Ag NPs, multi-shaped Ag NPs, Au NPs, and N719 dye. The N719 dye has two absorption bands which are absorption band at higher energy (393 nm) with a 107 nm FWHM (λ_1) and absorption band at lower energy (533nm) with a 108 nm FWHM (λ_2). The UV-visible spectra of spherical Ag NPs exhibited a λ_{max} of *ca* 400 nm, which was matched by the λ_1 of the N719 dye. However, the FWHM of spherical Ag NPs (61 nm) was narrower than that of the λ_1 of the N719 dye. While, the UV-visible spectra of multi-shaped Ag NPs exhibited a λ_{max} of ca 420 nm, which overlapped with the λ_1 of the N719 dye. The FWHM of multi-shaped Ag nanoparticles (121 nm)

was broader than that of the λ_1 of the N719 dye. For the lower energy band of the N719 dye at 533 nm (λ_2), the Au NPs were introduced on the DSSCs as the 2nd plasmonic layer. The size of the Au NPs was ca 19 nm, and the λ_{max} was 520 nm, which overlapped with the λ_2 of the N719 dye.

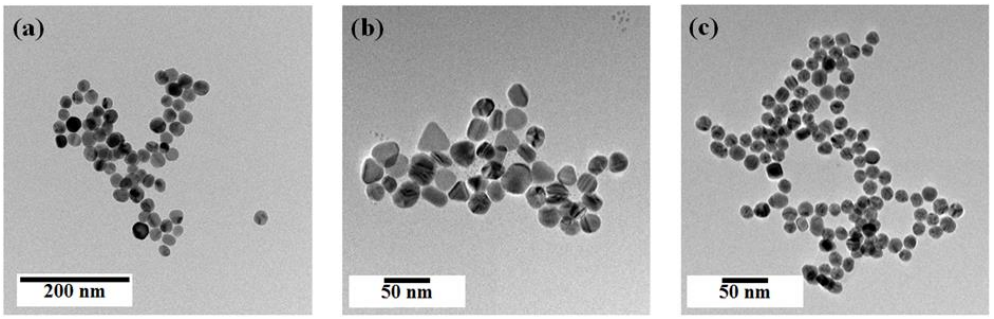

Figure 5. 6. TEM images of (a) spherical Ag nanoparticles, (b) multi-shaped Ag nanoparticles and (c) Au nanoparticles.

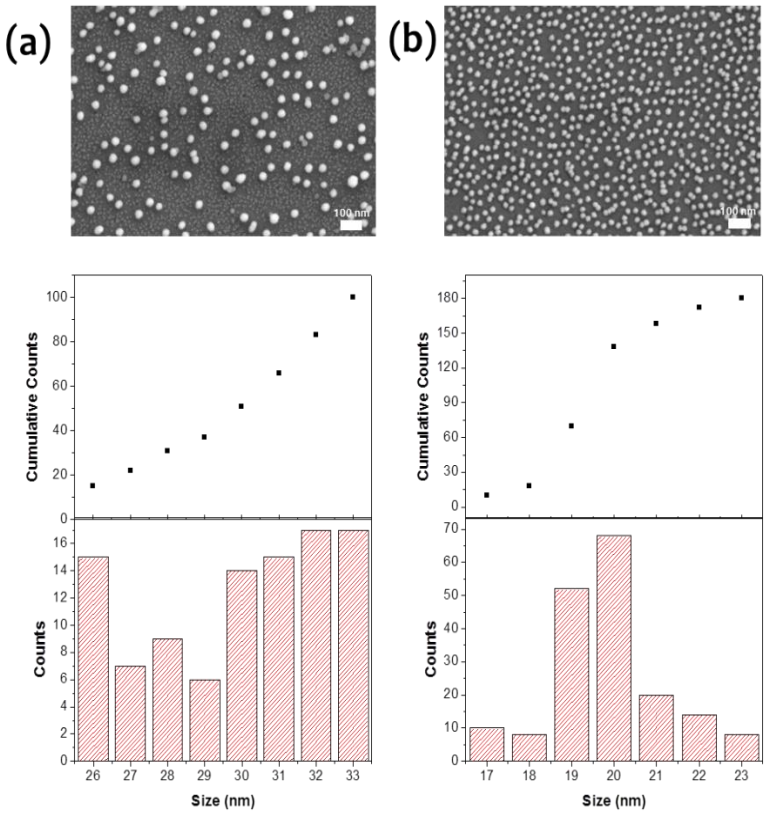

Figure 5. 7. The SEM images and size distribution histograms of (a) immobilized Ag NPs and (b) immobilized Au NPs on film. The average size of Ag and Au NPs is 29±1.8 nm and 19±1.5 nm, respectively.

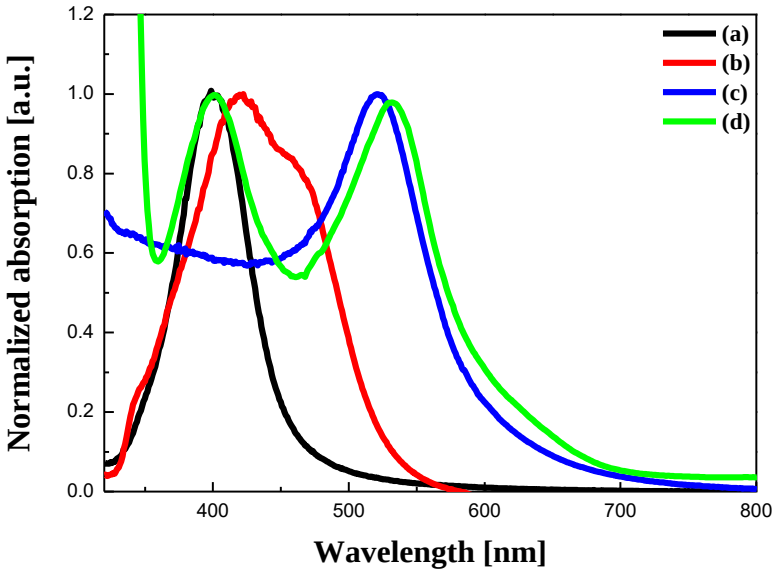

Figure 5. 8. UV-visible spectra of (a) spherical Ag nanoparticles, (b) multi-shaped Ag nanoparticles, (c) Au nanoparticles, and (d) N719 dye.

To compare the effect of spherical Ag and multi-shaped Ag NPs on the photovoltaic properties of DSSCs, we fabricated the DSSCs based on layer-by-layer structure. For the improvement of PCE in DSSCs, the Ag NPs were introduced on the DSSCs as the first plasmonic layer, while the Au NPs were introduced on the DSSCs as the second plasmonic layer in the DSSC based on layer-by-layer structure. In the DSSCs based on a layer-by-layer structure, the metal NPs were immobilized on the mesoporous TiO_2 layer with P4VP. To immobilize the metal NPs, the TiO_2 film coated with P4VP was immersed in metal NP solutions for optimum immobilizing time, 10min for sphericla Ag and multi-shaped Ag NPs and 70min for Au NPs. Figure 5. 9 shows the surface morphology immobilized spherical Ag, multi-shaped Ag or Au NPs, respectively. To confirm that the layer-by-layer structure was maintained in DSSCs, the cross-section image of SEM was obtained from photoanode of DSSC as shown in Figure 5. 10. The thicknesses of the 1^{st} TiO_2 layer, 2^{nd} TiO_2 layer and scattering layer were 5.44㎛, 4.83 ㎛, and 5.67 ㎛, respectively. In the layer-by-layer structure, the existence of Ag and Au NPs in the TiO_2 film was confirmed by the EDX spectra as shown in Figure 5.11. In the layer-by-layer structure, the LSPR field distributions of Au and Ag NPs under the excitation at their plasmon wavelengths were simulated by the finite difference time-domain (FDTD) method as shown in Figure 5. 12. The simulation showed the existence of the local field enhancement of Au and Ag NPs in the layer-by-layer structure.

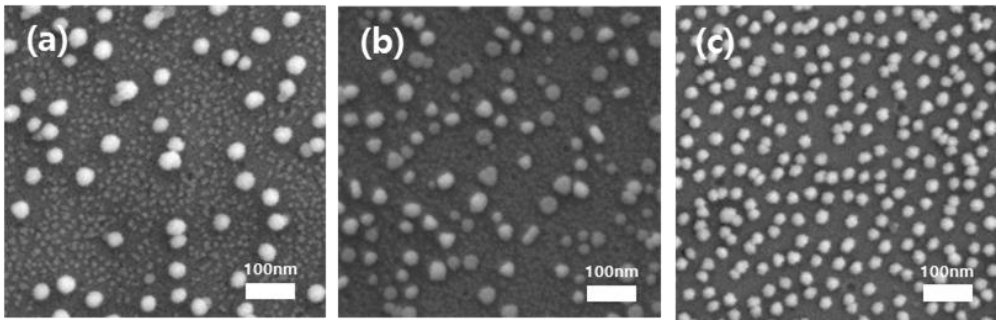

Figure 5. 9. SEM images of immobilized (a) spherical Ag nanoparticles for 10min (b) multi-shaped Ag nanoparticles for 10min (c) Au nanoparticles for 70min on the surface.

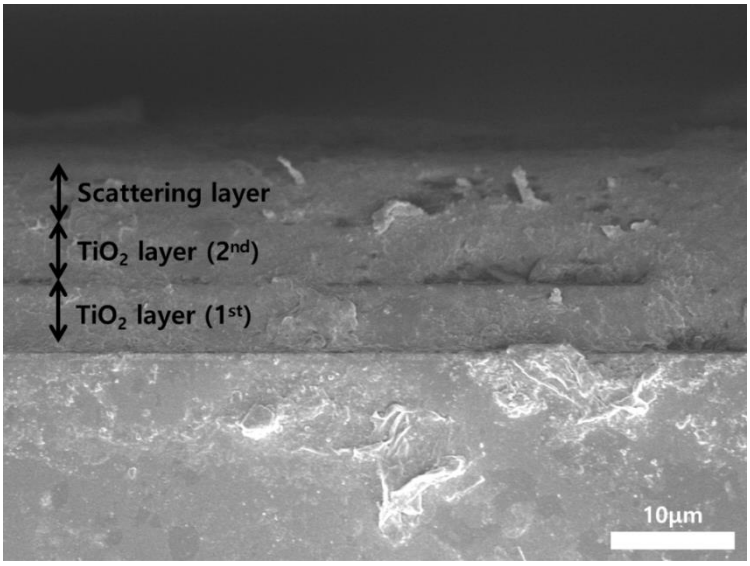

Figure 5. 10. The cross-section image of SEM by photoanode in DSSC based on layer-by-layer structure.

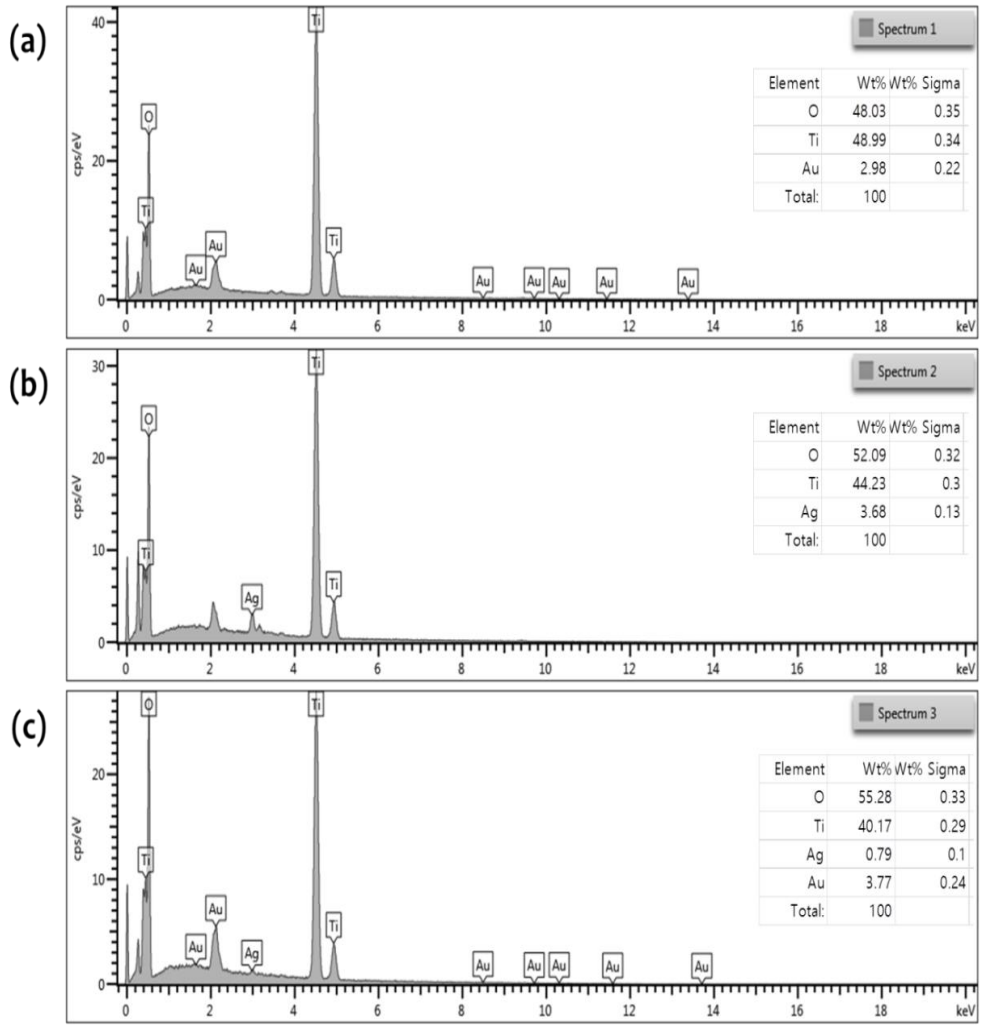

Figure 5. 11. The EDX spectra of (a) TiO_2 film immobilized Au NPs, (b) TiO_2 film immobilized Ag NPs and (c) TiO_2 film immobilized Ag and Au NPs based on layer-by-layer structure.

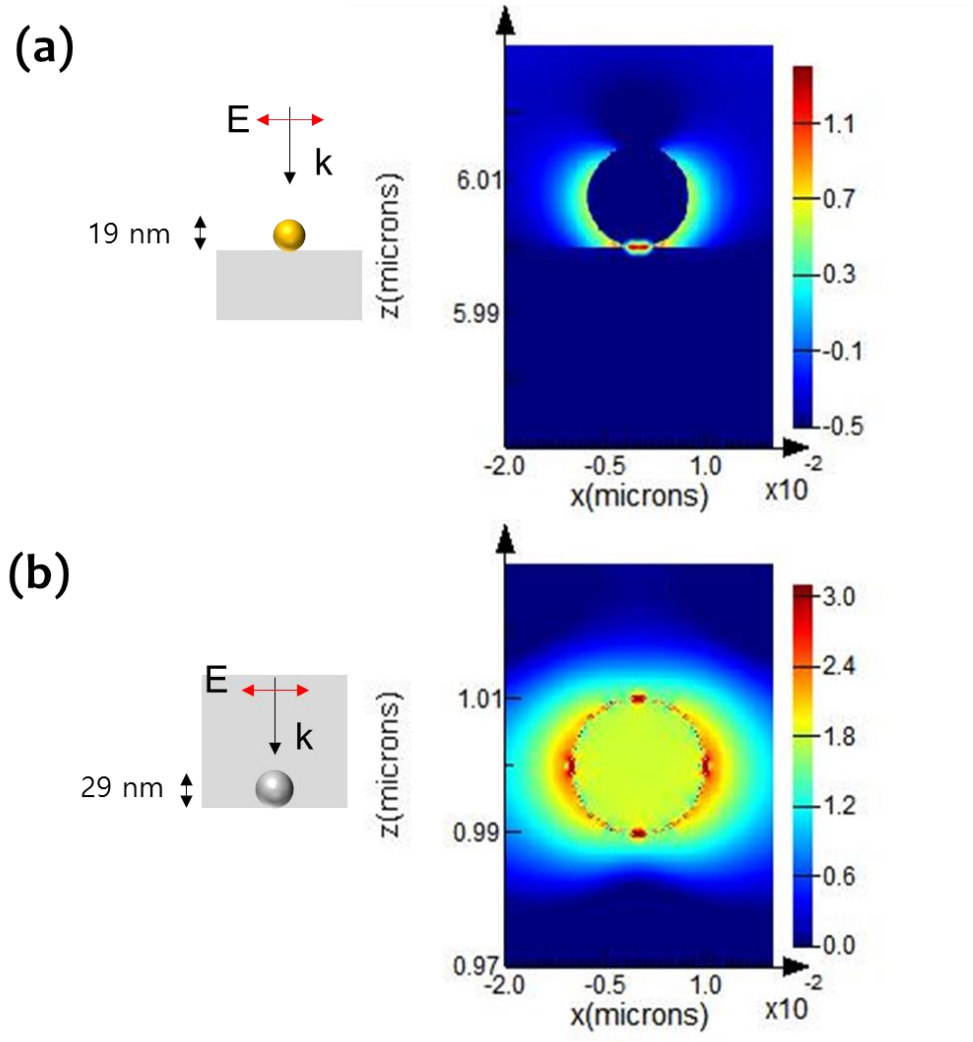

Figure 5. 12. Simulated electric field intensity distributions of (a) Au and (b) Ag NPs under the excitation at their plasmon wavelengths in layer-by-layer structure calculated by the finite difference time-domain (FDTD) method.

5. 5. 4. Photovoltaic properties of the DSSCs with multi-shaped Ag nanoparticles based on the layer-by-layer structure

J-V curves in Figure 5.13 were obtained from the DSSCs based on the layer-by-layer structure without/with spherical Ag NPs, multi-shaped Ag NPs, or Au NPs. The photovoltaic parameters are summarized in Table 5.2. To study the plasmon-enhanced effect with spherical Ag or multi-shaped Ag NPs in 1st plasmonic layer, except the 2nd plasmonic layer, three kinds of DSSCs were fabricated without metal NPs, with spherical Ag NPs, or with multi-shaped Ag NPs. For the DSSCs based on layer-by-layer structure without metal NPs, the photovoltaic parameters J_{sc}, V_{oc}, *ff*, and PCE were 15.86 mA/cm^2, 0.76 V, 0.70, and 8.44%, respectively. For the DSSCs based on layer-by-layer structure with spherical Ag NPs, the photovoltaic parameters J_{sc}, V_{oc}, *ff*, and PCE were 16.58 mA/cm^2, 0.76 V, 0.69, and 8.69%, respectively. For the DSSCs based on layer-by-layer structure with multi-shaped Ag NPs, the photovoltaic parameters J_{sc}, V_{oc}, *ff*, and PCE were 16.73 mA/cm^2, 0.75 V, 0.71, and 8.91%, respectively. Compared to the DSSCs based on layer-by-layer structure without metal NPs, the PCE of DSSCs with spherical Ag NPs increased by 2.96% due to the plasmon-enhanced effect of theh 1st plasmonic layer. Compared to the DSSCs based on layer-by-layer structure with spherical Ag NPs, the PCE of DSSCs with multi-shaped Ag NPs increased by

2.53% due to the plasmon-enhanced effect that covered the broad wavelength range in the short λ_{max} of N719 dye at 393 nm. The total enhancement of DSSCs based on the layer-by-layer structure with multi-shaped Ag NPs increased from 8.44% to 8.91%, corresponding to a 5.57% enhancement.

To improve the PCE of DSSCS, the 2nd plasmonic layer was also introduced on the layer-by-layer structure with Au NPs in DSSCs. Three kinds of DSSCs were fabricated such as the DSSC based on layer-by-layer structuer with Au NPs, spherical Ag and Au NPs, or multi-shaped Ag and Au NPs. For the DSSCs based on layer-by-layer structure with Au NPs, the photovoltaic parameters J_{sc}, V_{oc}, *ff*, and PCE were 17.58 mA/cm^2, 0.75 V, 0.69, and 9.10%, respectively. For the DSSCs based on layer-by-layer structure with spherical Ag and Au NPs, the photovoltaic parameters J_{sc}, V_{oc}, *ff*, and PCE were 19.41 mA/cm^2, 0.75 V, 0.68, and 9.90%, respectively. For the DSSCs based on layer-by-layer structure with multi-shaped Ag and Au NPs, the photovoltaic parameters J_{sc}, V_{oc}, *ff*, and PCE were 19.76 mA/cm^2, 0.75 V, 0.69, and 10.22%, respectively. Compared to the DSSCs based on layer-by-layer structure without metal NPs, the PCE of DSSCs with Au NPs increased by 7.82% due to the plasmon-enhanced effect of the 2nd plasmonic layer. Compared to the DSSCs based on layer-by-layer structure with Au NPs, the PCE of DSSCs with spherical Ag and Au NPs increased by 8.79% due the plasmon-enhanced effect of the 1st plasmonic layer. Compared to the DSSCs based on layer-by-layer structure with spherical Ag and Au NPs, the PCE of DSSCs with multi-shaped Ag

and Au NPs increased by 3.23% due to the plasmon-enhanced effect that covered the broad wavelength range in the short λ_{max} of N719 dye at 393 nm. The total enhancement of DSSCs based on the layer-by-layer structure with multi-shaped Ag and Au NPs increased from 8.44% to 10.22%, corresponding to a 21.09% enhancement. This means that the PCE of DSSCs with spherical Ag NPs or multi-shaped Ag NPs was improved by the plasmon-enhanced effect, and the DSSCs with multi-shaped Ag NPs, which covered the broad wavelength range in the λ_1 of N719 dye, exhibited better PCE than DSSCs with spherical Ag NPs.

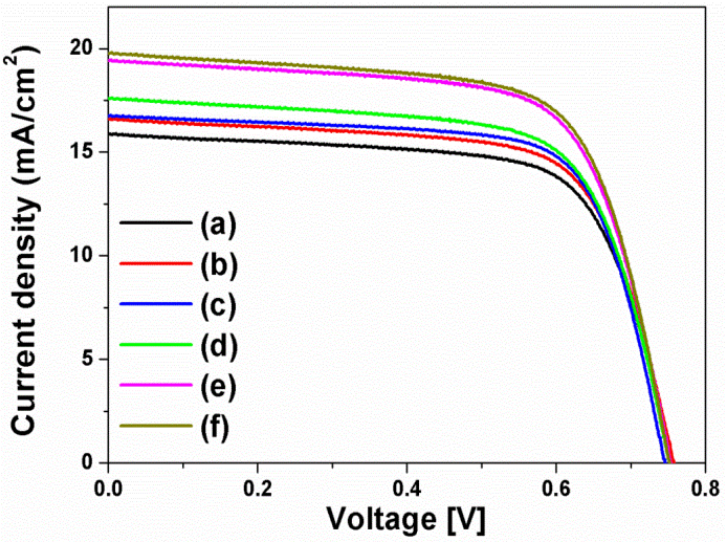

Figure 5. 13. $J-V$ curves of DSSCs based on a layer-by-layer structure: (a) without metal nanoparticles; (b) with spherical Ag Nanoparticles; (c) with multi-shaped Ag nanoparticles; (d) with Au Nanoparticles; (e) with spherical Ag and Au nanoparticles; and (f) with multi-shaped Ag and Au nanoparticles.

Table 5. 2. Photovoltaic parameters of dye-sensitized solar cells (DSSCs) based on layer-by-layer structure.

DSSCs based on layer-by-layer structure	J_{sc} (mA/cm²)	V_{oc} (V)	*ff*	η (%)
(a)Without metal NPs	15.86	0.76	0.70	8.44
(b) With spherical Ag NPs	16.58	0.76	0.69	8.69
(c) With multi-shaped Ag NPs	16.73	0.75	0.71	8.91
(d) With Au NPs	17.58	0.75	0.69	9.10
(e) With spherical Ag NPs and Au NPs	19.41	0.75	0.68	9.90
(f) With multi-shaped Ag NPs and Au NPs	19.76	0.75	0.69	10.22

5. 5. 5. Photovoltaic properties of the DSSCs with multi-shaped Ag nanoparticles based on composite film structure.

To confirm the plasmon-enhanced effect of the multi-shaped Ag NPs, another type of DSSC fabricated with a composite film structure was used.

The $J-V$ curves were measured from DSSCs based on the composite film structure with spherical Ag, multi-shaped Ag, or Au NPs as shown in Figure 5.14, and the photovoltaic parameters of the DSSCs are summarized in Table 5.3. To study the plasmon-enhanced effect of the 1st plasmonic layer with spherical Ag NPs or multi-shaped Ag NPs, excluding the 2nd plasmonic layer, three types of DSSCs were fabricated without metal NPs, with spherical Ag NPs, or with multi-shaped Ag NPs. For the DSSCs based on the composite film structure without metal NPs, the photovoltaic parameters J_{sc}, V_{oc}, *ff*, and PCE were 15.09 mA/cm^2, 0.77 V, 0.73, and 8.48%, respectively. For the DSSCs based on the composite film structure with spherical Ag NPs, the photovoltaic parameters J_{sc}, V_{oc}, *ff*, and PCE were 15.72 mA/cm^2, 0.77 V, 0.73, and 8.84%, respectively. For the DSSCs based on the composite film structure with multi-shaped Ag NPs, the photovoltaic parameters J_{sc}, V_{oc}, *ff*, and PCE were 15.81 mA/cm^2, 0.78 V, 0.73, and 9.00%, respectively. Compared to the DSSCs based on the composite film structure without metal NPs, the PCE of DSSCs with spherical Ag

nanoparticles increased by 4.25% due to the plasmon-enhanced effect of the 1st plasmonic layer. Compared to the DSSCs based on the composite film structure with spherical Ag NPs, the PCE of DSSCs with multi-shaped Ag NPs increased by 1.81% due to the plasmon-enhanced effect, which covered the broad wavelength range in the λ_1 of N719 dye. In total, the enhancement of the DSSCs based on the composite film structure with multi-shaped Ag NPs increased from 8.48% to 9.00%, corresponding to a 6.13% enhancement.

To improve the PCE of DSSCs with the first plasmon-enhanced effect using spherical Ag or multi-shaped Ag NPs, the second plasmonic layer was introduced on the composite film structure with Au NPs, spherical Ag and Au NPs, and multi-shaped Ag and Au NPs in the photoactive layer of DSSCs. For the DSSCs based on the composite film structure with Au NPs, the photovoltaic parameters J_{sc}, V_{oc}, *ff*, and PCE were 16.72 mA/cm^2, 0.78 V, 0.72, and 9.34%, respectively. For the DSSCs based on the composite film structure with spherical Ag and Au NPs, the photovoltaic parameters J_{sc}, V_{oc}, *ff*, and PCE were 17.07 mA/cm^2, 0.78 V, 0.75, and 9.99%, respectively. For the DSSCs based on the composite film structure with multi-shaped Ag and Au NPs, the photovoltaic parameters J_{sc}, V_{oc}, *ff*, and PCE were 17.91 mA/cm^2, 0.78 V, 0.74, and 10.34%, respectively. Compared to the DSSCs based on the composite film structure without metal NPs, the PCE of DSSCs with Au NPs increased by 8.86% due to the plasmon-enhanced effect of the 2nd plasmonic layer. Compared to the DSSCs based on the composite

film structure with Au NPs, the PCE of DSSCs with spherical Ag and Au NPs increased by 6.96% due the plasmon-enhanced effect of the 1st plasmonic layer. Compared to the DSSCs based on the composite film structure with spherical Ag and Au NPs, the PCE of DSSCs with multi-shaped Ag and Au NPs increased by 3.50% due to the plasmon-enhanced effect, which covered the broad wavelength range in the λ_1 of N719 dye. In total, the enhancement of the DSSCs based on the composite film structure with multi-shaped Ag and Au NPs increased from 8.48% to 10.34%, corresponding to an improvement of 21.93%. Similar to the layer-by-layer structure, the PCE of the composite film structure in DSSCs with spherical Ag or multi-shaped Ag NPs was improved by the plasmon-enhanced effect of the 1st plasmonic layer, and the DSSCs with multi-shaped Ag NPs, which have broader absorption wavelengths range in the λ_1 of N719 dye, exhibited better PCE than the DSSCs with spherical Ag NPs.

Compared with DSSCs based on the layer-by-layer structure and based on the composite film structure, the J_{sc} and V_{oc} are different. Kamat's group reported that there are two kinds of plasmonics; "plasmonic effect" and "charging effect".[113] When DSSCs were fabricated with the layer-by-layer structure, the spherical Ag or multi-shaped Ag NPs were introduced onto the TiO_2 film. In this case, the most electrons are transferred to TiO_2 that changes J_{sc}. So the main role of spherical Ag or multi-shaped Ag NPs in DSSCs based on the layer-by-layer structure is the light harvesting that is similar to "plasmonic effect". However, when

DSSCs were fabricated with the composite film structure, the spherical Ag or multi-shaped Ag NPs were mixed with TiO_2 films. In this case, some electrons are transferred to TiO_2 NPs, spherical Ag NPs, or multi-shaped Ag NPs that change the electron density and Fermi level on TiO_2 composite film structure. When electrons are transferred to TiO_2 NPs, the J_{sc} will be changed. But when electrons are transferred to spherical Ag or multi-shaped Ag NPs, the Fermi level is more negative potential that reflected to the V_{oc} and the electron density is more increased that reflected to *ff*. So the main role of spherical Ag or multi-shaped Ag NPs in DSSCs based on the composite film structure is the improvement of electron density that is similar to "charging effect".

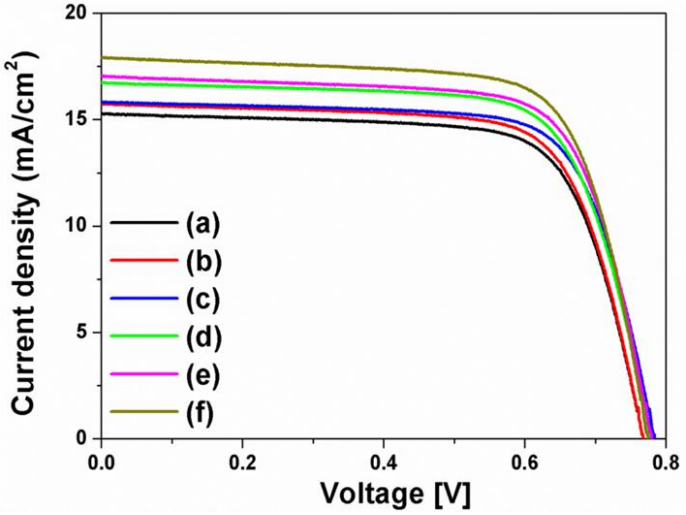

Figure 5. 14. $J-V$ curves of DSSCs based on the composite film structure (a) without metal nanoparticles, (b) with spherical Ag nanoparticles, (c) with multi-shaped Ag nanoparticles, (d) with Au nanoparticles, (e) with spherical Ag and Au nanoparticles, or (f) with multi-shaped Ag and Au nanoparticles.

Table 5. 3. Photovoltaic parameters of dye-sensitized solar cells (DSSCs) based on composite film structure.

DSSCs based on Composite film structure	J_{sc} (mA/cm^2)	V_{oc} (V)	ff	η (%)
(a)Without metal NPs	15.09	0.77	0.73	8.48
(b) With spherical Ag NPs	15.72	0.77	0.73	8.84
(c) With multi-shaped Ag NPs	15.81	0.78	0.73	9.00
(d) With Au NPs	16.72	0.78	0.72	9.34
(e) With spherical Ag NPs and Au NPs	17.07	0.78	0.75	9.99
(f) With multi-shaped Ag NPs and Au NPs	17.91	0.78	0.74	10.34

5. 5. 6. Plasmonic effect of multi-shaped Ag nanoparticles

Figure 5.15 shows the incident photon-to-electron conversion efficiency (IPCE) and integrated current densities of DSSCs based on the layer-by-layer structure without metal NPs, with spherical Ag and Au NPs, or with multi-shaped Ag and Au NPs. The intensity of the DSSCs without metal NPs was lower than those with Ag and Au NPs. In the DSSCs with Au NPs, the light absorption peak at 540 nm was higher and followed the same pattern. However, in the DSSCs with spherical Ag or multi-shaped Ag NPs, the light absorption peaks were also higher, but followed different patterns. The IPCE of the DSSCs with spherical Ag NPs had a narrow light absorption peak at 390 nm, matching the UV-Visible spectrum of spherical Ag NPs. Meanwhile, the IPCE of the DSSCs with multi-shaped Ag NPs had a broad light absorption peak at 420 nm matching the UV-visible spectrum of multi-shaped Ag NPs. This means that not only is plasmonic enhancement dependent on the light absorption of metal NPs, but also that the efficiency is improved by more electron generation within these wavelength ranges. Regarding the IPCE, both of the maximum light absorption peaks from the DSSCs were related to Ag NPs in the 1^{st} plasmonic layer and Au NPs in the 2^{nd} plasmonic layer. The 2^{nd} plasmonic layer with Au NPs showed the same patterned light absorption peaks at 540 nm in the DSSCs with spherical or multi-shaped Ag NPs. The

1st plasmonic layer of the DSSCs with spherical Ag NPs showed a narrow light absorption peak, while that of the DSSC with multi-shaped Ag NPs showed a broad light absorption peak following a similar pattern to the UV-visible spectra shown in Figure 5.7. This means more electrons were generated from N719 dye due to the light absorption of multi-shaped Ag NPs, affecting the PCE of the DSSCs. The integrated current density of DSSCs based on the layer-by-layer structure without metal NPs, with spherical Ag and Au NPs, or with multi-shaped Ag and Au NPs from the IPCE spectra are 15.83, 17.76 and 18.30 mA/cm^2 respectively, as shown in Figure 5.15. There is difference between these values and the J_{sc} obtained from the $J-V$ curves. Due to difference in the measurement of $J-V$ and IPCE, the difference between J_{sc} from $J-V$ curve and the integrated current density from IPCE spectra is generally observed. However, both of them exhibited similar tendency of increase.

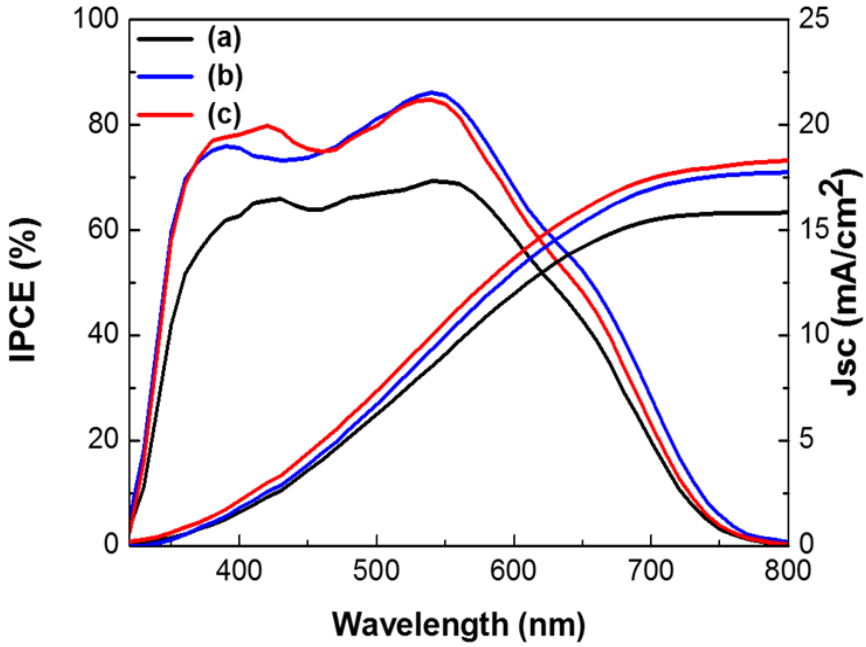

Figure 5. 15. IPCE spectra and integrated current density of the DSSCs based on layer-by-layer structure: (a) without metal NPs, (b) with spherical Ag and Au NPs, and (c) with multi-shaped Ag and Au NPs.

Figure 5.16 shows the UV−visible extinction spectra of TiO_2 nanoparticles film and layer−by−layer TiO_2 film consisting of Multi−shaped Ag and Au NPs before and after N719 dye adsorption. All of the films were treated with TIP solution. Before N719 dye adsorption, there is no significant increase in the intensity of the UV−visible extinction spectra. While after N719 dye adsorption, there is a significant increase in the intensity of the UV−visible extinction spectra. The intensity of the peaks corresponding to the localized surface plasmon resonances of multi−shaped Ag and Au NPs, near 420 and 530 nm, is significantly higher in the extinction spectrum measured from the layer−by−layer TiO_2 film consisting of multi−shaped Ag and Au NPs than that measured from the TiO_2 nanoparticles film. The number of dye molecules adsorbed on both films was almost equal, since the thickness of both films was the same. The higher extinction intensity is due to the plasmonic effects of metal NPs. An enhanced light absorption of dye molecules could take place on or near surface of metal NPs and far surface of metal NPs.

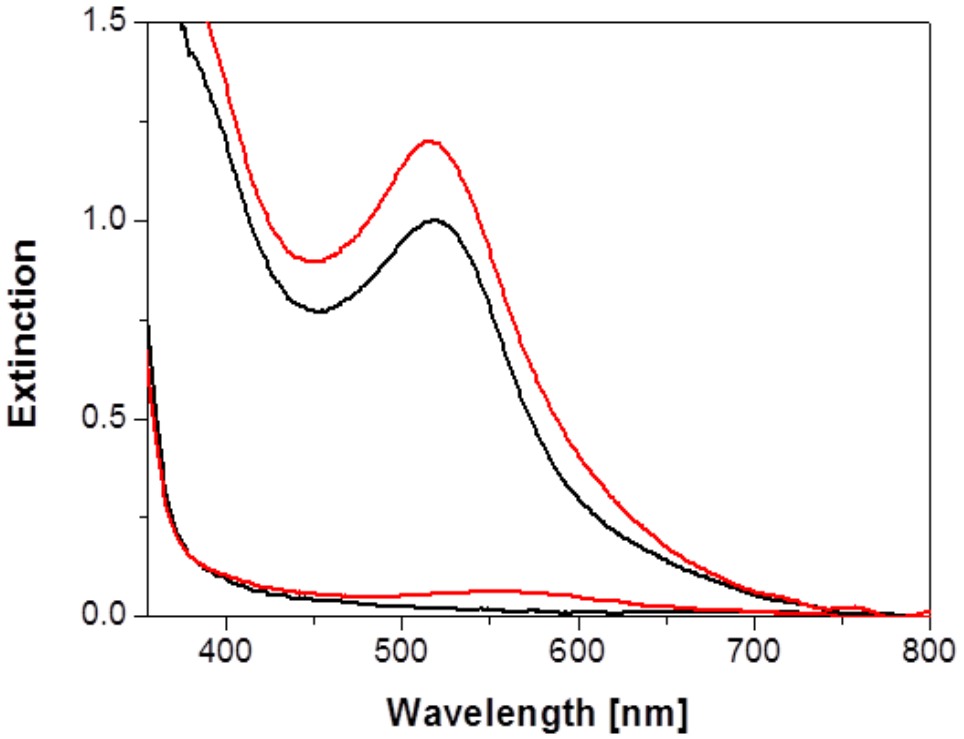

Figure 5. 16. Extinction spectra of TiO_2 nanoparticles film (black) and layer-by-layer film consisting of multi-shaped Ag and Au nanoparticles (red) before (bottom two spectra) and after N719 dye adsorption. Both films were treated with TIP before adsorption of dye molecules.

5. 6. Conclusion

As increase amount of Ag seed solution in one-step seed-mediated process, the shape of Ag NPs changes from sphere to discal plate with increasing their size, and their λ_{max} red-shifted, from 400 nm to 550 nm. In DSSCs with fabricated Ag NPs, the DSSC with Ag NPs, which have broad absorption with λ_{max} near 420nm and multi-shaped Ag nanoparticles, has the highest PCE due to broad absorption covered with λ_1 of the N719 dye at 393 nm.

For both of DSSCs based on the layer-by-layer and composite film structures, the PCE of DSSCs with multi-shaped Ag NPs was better than that of DSSCs with spherical Ag NPs which have λ_{max} near 400nm. The enhancement of the DSSC with multi-shaped Ag NPs was cause by broad absorption compared to spherical Ag NPs.

Reference

1. Holdren, J.P. and P.R. Ehrlich, *Human Population and the Global Environment: Population growth, rising per capita material consumption, and disruptive technologies have made civilization a global ecological force.* American scientist, 1974. **62**(3): p. 282-292.
2. Kasimir-Klemedtsson, Å., et al., *Greenhouse gas emissions from farmed organic soils: a review.* Soil use and management, 1997. **13**(s4): p. 245-250.
3. Kumar, V., R. Shrivastava, and S. Untawale, *Solar Heating for Industrial Process Heat: Step Towards Eco-friendly and Sustainable Technology.* SOLAR ENERGY, 2013. **20**: p. 22.
4. Riti, J.S. and Y. Shu, *Renewable energy, energy efficiency, and eco-friendly environment (R-E5) in Nigeria.* Energy, Sustainability and Society, 2016. **6**(1): p. 1-16.
5. Choubey, P., A. Oudhia, and R. Dewangan, *A review: Solar cell current scenario and future trends.* Recent Research in Science and Technology, 2012. **4**(8).
6. Kibria, M., et al. *A Review: Comparative studies on different generation solar cells technology, Int*. in *Conf. Environ. Asp. Bangladesh*. 2014.
7. Parida, B., S. Iniyan, and R. Goic, *A review of solar photovoltaic technologies.* Renewable and sustainable energy reviews, 2011. **15**(3): p. 1625-1636.
8. Bernede, J., *Organic photovoltaic cells: history, principle and techniques.* Journal of the Chilean Chemical Society, 2008. **53**(3): p. 1549-1564.
9. Bae, S.-H., et al., *Printable Solar Cells from Advanced Solution-Processible Materials.* Chem, 2016. **1**(2): p. 197-219.
10. Alicki, R., D. Gelbwaser-Klimovsky, and A. Jenkins, *A thermodynamic cycle for the solar cell.* Annals of Physics, 2017.
11. Khan, M.I., *A Study on the Optimization of Dye-Sensitized Solar Cells.* 2013.
12. Kasap, S. and P. Capper, *Springer handbook of electronic and photonic materials*. 2006: Springer Science & Business Media.
13. Bartesaghi, D., et al., *Competition between recombination and extraction of free charges determines the fill factor of organic solar cells.* Nature communications, 2015. **6**.

14. Van Dyk, E. and E. Meyer, *Analysis of the effect of parasitic resistances on the performance of photovoltaic modules.* Renewable energy, 2004. **29**(3): p. 333-344.
15. Hagfeldt, A. and M. Graetzel, *Light-induced redox reactions in nanocrystalline systems.* Chemical Reviews, 1995. **95**(1): p. 49-68.
16. Zhao, H., *Light Trapping for Silicon Solar Cells: Theory and Experiment.* 2013.
17. Corazza, M., *Characterization of Organic Solar Cell Devices and their Interfaces under Degradation: Imaging, Electrical and Mechanical Methods.* 2016.
18. Nazeeruddin, M.K., et al., *Conversion of light to electricity by cis-X2bis (2, 2'-bipyridyl-4, 4'-dicarboxylate) ruthenium (II) charge-transfer sensitizers (X= Cl-, Br-, I-, CN-, and SCN-) on nanocrystalline titanium dioxide electrodes.* Journal of the American Chemical Society, 1993. **115**(14): p. 6382-6390.
19. Juan, M.L., M. Righini, and R. Quidant, *Plasmon nano-optical tweezers.* Nature Photonics, 2011. **5**(6): p. 349-356.
20. Garcés-Chávez, V., et al., *Extended organization of colloidal microparticles by surface plasmon polariton excitation.* Physical Review B, 2006. **73**(8): p. 085417.
21. Zayats, A.V., I.I. Smolyaninov, and A.A. Maradudin, *Nano-optics of surface plasmon polaritons.* Physics reports, 2005. **408**(3): p. 131-314.
22. Zayats, A.V. and I.I. Smolyaninov, *Near-field photonics: surface plasmon polaritons and localized surface plasmons.* Journal of Optics A: Pure and Applied Optics, 2003. **5**(4): p. S16.
23. Volpe, G., et al., *Surface plasmon radiation forces.* Physical review letters, 2006. **96**(23): p. 238101.
24. Linic, S., P. Christopher, and D.B. Ingram, *Plasmonic-metal nanostructures for efficient conversion of solar to chemical energy.* Nature materials, 2011. **10**(12): p. 911-921.
25. Jatschka, J., et al., *Propagating and localized surface plasmon resonance sensing—A critical comparison based on measurements and theory.* Sensing and Bio-Sensing Research, 2016. **7**: p. 62-70.
26. Van Duyne, R.P., *Molecular plasmonics.* Science, 2004. **306**(5698): p. 985-986.
27. Haes, A.J., et al., *Plasmonic materials for surface-enhanced*

sensing and spectroscopy. MRS bulletin, 2005. **30**(05): p. 368-375.
28. Zhang, X., et al., *Rapid detection of an anthrax biomarker by surface-enhanced Raman spectroscopy.* Journal of the American Chemical Society, 2005. **127**(12): p. 4484-4489.
29. Brolo, A.G., *Plasmonics for future biosensors.* Nature Photonics, 2012. **6**(11): p. 709-713.
30. Homola, J., S.S. Yee, and G. Gauglitz, *Surface plasmon resonance sensors: review.* Sensors and Actuators B: Chemical, 1999. **54**(1): p. 3-15.
31. Haes, A.J. and R.P. Van Duyne, *A unified view of propagating and localized surface plasmon resonance biosensors.* Analytical and bioanalytical chemistry, 2004. **379**(7-8): p. 920-930.
32. Murray, W.A. and W.L. Barnes, *Plasmonic materials.* Advanced materials, 2007. **19**(22): p. 3771-3782.
33. Zhang, J., L. Zhang, and W. Xu, *Surface plasmon polaritons: physics and applications.* Journal of Physics D: Applied Physics, 2012. **45**(11): p. 113001.
34. Willets, K.A. and R.P. Van Duyne, *Localized surface plasmon resonance spectroscopy and sensing.* Annu. Rev. Phys. Chem., 2007. **58**: p. 267-297.
35. Nath, N. and A. Chilkoti, *Label-free biosensing by surface plasmon resonance of nanoparticles on glass: optimization of nanoparticle size.* Analytical Chemistry, 2004. **76**(18): p. 5370-5378.
36. Haynes, C.L. and R.P. Van Duyne, *Nanosphere lithography: a versatile nanofabrication tool for studies of size-dependent nanoparticle optics*. 2001, ACS Publications.
37. Jensen, T.R., et al., *Nanosphere lithography: tunable localized surface plasmon resonance spectra of silver nanoparticles.* The Journal of Physical Chemistry B, 2000. **104**(45): p. 10549-10556.
38. Jensen, T.R., et al., *Nanosphere lithography: effect of the external dielectric medium on the surface plasmon resonance spectrum of a periodic array of silver nanoparticles.* The Journal of Physical Chemistry B, 1999. **103**(45): p. 9846-9853.
39. Miller, M.M. and A.A. Lazarides, *Sensitivity of metal nanoparticle surface plasmon resonance to the dielectric environment.* The Journal of Physical Chemistry B, 2005. **109**(46): p. 21556-

21565.
40. Kelly, K.L., et al., *The optical properties of metal nanoparticles: the influence of size, shape, and dielectric environment*. 2003, ACS Publications.
41. Kim, S.-S., et al., *Plasmon enhanced performance of organic solar cells using electrodeposited Ag nanoparticles.* Applied Physics Letters, 2008. **93**(7): p. 305.
42. Rand, B.P., P. Peumans, and S.R. Forrest, *Long-range absorption enhancement in organic tandem thin-film solar cells containing silver nanoclusters.* Journal of Applied Physics, 2004. **96**(12): p. 7519-7526.
43. Huber, E. and M. Frost, *Light scattering by small particles.* Journal of Water Supply: Research and Technology-Aqua, 1998. **47**(2): p. 87-94.
44. Christopher, P., D.B. Ingram, and S. Linic, *Enhancing photochemical activity of semiconductor nanoparticles with optically active Ag nanostructures: photochemistry mediated by Ag surface plasmons.* The Journal of Physical Chemistry C, 2010. **114**(19): p. 9173-9177.
45. Burda, C., et al., *Chemistry and properties of nanocrystals of different shapes.* Chemical reviews, 2005. **105**(4): p. 1025-1102.
46. Lee, J., et al., *Bioconjugated Ag Nanoparticles and CdTe Nanowires: Metamaterials with Field-Enhanced Light Absorption.* Angewandte Chemie International Edition, 2006. **45**(29): p. 4819-4823.
47. Vo-Dinh, T., *Surface-enhanced Raman spectroscopy using metallic nanostructures.* TrAC Trends in Analytical Chemistry, 1998. **17**(8): p. 557-582.
48. Cao, Y.C., R. Jin, and C.A. Mirkin, *Nanoparticles with Raman spectroscopic fingerprints for DNA and RNA detection.* Science, 2002. **297**(5586): p. 1536-1540.
49. Shipway, A.N., E. Katz, and I. Willner, *Nanoparticle arrays on surfaces for electronic, optical, and sensor applications.* ChemPhysChem, 2000. **1**(1): p. 18-52.
50. Anger, P., P. Bharadwaj, and L. Novotny, *Enhancement and quenching of single-molecule fluorescence.* Physical review letters, 2006. **96**(11): p. 113002.
51. Munday, J.N. and H.A. Atwater, *Large integrated absorption*

enhancement in plasmonic solar cells by combining metallic gratings and antireflection coatings. Nano letters, 2010. **11**(6): p. 2195-2201.
52. Ferry, V.E., et al., *Plasmonic nanostructure design for efficient light coupling into solar cells.* Nano letters, 2008. **8**(12): p. 4391-4397.
53. Pala, R.A., et al., *Design of plasmonic thin-film solar cells with broadband absorption enhancements.* Advanced Materials, 2009. **21**(34): p. 3504-3509.
54. Atwater, H.A. and A. Polman, *Plasmonics for improved photovoltaic devices.* Nature materials, 2010. **9**(3): p. 205-213.
55. Nguyen, B.H., V.H. Nguyen, and D.L. Vu, *Plasmonic enhancement of light trapping into organic solar cells.* Advances in Natural Sciences: Nanoscience and Nanotechnology, 2015. **6**(4): p. 043002.
56. Stenzel, O., et al., *Enhancement of the photovoltaic conversion efficiency of copper phthalocyanine thin film devices by incorporation of metal clusters.* Solar energy materials and solar cells, 1995. **37**(3-4): p. 337-348.
57. Derkacs, D., et al., *Improved performance of amorphous silicon solar cells via scattering from surface plasmon polaritons in nearby metallic nanoparticles.* Applied Physics Letters, 2006. **89**(9): p. 093103.
58. Faraday, M., *Experimental relations of gold (and other metals) to light.* Phil. Trans. Roy. Soc. London, 1857. **147**: p. 145-181.
59. Park, H.J. and L.J. Guo, *Optical enhancement effects of plasmonic nanostructures on organic photovoltaic cells.* Chinese Chemical Letters, 2015. **26**(4): p. 419-425.
60. Zheng, X. and L. Zhang, *Photonic nanostructures for solar energy conversion.* Energy & Environmental Science, 2016. **9**(8): p. 2511-2532.
61. Beck, F., A. Polman, and K. Catchpole, *Tunable light trapping for solar cells using localized surface plasmons.* Journal of Applied Physics, 2009. **105**(11): p. 114310.
62. Navalon, S., et al., *Enhancement of the catalytic activity of supported gold nanoparticles for the Fenton reaction by light.* Journal of the American Chemical Society, 2011. **133**(7): p. 2218-2226.
63. Wiley, B.J., et al., *Maneuvering the surface plasmon resonance*

of silver nanostructures through shape-controlled synthesis. 2006, ACS Publications.
64. Wiley, B., Y. Sun, and Y. Xia, *Synthesis of silver nanostructures with controlled shapes and properties.* Accounts of Chemical Research, 2007. **40**(10): p. 1067-1076.
65. Wiley, B., et al., *Shape-controlled synthesis of metal nanostructures: the case of silver.* Chemistry-A European Journal, 2005. **11**(2): p. 454-463.
66. Lu, X., et al., *Chemical synthesis of novel plasmonic nanoparticles.* Annual review of physical chemistry, 2009. **60**: p. 167-192.
67. Logothetidis, S., *Nanotechnology: Principles and applications*, in *Nanostructured Materials and Their Applications*. 2012, Springer. p. 1-22.
68. Mijatovic, D., J. Eijkel, and A. Van Den Berg, *Technologies for nanofluidic systems: top-down vs. bottom-up—a review.* Lab on a Chip, 2005. **5**(5): p. 492-500.
69. Koch, C., *Top-Down Synthesis Of Nanostructured Materials: Mechanical And Thermal Processing Methods.* Reviews on Advanced Materials Science, 2003. **5**(2): p. 91-99.
70. Pease, R.F. and S.Y. Chou, *Lithography and other patterning techniques for future electronics.* Proceedings of the IEEE, 2008. **96**(2): p. 248-270.
71. Sze, S.M., *Semiconductor devices: physics and technology*. 2008: John Wiley & Sons.
72. Yadav, T.P., R.M. Yadav, and D.P. Singh, *Mechanical milling: a top down approach for the synthesis of nanomaterials and nanocomposites.* Nanoscience and Nanotechnology, 2012. **2**(3): p. 22-48.
73. Chichkov, B.N., et al., *Femtosecond, picosecond and nanosecond laser ablation of solids.* Applied Physics A, 1996. **63**(2): p. 109-115.
74. Wu, Z.-S., et al., *Synthesis of graphene sheets with high electrical conductivity and good thermal stability by hydrogen arc discharge exfoliation.* ACS nano, 2009. **3**(2): p. 411-417.
75. Ashalley, E., et al., *Bismuth telluride nanostructures: preparation, thermoelectric properties and topological insulating effect.* Frontiers of Materials Science, 2015. **9**(2): p. 103-125.
76. Lu, J., J.W. Elam, and P.C. Stair, *Synthesis and stabilization of*

supported metal catalysts by atomic layer deposition. Accounts of chemical research, 2013. **46**(8): p. 1806-1815.
77. Brinker, C.J. and G.W. Scherer, *Sol-gel science: the physics and chemistry of sol-gel processing*. 2013: Academic press.
78. Rubinstein, I., et al., *Ionic recognition and selective response in self-assembling monolayer membranes on electrodes.* Nature, 1988. **332**(6163): p. 426-429.
79. Thiruvengadathan, R., et al., *Nanomaterial processing using self-assembly-bottom-up chemical and biological approaches.* Reports on Progress in Physics, 2013. **76**(6): p. 066501.
80. Kim, B.-H., et al., *Preparation of TiO 2 thin film by liquid sprayed mist CVD method.* Materials Science and Engineering: B, 2004. **107**(3): p. 289-294.
81. Sajanlal, P.R., et al., *Anisotropic nanomaterials: structure, growth, assembly, and functions.* Nano Reviews & Experiments, 2011. **2**.
82. Zsigmondy, R., *Colloids and the ultramicroscope: a manual of colloid chemistry and ultramicroscopy*. 1909: J. Wiley & Sons.
83. Jana, N.R., L. Gearheart, and C.J. Murphy, *Evidence for seed-mediated nucleation in the chemical reduction of gold salts to gold nanoparticles.* Chemistry of Materials, 2001. **13**(7): p. 2313-2322.
84. O' regan, B. and M. Grfitzeli, *A low-cost, high-efficiency solar cell based on dye-sensitized.* nature, 1991. **353**(6346): p. 737-740.
85. Abdou, E., et al., *Photostability of low cost dye-sensitized solar cells based on natural and synthetic dyes.* Spectrochimica Acta Part A: Molecular and Biomolecular Spectroscopy, 2013. **115**: p. 202-207.
86. Gong, J., J. Liang, and K. Sumathy, *Review on dye-sensitized solar cells (DSSCs): fundamental concepts and novel materials.* Renewable and Sustainable Energy Reviews, 2012. **16**(8): p. 5848-5860.
87. Wongcharee, K., V. Meeyoo, and S. Chavadej, *Dye-sensitized solar cell using natural dyes extracted from rosella and blue pea flowers.* Solar Energy Materials and Solar Cells, 2007. **91**(7): p. 566-571.
88. Nazeeruddin, M.K., E. Baranoff, and M. Grätzel, *Dye-sensitized solar cells: a brief overview.* Solar Energy, 2011. **85**(6): p.

1172-1178.
89. Ko, K.H., Y.C. Lee, and Y.J. Jung, *Enhanced efficiency of dye-sensitized TiO 2 solar cells (DSSC) by doping of metal ions.* Journal of colloid and interface science, 2005. **283**(2): p. 482-487.
90. Zhu, K., et al., *Enhanced charge-collection efficiencies and light scattering in dye-sensitized solar cells using oriented TiO2 nanotubes arrays.* Nano letters, 2007. **7**(1): p. 69-74.
91. Qi, J., et al., *Highly efficient plasmon-enhanced dye-sensitized solar cells through metal@ oxide core-shell nanostructure.* ACS nano, 2011. **5**(9): p. 7108-7116.
92. Dang, X., et al., *Tunable localized surface plasmon-enabled broadband light-harvesting enhancement for high-efficiency panchromatic dye-sensitized solar cells.* Nano letters, 2013. **13**(2): p. 637-642.
93. Kawashima, T., et al., *FTO/ITO double-layered transparent conductive oxide for dye-sensitized solar cells.* Journal of Photochemistry and Photobiology A: Chemistry, 2004. **164**(1): p. 199-202.
94. Park, N.-G., J. Van de Lagemaat, and A. Frank, *Comparison of dye-sensitized rutile-and anatase-based TiO2 solar cells.* The Journal of Physical Chemistry B, 2000. **104**(38): p. 8989-8994.
95. Buscaino, R., et al., *A mass spectrometric analysis of sensitizer solution used for dye-sensitized solar cell.* Inorganica Chimica Acta, 2008. **361**(3): p. 798-805.
96. Grätzel, M., *Recent advances in sensitized mesoscopic solar cells.* Accounts of chemical research, 2009. **42**(11): p. 1788-1798.
97. Nazeeruddin, M.K., et al., *Combined experimental and DFT-TDDFT computational study of photoelectrochemical cell ruthenium sensitizers.* Journal of the American Chemical Society, 2005. **127**(48): p. 16835-16847.
98. Qin, Y. and Q. Peng, *Ruthenium sensitizers and their applications in dye-sensitized solar cells.* International Journal of Photoenergy, 2012. **2012**.
99. Sekar, N. and V.Y. Gehlot, *Metal complex dyes for dye-sensitized solar cells: Recent developments.* Resonance, 2010. **15**(9): p. 819.
100. Karmakar, A.S. and J.P. Ruparelia. *A critical review on dye sensitized solar cells*. in *International conference on current*

trends in technology, NUiCONE. 2011.
101. He, J., et al., *Ruthenium-Based Photosensitizers for Dye-Sensitized Solar Cells*, in *Organometallics and Related Molecules for Energy Conversion*. 2015, Springer. p. 91-114.
102. Chen, J., et al., *Connection style and spectroscopic properties: theoretical understanding of the interface between N749 and TiO 2 in DSSCs.* Dyes and Pigments, 2013. **99**(1): p. 201-208.
103. Wu, J., et al., *Electrolytes in dye-sensitized solar cells.* Chemical reviews, 2015. **115**(5): p. 2136-2173.
104. Kim, M.-J., et al., *Unusual enhancement of photocurrent by incorporation of Bronsted base thiourea into electrolyte of dye-sensitized solar cell.* The Journal of Physical Chemistry C, 2010. **114**(46): p. 19849-19852.
105. Mathew, A., et al., *Effect of iodine concentration on the photovoltaic properties of dye sensitized solar cells for various I_2/LiI ratios.* Electrochimica Acta, 2013. **87**: p. 92-96.
106. Suzuka, M., et al., *A quasi-solid state dssc with 10.1% efficiency through molecular design of the charge-separation and-transport.* Scientific Reports, 2016. **6**.
107. Thomas, S., et al., *A review on counter electrode materials in dye-sensitized solar cells.* Journal of Materials Chemistry A, 2014. **2**(13): p. 4474-4490.
108. Wang, H. and Y.H. Hu, *Graphene as a counter electrode material for dye-sensitized solar cells.* Energy & Environmental Science, 2012. **5**(8): p. 8182-8188.
109. Roy-Mayhew, J.D., et al., *Functionalized graphene as a catalytic counter electrode in dye-sensitized solar cells.* Acs Nano, 2010. **4**(10): p. 6203-6211.
110. Singh, V.K., R.K. Kanaparthi, and L. Giribabu, *Emerging molecular design strategies of unsymmetrical phthalocyanines for dye-sensitized solar cell applications.* RSC Advances, 2014. **4**(14): p. 6970-6984.
111. Nahm, C., et al., *The effects of 100 nm-diameter Au nanoparticles on dye-sensitized solar cells.* Applied Physics Letters, 2011. **99**(25): p. 253107.
112. Brown, M.D., et al., *Plasmonic dye-sensitized solar cells using core- shell metal- insulator nanoparticles.* Nano letters, 2010. **11**(2): p. 438-445.

113. Choi, H., W.T. Chen, and P.V. Kamat, *Know thy nano neighbor. Plasmonic versus electron charging effects of metal nanoparticles in dye-sensitized solar cells.* ACS nano, 2012. **6**(5): p. 4418-4427.
114. Liu, W.-L., et al., *The influence of shell thickness of Au@ TiO 2 core-shell nanoparticles on the plasmonic enhancement effect in dye-sensitized solar cells.* Nanoscale, 2013. **5**(17): p. 7953-7962.
115. Standridge, S.D., G.C. Schatz, and J.T. Hupp, *Distance dependence of plasmon-enhanced photocurrent in dye-sensitized solar cells.* Journal of the American Chemical Society, 2009. **131**(24): p. 8407-8409.
116. Hossain, M.A., et al., *Surface plasmonic effects on dye-sensitized solar cells by SiO_2-encapsulated Ag nanoparticles.* Current Applied Physics, 2016. **16**(3): p. 397-403.
117. Zarick, H.F., et al., *Enhanced efficiency in dye-sensitized solar cells with shape-controlled plasmonic nanostructures.* Acs Photonics, 2014. **1**(9): p. 806-811.
118. Elbohy, H., et al., *Incorporation of plasmonic Au nanostars into photoanodes for high efficiency dye-sensitized solar cells.* Journal of Materials Chemistry A, 2016. **4**(2): p. 545-551.
119. Bai, L., et al., *Plasmonic enhancement of the performance of dye-sensitized solar cell by core-shell AuNRs@ SiO_2 in composite photoanode.* Journal of Power Sources, 2014. **272**: p. 1100-1105.
120. Guo, K., et al., *Enhancement of properties of dye-sensitized solar cells by surface plasmon resonance of Ag nanowire core-shell structure in TiO_2 films.* Journal of Materials Chemistry A, 2013. **1**(24): p. 7229-7234.
121. Gangishetty, M.K., et al., *Plasmonic enhancement of dye sensitized solar cells in the red-to-near-infrared region using triangular core-shell Ag@ SiO_2 nanoparticles.* ACS applied materials & interfaces, 2013. **5**(21): p. 11044-11051.
122. Kim, H.-Y. and J.S. Suh, *Panchromatic quasi-monolayer of Ag nanoparticles for high-efficiency dye-sensitized solar cells.* RSC Advances, 2015. **5**(74): p. 59895-59902.
123. Al-Azawi, M.A., et al., *Preparation of gold and gold-silver alloy nanoparticles for enhancement of plasmonic dye-sensitized solar cells performance.* Solar Energy, 2016. **126**: p.

93-104.
124. Xu, Q., et al., *Broadband light absorption enhancement in dye-sensitized solar cells with Au-Ag alloy popcorn nanoparticles.* Scientific reports, 2013. **3**: p. 2112.
125. Yun, J., S.H. Hwang, and J. Jang, *Fabrication of Au@ Ag core/shell nanoparticles decorated TiO_2 hollow structure for efficient light-harvesting in dye-sensitized solar cells.* ACS applied materials & interfaces, 2015. **7**(3): p. 2055-2063.
126. Dong, H., et al., *Ag-encapsulated Au plasmonic nanorods for enhanced dye-sensitized solar cell performance.* Journal of Materials Chemistry A, 2015. **3**(8): p. 4659-4668.
127. Suh, J., D. DiLella, and M. Moskovits, *Surface-enhanced Raman spectroscopy of colloidal metal systems: a two-dimensional phase equilibrium in p-aminobenzoic acid adsorbed on silver.* The Journal of Physical Chemistry, 1983. **87**(9): p. 1540-1544.
128. Rohiman, A., et al. *Study of colloidal gold synthesis using Turkevich method*. in *AIP Conference Proceedings*. 2011. AIP.
129. Ng, S.-P., et al., *Plasmonic enhanced dye-sensitized solar cells with self-assembly gold-TiO_2@core-shell nanoislands.* Solar Energy, 2014. **99**: p. 115-125.
130. Jeong, N.C., C. Prasittichai, and J.T. Hupp, *Photocurrent enhancement by surface plasmon resonance of silver nanoparticles in highly porous dye-sensitized solar cells.* Langmuir, 2011. **27**(23): p. 14609-14614.
131. Kim, H.-Y., H. Yoon, and J.S. Suh, *Surface plasmon-enhanced dye-sensitized solar cells based on double-layered composite films consisting of TiO_2/Ag and TiO_2/Au nanoparticles.* RSC Advances, 2015. **5**(35): p. 27464-27469.
132. Mayer, K.M. and J.H. Hafner, *Localized surface plasmon resonance sensors.* Chemical reviews, 2011. **111**(6): p. 3828-3857.
133. Kreibig, U. and M. Vollmer, *Optical properties of metal clusters*. Vol. 25. 2013: Springer Science & Business Media.
134. Kim, H.-Y., et al., *Aggregation effect of silver nanoparticles on the energy conversion efficiency of the surface plasmon-enhanced dye-sensitized solar cells.* Solar Energy, 2014. **109**: p. 61-69.
135. Kim, Y.J., et al., *Formation of highly efficient dye-sensitized*

solar cells by hierarchical pore generation with nanoporous TiO_2 spheres. Advanced Materials, 2009. **21**(36): p. 3668-3673.
136. Lee, S., G.H. Gu, and J.S. Suh, *A simple method to fabricate silver colloid clusters for surface-enhanced Raman scattering.* Chemical Physics Letters, 2011. **511**(1): p. 121-125.
137. Liz-Marzán, L.M., *Tailoring surface plasmons through the morphology and assembly of metal nanoparticles.* Langmuir, 2006. **22**(1): p. 32-41.
138. Kim, K., H. Ryoo, and K.S. Shin, *Adsorption and aggregation characteristics of silver nanoparticles onto a poly (4-vinylpyridine) film: a comparison with gold nanoparticles.* Langmuir, 2010. **26**(13): p. 10827-10832.
139. Lim, S.P., et al., *Enhanced photovoltaic performance of silver@ titania plasmonic photoanode in dye-sensitized solar cells.* RSC Advances, 2014. **4**(72): p. 38111-38118.
140. Neighbor, K.T.N., *Plasmonic versus Electron Charging Effects of Metal Nanoparticles in Dye-Sensitized Solar Cells Choi, Hyunbong; Chen, Wei Ta; Kamat, Prashant V.* ACS Nano, 2012. **6**(5): p. 4418-4427.

국문 초록

염료감응태양전지는 가격경쟁력이 우수하고, 투명하며 다양한 색상을 구현할 수 있는 기술로 다양한 응용성이 기대되는 기술이다. 하지만 기존의 실리콘 태양전지에 비해 효율이 낮으므로, 효율 향상에 대한 연구가 활발히 진행되고 있다.

일반적으로 염료감응 태양전지의 효율은 염료의 광 흡수 정도에 많은 영향을 받는다. 그러므로 전자전달이 용이한 염료를 이용하거나 장파장의 빛을 흡수하는 염료를 이용하기도 한다. 또는 다양한 빛 흡수를 일으키는 염료를 이용하는 대신 다양한 국부적 표면 플라즈모닉 현상을 나타내는 금속 나노입자를 이용하여 같은 효과를 기대 할 수 있다. 따라서 본 연구에서는 금속 나노입자의 국부적 표면 플라즈모닉 효과를 이용하여 염료감응 태양전지의 효율을 향상시키고자 하였다.

첫 번째 연구에서는 은 나노입자와 금 나노입자를 제조하여 광전극 층에 도입함으로써 플라즈모닉 염료감응 태양전지를 제작하였다. 제조한 구형의 은과 금 나노입자의 플라즈모닉 흡수밴드는 각각 λ_{max} 가 400nm와 520nm 근방이며, 이는 염료감응태양전지에서 주로 사용되고 있는 N719 염료의 두 흡수밴드 (λ_{max}=393, 533 nm)와 잘 중첩된다. 일반적으로 플라즈모닉 염료감응 태양전지의 효율은 플라즈모닉 흡수밴드와 염료의 흡수밴드의 중첩도에 영향을 받는다. 그러므로 은과 금 나노입자를 함께 광전극층에 더블레이어 형태로 도입함으로써 N719 염료의 두 흡수밴드와 중첩도를 높여 플라즈모닉 염료감응태양전지의 효율을 향상시키고자 하였다. 한 가지 금속 나노입자를 도입하는 경우보다 두 금속 나노입자를 함께 도입하였을 때 높은 효율을 보였다. 은과 금나노입자의 플라즈모닉 효과에 의해 금속 나노입자 주위의 전자기장이 증폭하고 금속 나

노입자 표면 또는 근처의 염료의 빛 흡수를 향상시키며, 생성되는 전자의 양을 증가시킴으로써 효율이 증가된다. 더 나아가 보다 높은 효율의 플라즈모닉 염료감응태양전지를 제작하기 위해서는 광전극층에서의 은과 금 나노입자의 위치를 고려 해야한다. 장파장의 빛이 단파장의 빛보다 멀리 도달할 수 있으므로, 단파장을 흡수하는 은 나노입자를 아래에, 장파장을 흡수하는 금 나노입자를 위에 위치함으로써 효율을 향상 시킬 수 있었다. 또한, 이산화 티탄 입자에 대한 도입되는 은과 금 나노입자의 중량비를 고려해야 한다. 최적의 중량비에서 최대 효율을 나타내며 그 이상의 중량비에서는 오히려 효율이 감소하는 경향을 보였다. 이는 중량비가 증가할수록 이산화티탄 내에서의 금속나노입자간의 응집 현상이 일어나, 금속나노입자의 플라즈모닉 흡수밴드가 장파장으로 이동하면서 N719 염료의 흡수밴드와의 중첩도가 감소하여 플라즈모닉 염료감응 태양전지의 효율이 감소하는 것이다.

그러므로 보다 높은 효율의 염료감응태양전지를 제작하기 위해서는 금속 나노입자의 응집현상을 최소화 해야 하므로, 다음 연구에서는 은과 금 나노입자로 이루어진 플라즈모닉 층을 광전극층 위에 흡착시킴으로써 플라즈모닉 염료감응 태양전지를 제작하였다. 이때 은과 금 나노입자를 poly(4-vinylpyridine)(P4VP) 을 통해 광전극층 위에 흡착 시킴으로써 금속 나노입자가 응집되지 않고 흡착되어 있음을 확인 할 수 있었다. 은과 금 나노입자로 이루어진 플라즈모닉 레이어를 도입함으로써 8.39% 에서 10.17% 로 효율이 향상되었다. 이는 광전류의 증가로 인해 효율이 향상 되었으며, 은과 금 나노입자의 국부적 표면 플라즈모닉 현상 때문이다. 광전극층 위에 위치한 플라즈모닉 레이어가 빛 산란 역할을 함으로써, 입사하는 빛이 소자 내에 좀 더 머무를 수 있게 하여 광 흡수가 증가하며 산란된 빛에 의해 플라즈모닉 레이어 표면이나 표면 근처에 존재하는 N719 염료의 빛 흡수를 보다 증가시켜준다.

마지막으로, 앞선 연구에서 사용되었던 구형의 금속 나노입자는 염료의 흡수 밴드와 잘 중첩되지만 좁은 단일 플라즈모닉 흡수 밴드로 빛 흡수영역이 제한된다. 그러므로 금속 나노입자의 형태를 다양하게 함으로써 다양한 플라즈모닉 흡수를 유발하고자 multi-shaped 은 나노입자를 제조하였다. 제조한 multi-shaped 은 나노입자는 구형, 판, 줄 모양의 은 나노입자가 포함되어있다. 구형의 은 나노입자가 400nm 근방에서 좁은 단일 플라즈모닉 흡수 밴드를 가지는 반면, Multi-shaped 은 나노입자는 420nm 근방에서 좀더 넓은 흡수 밴드를 가지며, 393nm 에서의 N719 염료의 흡수 밴드 영역뿐 만 아니라 N719 염료의 빛 흡수가 약한 450-550nm 영역에서도 빛 흡수가 일어난다. 보다 넓은 빛 흡수를 가지는 multi-shaped 은 나노입자와 금 나노입자를 사용함으로써 구형의 은 나노입자와 금 나노입자를 사용한 염료감응태양전지가 9.90%인 것에 비해 10.22 %로 효율이 향상되었다. 이로 인해 금속 나노입자의 형태를 조절하여 다양한 빛 흡수를 유발함으로써 보다 더 높은 효율의 염료감응태양전지를 제작할 수 있었다.

중심어 : 염료감응 태양전지, 국부적 표면 플라즈몬 공명, 은 나노입자, 금 나노입자